#### People's Democratic Republic of Algeria Ministry of Higher Education and Scientific Research Ferhat ABBAS University - Setif 1





#### **THESIS**

Presented in the Department of Physics

Faculty of Sciences

To obtain the degree of

#### **DOCTORATE**

Domain: Matter Sciences Option: Condensed Matter

#### TITLE

# Effect of Li<sup>+</sup>, Na<sup>+</sup>, and K<sup>+</sup> Co-Doping on Structural, Morphological and Luminescent Properties of Ce<sup>3+</sup>/Pr<sup>3+</sup>-Activated Lu<sub>3</sub>Al<sub>5</sub>O<sub>12</sub> Garnet powder scintillators

By

#### **AKHRIB Zohra**

*In the presence of the jury* 

<b>GUEMMAZ Mohamed</b>	Prof	Ferhat ABBAS University Setif 1	President
<b>GUERBOUS</b> Lakhdar	Dir/R	<b>Nuclear Research Center of Algiers</b>	Thesis Director
BOUHEMADOU Abdelmadjid	Prof	Ferhat ABBAS University Setif 1	<b>Co-Director</b>
KHARFI Faycal	Prof	Ferhat ABBAS University Setif 1	Thesis Examiner
BAADJI Nadjib	Prof	Mohamed BOUDIAF University M'sila	Thesis Examiner
DIAF Madjid	Prof	Badji Mokhtar - Annaba University	Thesis Examiner
FASOLI Mauro	Prof	University of Milano-Bicocca	Guest
COVA Francesca	MCA	University of Milano-Bicocca	Guest

## Acknowledgments

As I arrive at the end of this long and enriching journey, it was not just academic. It was also human, personal, and blooming. I am filled with deep gratitude and emotion. This PhD thesis is more than a scientific endeavor, it is a reflection of years of perseverance, growth, and the unwavering support of many kind souls who have walked beside me, believed in me, and lifted me when I faltered.

This PhD thesis was conducted as a collaborative effort between the Department of Physics, University of Ferhat Abbas Setif 1 (UFAS), the Algiers Nuclear Research Center, and the Materials Science Department, University of Milan-Bicocca, Italy. I am deeply grateful to these institutions for providing me with the opportunity and resources to pursue this research. I am especially thankful to the department of Physics, UFAS for its academic and administrative support during my doctoral studies.

First and foremost, I would like to express my deepest gratitude to my supervisor, Prof. GUERBOUS Lakhdar, Director of Research at the Algiers Nuclear Research Centre (CRNA), for his invaluable guidance, patience, and trust throughout these years. His expertise and support have been essential to the successful completion of my thesis. I am truly grateful for the freedom he gave me to explore, and for always being a steady presence when I needed direction.

I also wish to express my deep appreciation to my co-supervisor, Prof. BOUHEMADOU Abdelmadjid, Professor at the department of Physics at UFAS, for his insightful feedback, constructive suggestions, and generous support throughout this work.

I would like to express my sincere gratitude to Professor GUEMMAZ Mohamed, from the department of Physics at UFAS, for doing me the honor of chairing the jury of this thesis. I warmly thank him for his availability and for kindly accepting this role.

My sincere thanks also go to the esteemed jury and invited members:

Prof. KHARFI Faycal, from the department of Physics at UFAS; Prof. BAADJI Nadjib, from Mohamed BOUDIAF University M'sila; Prof. DIAF Madjid, Badji Mokhtar-Annaba University; Prof. FASOLI Mauro and Dr. COVA Francesca, from the Materials Science

Department, University of Milan-Bicocca, Italy. Thank you for your time, your thoughtful suggestions, and your inspiring perspectives that enriched my work.

This research work was primarily conducted at the Algiers Nuclear Research Center (CRNA), and I would like to express my sincere gratitude to the General Management of the CRNA for graciously welcoming me into their esteemed institution and providing me with the opportunity to carry out my doctoral research within the framework of their scientific activities.

I am deeply thankful to Dr. Allaoua Boukerika, who was the very first person to accompany me during my initial steps in the laboratory. His guidance and encouragement played a vital role in shaping my early experience in experimental work.

My heartfelt thanks also go to Ahmed Rafik Touil, Mohamed Taibeche and Mustapha Lasmi, whose collaboration, generosity, and support, particularly in the VASP calculations enriched this work in both depth and direction.

To the entire CRNA laboratory team, thank you for your cooperation, your technical support and for creating an environment where this research could truly take root and flourish.

I would like to sincerely thank Prof. Paul Lecoq for his generosity and support at a pivotal moment in my PhD journey. When I faced the lack of materials needed to complete essential parts of my thesis, he kindly recommended me to leading scientists in the scintillation field. Thanks to his trust and encouragement, his belief in me and his willingness to help opened doors, and I will remain deeply grateful for his kindness.

I am sincerely grateful to Prof. Anna Vedda from the Materials Science Department, University of Milan-Bicocca for warmly welcoming me into her department and offering me the opportunity to carry out part of my research in such a supportive environment.

My deepest thanks go to Professor Mauro Fasoli, who was a true light throughout my doctoral journey. His unwavering support, generous guidance, and sincere belief in my potential accompanied me through every phase of this work in the lab, during the writing process, and even from afar. His presence was more than academic; it was uplifting. Through his patience and trust, he not only helped me advance scientifically, but also

gave me the confidence to grow into a more independent and thoughtful researcher. For all the time, effort, and kindness he offered, I will remain deeply and sincerely grateful.

I also warmly thank Dr. Francesca Cova for her patience, clarity, and generous support during my experimental measurements. Her insights greatly deepened my understanding of scintillation mechanisms and helped me grow as a researcher.

I would like to thank the entire team at the Department of Materials Science for their welcoming spirit, technical support, and for providing an environment that was both professionally enriching and personally uplifting.

I also sincerely thank Prof. Haikel Jelassi Director of Research at the National Center for Nuclear Science and Technology (CNSTN), Tunisia, for his invaluable support in facilitating important experimental work during my thesis. Thanks to his guidance and generosity, I was able to carry out advanced measurements, including SEM, EDS and Raman spectroscopy, in well-equipped institutions across Tunisia.

To my dear friends and colleagues, thank you for walking beside me through both light and shadow. Your presence, kindness, and laughter brought comfort to my heart and joy to my days. Thank you for reminding me to breathe, to smile, to rest, and above all to believe in myself.

Finally, to my beloved family, Mom, Dad, my brothers and my loved ones, no words can ever fully express the gratitude I carry in my heart. Your unconditional love, prayers, sacrifices and unwavering belief in me gave me the strength to keep going, even in the most challenging moments. In every step forward, I carried your hopes with me. This achievement is not mine alone it is ours.

"Like a peony, I did not bloom all at once, but layer by layer, in silence and grace, I opened to the light that waited for me all along." Mira

#### LIST OF FIGURES

**Figure I.1** The three primary photon interaction processes' respective significance in relation to photon energy and atomic number (Z).

**Figure I.2** A schematic illustration of the scintillation mechanism in an inorganic scintillator. Scintillation process over time, highlighting the progression of particle energy through the various stages that contribute to scintillation emission.

Figure I.3 Pulse heigh spectrum. Definition of detector resolution.

**Figure I.4** Unit cell illustration of  $Lu_3Al_5O_{12}$  crystal structures (a) Aluminum site of  $Lu_3Al_5O_{12}$  (c).

**Figure I.5** Trivalent Ce and Pr ions' 4f energy levels, as well as their 4f-5d absorption and emission bands, are displayed in the Dieke diagram.

**Figure I.6** A simplified diagram of the energy levels of the  $Ce^{3+}$  (4f¹) ion is shown. On the left, only the 4f and 5d electronic levels are shown, without taking into account additional interactions. On the right, the effects of spin-orbit coupling (SO) and crystal field splitting are illustrated. The spin-orbit interaction divides the 4f level into two sublevels, separated by around 2000 cm-¹. The crystal field effect ( $\Delta$ ) divides the 5d level into five distinct components, covering an energy range of around 15,000 cm-¹.

**Figure I.7** Representative application areas for Ce<sup>3+</sup>-doped garnet phosphors.

**Figure I.8** The Pr<sup>3+</sup> ion's energy level scheme is made up of a dense network of energy levels that stretch up to about 25,000 cm<sup>-1</sup>.

**Figure I.9** Diagram of a scintillation counter.

**Figure I.10** Eu<sup>3+</sup> doped Gd<sub>2</sub>O<sub>3</sub> fluorescence spectra at T=10K excitation at 580.7 nm (to  $4f^7 7F^{0-5}D_0$ ). The fluorescence transition is equivalent to Eu<sup>3+</sup>'s  $4f^{7\,5}D_0$ -7F<sub>2</sub>.

**Figure I.11** Effects of crystal field oscillations on concentration quenching: excitation energy can travel long distances in bulk materials (left) until it reaches a non-radiative defect (light grey) due to the alignment of energy levels (black lines) between dopant ions.

**Figure I.12** new uses illustrate the wider range of applications made possible by the characteristics of nanoparticles compared with their bulk counterparts.

**Figure II.1** Synthesis process steps and final products of some codoped LuAG:Ce and LuAG:Pr by different content of Li, Na and K powders prepared - **CRNA Algiers.** 

**Figure II.2** The flow chart for LuAG powders synthesis by the sol-gel method.

**Figure II.3** Visualisation of the Braggs equation.

**Figure II.4** X-ray diffraction (XRD) technique a PANanlytical X'Pert (Philips) PRO **-CRNA Algiers**.

**Figure II.5** JEOL JSM-5400 Thermoscientific Scanning Electron Microscope- **ETAP Tunisia** 

Figure II.6 Perkin-Elmer (LS-50B) luminescence spectrometer -CRNA Algiers.

**Figure II.7** Homemade instrumental setup for radio- thermo- and photo-luminescence- **Unimib Italy**.

Figure II.8 Instrumental setup for PL and scintillation decay-Unimib Italy.

**Figure II.9** wavelength-resolved thermally stimulated luminescence below and above room temperature, X-ray spectroscopy apparatuses – **Unimib Italy**.

**Figure II.10**. VASP input and output files.

**Figure III.1** XRD patterns of  $Lu_3Al_5O_{12}$ : 0.5 at. % Ce<sup>+3</sup>, co-doped with different Li<sup>+</sup> co-doping concentration.

**Figure III.2** Structure configurations containing, (a) LuAG doped Ce, (b) LuAG:Ce codoped Li<sub>Al</sub> substitute defect, and (c) LuAG:Ce co-doped Li<sub>Lu</sub> substitute defect. Green, red, blue, purple and yellow spheres represent Li, O, Al, Lu and Ce atoms, respectively.

**Figure III.3** (a) Height (cts), (b)  $2\theta$  (°) and (c) the crystal cell volume V(ų) as a function of Li<sup>+</sup> co-doping concentration.

**Figure III.4** Variation of crystallite size calculated by Williamson-Hall formula and the strain with against the Li<sup>+</sup> content.

**Figure III.5** XRD patterns of Lu<sub>3</sub>Al<sub>5</sub>O<sub>12</sub>: 0.5 at. % Ce  $^{+3}$ , co-doped with different Na $^+$  co-doping concentration.

**Figure III.6** XRD patterns of  $Lu_3Al_5O_{12}$ : 0.5 at. % Ce<sup>+3</sup>, co-doped with different K<sup>+</sup> co-doping concentration.

**Figure III.7** Density of State for **(a)**: LuAG:Ce co-doped  $\text{Li}_{Al-24d}$  substitute defect, **(b)** LuAG: Ce co-doped  $\text{Li}_{Lu}$ .

**Figure III.8** Left: FE-SEM images of three samples, namely LuAG:  $Ce^{3+}$ , x at. % Li<sup>+</sup> (x = 0, 5 and 15), insets, enlarged regions corresponding to the origins of the arrows. Right the corresponding attached EDS spectra.

**Figure III.9 (a)** Room temperature emission spectra of Lu<sub>2.985-x</sub>Li<sub>x</sub>Ce<sub>0.015</sub> Al<sub>5</sub>O<sub>12</sub>Co-doped by different content of Li<sup>+</sup> powders and single crystal (SC) **(b)** Variation of integrated intensities with Li<sup>+</sup> co-doping concentrations **(c)** Variation of integrated intensities as well as crystallite size in function of Li<sup>+</sup> content.

**Figure III.10** Right, Excitation and emission spectra of LuAG: 0.5%Ce<sup>3+</sup>Co-doped by Li<sup>+</sup> powders. Left: Ce<sup>3+</sup> 4f and 5d level positions relative to LuAG electronic bands. The band gap (Eg), The redshift D (Ce<sup>3+</sup>, LuAG), the Crystal Field Splitting (CFS), the lowest  $4f \leftrightarrow 5d$  energy transition E (Ce<sup>3+</sup>, LuAG), and the energies  $\Delta E_{4f-VB}$ ,  $\Delta E_{5d-CB}$  are shown.

**Figure III.11** Variation of the crystal field splitting of the lowest  $5d_1$ - $5d_2$  levels ( $\Delta_{12}$ ) as well as redshift (D (Ce<sup>3+</sup>, LuAG)) as a function of Li<sup>+</sup> content. Values for the single crystal (SC) are shown.

**Figure III.12** Emission and excitation spectrum fitted by two Gaussian curves showing the Stokes Shift and ZPL. Franck-Condon diagram of the ground and excited states of the optical center in solids.

**Figure III.13** Room temperature emission and excitation spectra of LuAG: 0.5 at. % Ce<sup>3+</sup> Co-doped by different content of K<sup>+</sup> (left) and by different content Na<sup>+</sup> (right) powders.

**Figure III.14** (a) PL decay curves of LuAG: 0.5% Ce<sup>3+</sup> co-doped by Li<sup>+</sup> powders as well as that of SC with Li<sup>+</sup> content, (b) Monoexponential and three exponential fits for the emission decay curves of LuAG: Ce<sup>3+</sup> SC and LuAG: Ce<sup>3+</sup>, 5 at. % Li<sup>+</sup> powder respectively. **Figure III.15a** variation of the experimental Ce<sup>3+</sup> decay time ( $\tau_{exp} = \tau_3$ ) against Li<sup>+</sup> content as well as of SC.

**Figure III.15b** variation of the effective refractive index  $(n_{eff})$  and the PL emission intensity against Li<sup>+</sup> content.

**Figure III.16** Radioluminescence spectra of LuAG: 0.5 at. % Ce<sup>3+</sup> codoped by different content of Li<sup>+</sup> powders, single crystal (SC) and BGO (left). Variation of intensities with Li<sup>+</sup> co-doping concentrations (right).

**Figure III.17** Radioluminescence decay time under pulsed X-ray excitation of LuAG:Ce<sup>3+</sup>, x at. % Li<sup>+</sup> powders and LuAG:Ce<sup>3+</sup> single crystal.

**Figure III.18** TSL above room temperature (X-ray excitation) of LuAG:Ce<sup>3+</sup>, x at. % Li<sup>+</sup> powders codoped with different content of Li<sup>+</sup>.

**Figure IV.1** XRD patterns of Lu<sub>3</sub>Al<sub>5</sub>O<sub>12</sub>: 1 at. % Pr +3, co-doped with different content of Li<sup>+</sup>.

**Figure IV.2** XRD patterns of Lu<sub>3</sub>Al<sub>5</sub>O<sub>12</sub>: 1 at. % Pr<sup>+3</sup>, co-doped with different content of K<sup>+</sup>.

**Figure IV.3** XRD patterns of Lu<sub>3</sub>Al<sub>5</sub>O<sub>12</sub>: 1 at. % Pr<sup>+3</sup>, co-doped with different content of Na<sup>+</sup>.

**Figure IV.4** SEM images of samples, namely LuAG: Pr<sup>3+</sup>, 0Li; LuAG: Pr<sup>3+</sup>, 15Li; LuAG: Pr<sup>3+</sup>, 5K; LuAG: Pr<sup>3+</sup>, 15Na.

**Figure IV.5** Schematic energy diagram of Pr<sup>3+</sup> ion with indication of the absorption and emission transitions of this ions in the LuAG host.

**Figure IV.6** Room temperature emission and excitation spectra of Lu<sub>3</sub>Al<sub>5</sub>O<sub>12</sub>: 1 at. %Pr<sup>+3</sup> Co-doped by different content of Li<sup>+</sup> powders.

**Figure IV.7** Room temperature emission and excitation spectra of Lu<sub>3</sub>Al<sub>5</sub>O<sub>12</sub>: 1 at. %Pr<sup>+3</sup> Co-doped by different content of Li<sup>+</sup> powders.

**Figure IV.8** Room temperature emission and excitation spectra of  $Lu_3Al_5O_{12}$ : 1 at. %Pr<sup>+3</sup> Co-doped by different content of K<sup>+</sup> powders.

**Figure IV.9** Room temperature emission and excitation spectra of Lu<sub>3</sub>Al<sub>5</sub>O<sub>12</sub>: 1 at. %Pr <sup>+3</sup> Co-doped by (undoped, 1%Li<sup>+</sup>, 1%Na<sup>+</sup>, 5%K<sup>+</sup>) powders.

**Figure IV.10** Radioluminescence spectra of Lu<sub>3</sub>Al<sub>5</sub>O<sub>12</sub>: 1 at. %Pr <sup>+3</sup> codoped by different content of Li<sup>+</sup> powders and Variation of RL integrated amplitude.

**Figure IV.11** Radioluminescence decay time under pulsed X-ray excitation of  $Lu_3Al_5O_{12}$ : 1 at. %Pr<sup>+3</sup>, x at. % Li<sup>+</sup> powders.

#### LIST OF TABLES

**Table I.1** the applications of various Ce<sup>3+</sup>-doped garnet phosphors.

**Table I.2** Summary of previous studies on the effects of Li<sup>+</sup>, Na<sup>+</sup>, and K<sup>+</sup> co-doping on the structural, photoluminescent, and scintillation performance of Ce<sup>3+</sup>- and Pr<sup>3+</sup>-doped garnet materials.

**Table II.1** The different files used in the calculations.

**Table III.1** Structural parameters for samples of LuAG: 0.5%Li co-doped with different content of Li<sup>+</sup>.

**Table III.2** Structural parameters for samples of LuAG: 0.5% Ce co-doped with different content of Na<sup>+</sup>.

**Table III.3** Structural parameters for samples of LuAG: 0.5% Ce co-doped with different content of K<sup>+</sup>.

**Table III.4** Stoichiometric ratios between the different elements in Lu<sub>3</sub>Al<sub>5</sub>O<sub>12</sub>: Ce<sup>3+</sup>, Li<sup>+</sup>.

**Table III.5** Excitation and emission maxima, *FWHM*, Stokes shift, Huang-Rhys parameters of LuAG: Ce<sup>3+</sup>, Li<sup>+</sup> nanophosphors and that of single crystal (SC).

**Table III.6** Summary of the radiative decay parameters for Ce<sup>3+</sup> in LuAG: Ce<sup>3+</sup>, Li<sup>+</sup> nanophosphors and single crystal (SC).

**Table IV.1** Structural parameters for samples of LuAG: 1%Pr³+ co-doped with different content of Li⁺.

**Table IV.2** Structural parameters for samples of LuAG: 1%Pr3+ co-doped with different content of K<sup>+</sup>.

**Table IV.3** Structural parameters for samples of LuAG: 1%Pr<sup>3+</sup> co-doped with different content of Na<sup>+</sup>.

**Table IV.4** Structural parameters for samples of LuAG:  $1\%Pr^{3+}$  co-doped with different content of Li<sup>+</sup> / K<sup>+</sup> /Na<sup>+</sup>

9

#### TABLE OF CONTENTS

Acknowledgments	1
LIST OF FIGURES	5
LIST OF TABLES	9
TABLE OF CONTENTS	10
General Introduction	14
Chapter I THEORETICAL BACKGROUND	18
Introduction	19
I.1 Fundamentals of Scintillator Materials: Mechanisms, Properties, and App.	
I.1.1 Radiation-matter interaction	
I.1.2 Scintillator materials	22
I.1.3 Mechanisms of Scintillation	23
I.1.4 Scintillation Parameters	25
I.1.5 Classification of Scintillator Materials	28
I.1.6 Applications of Scintillators	30
I.2 Inorganic Scintillators: Structural and Optical Properties of Garnet System ( $Lu_3Al_5O_{12}$ )	
I.3 Rare Earth Dopants in Garnet Scintillators: Ce <sup>3+</sup> and Pr <sup>3+</sup>	
I.3.1 Ce <sup>3+</sup> -Doped garnet phosphors	
I.3.2 Pr <sup>3+</sup> -Doped garnet phosphors	
I.4 Enhancing Scintillation Performance via Alkaline Metal Co-Doping (Li <sup>+</sup> , N	
I.5. Nanoscale Scintillators: Emerging Opportunities and Challenges	40
Conclusion	44
Chapter II MATERIALS AND METHODS	45
Introduction	46
II 1 Matoriale	47

II.1.1 Starting Materials	47
II.2 Synthesis Methodology	48
II.2.1 Sol-Gel Synthesis Process	48
II.2.2 Optimization of Co-Doping Concentrations	50
II.3. Characterization Techniques	52
II.3.1 Physical Characterization	52
II.3.1.1 X-ray Diffraction (XRD)	52
II.3.1.2 Morphological Analysis	54
II.3.2 Optical Characterization	55
II.3.2.1 Photoluminescence Spectroscopy (PL)	55
II.3.2.2 Radioluminescence (RL)	56
II.3.2.3 Thermally Stimulated Luminescence (TSL)	57
II.3.3 Theoretical Calculations and Simulations	58
II.3.3.1 Density Functional Theory (DFT) Simulations via VASP	58
II.3.3.2 Defect State Calculations	62
Conclusion	63
Chapter III CODOPING EFFECTS ON LuAG:Ce <sup>3+</sup>	64
Introduction	65
III.1 Codoping effects of Li <sup>+</sup> , K <sup>+</sup> , and Na <sup>+</sup> on LuAG:0.5%Ce <sup>3+</sup> scintillating powders	67
III.1.1 Structural analysis	67
III.1.2 VASP simulation	79
III.1.3 Morphological analysis	81
III.1.4 Photoluminescence study	84
III.1.4.1 photoluminescence steady state	84
III.1.4.2 Time resolved photoluminescence	94
III.1.5. Radioluminescence	101
III.1.5.1 Radioluminescence steady state	101

III.1.5.2 Time resolved pulsed radioluminescence	102
III.1.6. Thermally Stimulated Luminescence TSL	104
III.1.6.1 TSL above room temperature	104
III.1.6.2 TSL Measurements at low temperature	106
Conclusion	110
Chapter IV CODOPING EFFECTS ON LuAG:Pr³+	112
Introduction	113
IV.1 Codoping effects of Li <sup>+</sup> , K <sup>+</sup> , and Na <sup>+</sup> on LuAG:1%Pr <sup>3+</sup> scintillating powders	114
IV.1.1 structural analysis	114
IV.1.2 Morphological analysis	119
IV.1.3 Photoluminescence study	121
IV.1.3.1 Photoluminescence steady state	121
IV.1.4 Radioluminescence	128
IV.1.4.1 Radioluminescence steady state	128
IV.1.4.2 Time resolved Radioluminescence	130
Conclusion	131
General Conclusion	133
References	135

# GENERAL INTRODUCTION

#### **General Introduction**

A scintillator is a material that emits light when it absorbs ionising radiation, it is the cornerstone of radiation detection in various fields such as medical imaging (e.g. TAC and PET scanners), security checks, geological exploration and high-energy physics experiments. For over 120 years, their exceptional ability to provide essential parameters such as energy, time and particle identity has made scintillators indispensable [1-5]. Scientists have developed scintillator science in parallel with advances in photodetector technology, as the needs of applications such as high-energy calorimetry, positron emission tomography (PET) in the 1990s and homeland security where high energy resolution has become a key objective have evolved. Prof. Dorenbos classified scintillator technology as having gone through the following four distinct phases: [4,5], first, the discovery era (1900-1940) where the first scintillators, such as ZnS:Ag, were detected by the human eye, then came the innovation driven by PMTs (1940s-1970s) where the introduction of PMTs led to the development of NaI:Tl +, a reference scintillator that is still widely used today, into the lanthanide-doped materials (1970-2000) where the focus was on oxides and halides doped with Ce<sup>3+</sup> or Eu<sup>3+</sup> (for example, LuAG:Ce, LaBr<sub>3</sub>:Ce) to improve light yield and decay times, towards the search for high-energy resolution (after 2000) where research prioritised Ce<sup>3+</sup>/Eu<sup>2+</sup>-doped halides (e.g. SrI<sub>2</sub>:Eu ) and co-doping strategies to minimise non-proportionality [6]. From the various classes of scintillators, garnet-based inorganic materials, in particular lutetium aluminium garnet (Lu<sub>3</sub>Al<sub>5</sub>O<sub>12</sub> or LuAG), have received considerable interest due to their outstanding optical properties, high density and chemical stability. Furthermore, the scintillation characteristics of garnet structures are enhanced by the doping of rare earth ions (RE<sup>3+</sup>), such as Ce<sup>3+</sup> and Pr<sup>3+</sup>.[6-8]. The effectiveness and performance of scintillator materials are determined by a variety of critical parameters, including light yield, decay time, and energy resolution, which are impacted by the structural composition and doping components. Ce<sup>3+</sup> or Pr<sup>3+</sup> activated rare-earth aluminum garnet scintillators, such (Lu,Y)3Al5O12, have bright and fast scintillation characteristics that make them very promising for a variety of field applications. However, defects in the garnet matrix, such as oxygen vacancies and antisite defects which affect scintillation mechanisms, continue to limit their performance. It is widely reported in the literature that one method to address these limitations and enhance structural photoluminescence and scintillation performance is co-doping with monovalent ions Li<sup>+</sup>, Na<sup>+</sup>, and K<sup>+</sup> (particularly lithium). [7,9-17]. In addition, scintillators

need exceptional optical transmission over the emission spectrum to avoid self-absorption, which is typically obtained with wide band gap crystals [19]. However, creating massive single crystals is a costly and time-consuming process that requires specialized lab equipment, extremely pure chemicals, and often long processing periods of up to six months. [10-15]. Regarding these limitations, it is believed that scintillating powders will be perfect for to obtain a low-cost efficient scintillator. Enhancing scintillator performance necessitates precise control of doping ion distribution within the matrix and precise control of particle size in powder forms [25,26].

Various simple chemical synthesis techniques, among them solvothermal synthesis, coprecipitation, sol-gel combustion, spray pyrolysis and sol-gel processing, have been successfully used to produce LuAG:Ce<sup>3+</sup> powders. [27]. Sol-gel synthesis method [5,27-30]. Over the last thirty years, sol-gel methods have emerged as a cost-effective and flexible method for producing advanced materials such as glasses, ceramics, powders, fibres and thin films [31]. Through the use of molecular precursors such as metal alkoxides or acetates, this solution-based technique allows precise control of particle size distribution, shape and composition. A major advantage is its ability to generate homogeneous and very pure nanomaterials, which is particularly important for luminescent applications where emission characteristics depend on dopants such as rare earth or transition metal ions (e.g. Ce<sup>3+</sup>, Eu<sup>3+</sup>) [32]. Moreover, compared with traditional solid-state synthesis, the sol-gel process has several benefits, such as increased improved compositional homogeneity, precursor reactivity, lower sintering temperatures, and scalability [31,33]. Recently, sol-gel chemistry has been shown to be applicable to engineered oxide systems. This method has been successfully used to produce cerium-doped lutetium aluminum garnet (Lu<sub>3</sub>Al<sub>5</sub>O<sub>12</sub>:Ce), a potential scintillator material, by exploiting its ability to obtain both controlled crystallisation and homogeneous distribution of dopants at lower processing temperatures [33].

The objective of this PhD thesis is producing low defect materials via a cost-effective route, by investigating and improving structural, morphological properties and luminescent performance of  $Ce^{3+}/Pr^{3+}$ -Activated  $Lu_3Al_5O_{12}$  (LuAG) Garnet scintillating powders synthetised using sol gel method and codoping them with lithium, potassium and sodium (Li<sup>+</sup>, K<sup>+</sup> and Na<sup>+</sup>).

The motivation for this research arises from the increasing demands for more efficient high-performance scintillators with specific properties. While traditional crystal growth methods frequently face a number of challenges such as high costs and problems with scalability, Sol-gel synthesis provides a cost-effective and versatile solution. Co-doping with Li<sup>+</sup>, Na<sup>+</sup> and K<sup>+</sup> is of special interest due to the ability of these ions to improve structural properties and scintillation efficiency. Furthermore, whereas the separate effects of Ce<sup>3+</sup> and Pr<sup>3+</sup> doping in LuAG have been widely studied, the role of alkali metal codopants in such systems is still in fact still understudied. Closing this research gap is intended to provide a better understanding of how codoping strategies can open up new perspectives for the future of producing high-quality low-defect scintillating powders. In these ways, the results of this research are expected to further contribute to the progress of radiation detection materials.

In order to achieve the objectives described above, this PhD thesis is structured into four chapters, each covering a particular feature of the research.

Chapter one introduces an important overview of scintillating materials, their fundamental properties and their classification. It also reviews the mechanisms governing the scintillation process, including radiation-matter interactions and the role of key performance parameters. A significant focus is given to inorganic scintillators, in particular LuAG, by concentrating on their structural and optical properties, and the effects of Ce<sup>3+</sup> and Pr<sup>3+</sup> doping on garnet-based scintillators is discussed. Lastly, it explores our two motivations and objects, namely the emerging research into alkali metal codoping as a means of improving scintillation efficiency, and discusses the potential benefits and challenges of nanoscale scintillators in modern applications.

Chapter two provides the methodology and experimental methods employed, a detailed presentation of the materials used in this study, including their composition, background information and selection criteria, as well as a detailed description of the synthesis process, paying particular attention to the sol-gel procedure and the optimisation of the codopant concentration required to obtain the necessary structural, morphological and scintillation properties. Furthermore, Experimental set-up for luminescence measurements and calibration of detection equipment is also covered to ensure reproducibility and accuracy, the structural properties and shape of the particles are studied using physical techniques such as X-ray diffraction (XRD), scanning electron

microscopy (SEM) and energy-dispersive X-ray spectroscopy (EDS). Their luminescent performance and trapping characteristics are assessed using optical techniques such as photoluminescence (PL), radioluminescence (RL) and thermally stimulated luminescence (TSL). Finally, theoretical calculations and simulations based on density functional theory (DFT) are used to understand the electrical structure and defect states of codoped garnets and to support the experimental results.

Chapter three is devoted to LuAG:Ce³+ codoped with Li⁺, Na⁺ and K⁺. It covers the effects of codoping focuses on especially the effect of Lithium, on the structural and morphological properties of the powders, as well as steady-state and time-resolved photoluminescence, radioluminescence and thermally stimulated luminescence measurements. It also includes a summary of simulations using the Vienna Ab initio Simulation Package (VASP) to better understand the influence of codopants on material properties and to support the experimental findings.

**Chapter Four** focuses on LuAG:Pr³+ co-doped with Li⁺, Na⁺, and K⁺. Similar to the previous chapter, it examines the structural, morphological and luminescent properties of the materials, in order to outline the differences between the two rare earth dopants.

To summarise, this PhD work explores how codoping strategies can redefine the performance of  $Lu_3Al_5O_{12}$  scintillators. This study not only addresses fundamental scientific questions but also opens new perspectives for the development of high-performance scintillators. Each chapter represents a progressive step in tackling key challenges in materials science, with particular emphasis on advancing the field of scintillating materials.

# **Chapter I**

### THEORETICAL BACKGROUND

#### Introduction

Detecting ionizing radiation is the main application for a scintillator which is a substance that releases light when it absorbs such radiation. Scintillators are essential in many domains and applications including security, medical imaging, geological exploration and high-energy physics, due to their broad spectrum of ionizing radiation detection capabilities and the wide variety of information they provide, including energy, time, and nature of the ionizing species. For almost 120 years, ionizing radiation has been detected and characterized using scintillation materials [6]. Their efficiency and performance depend on several intrinsic characteristics such as the light yield, decay time and energy resolution, in turn influenced by their structural composition and doping elements. Within the different classes of scintillators, garnet-based inorganic materials, in particular lutetium aluminum garnet (Lu<sub>3</sub>Al<sub>5</sub>O<sub>12</sub> or LuAG), have attracted particular attention due to their outstanding optical properties, high density and chemical stability. In addition, doping rare earth ions (RE<sup>3+</sup>) including Ce<sup>3+</sup> and Pr<sup>3+</sup> into garnet structures improves their scintillation properties making them suitable for these applications [17,34,41]. However, no material is ideal and in order to satisfy the rising need for advanced radiation detection systems, additional advancements in performance metrics like light yield and energy resolution are required. Co-doping LuAG with alkali metal ions (Li<sup>+</sup>, Na<sup>+</sup>, and K<sup>+</sup>) is one approach that shows promising results [33,53-57]. and it has been shown to influence the structural and luminescent properties which will be discussed in this chapter.

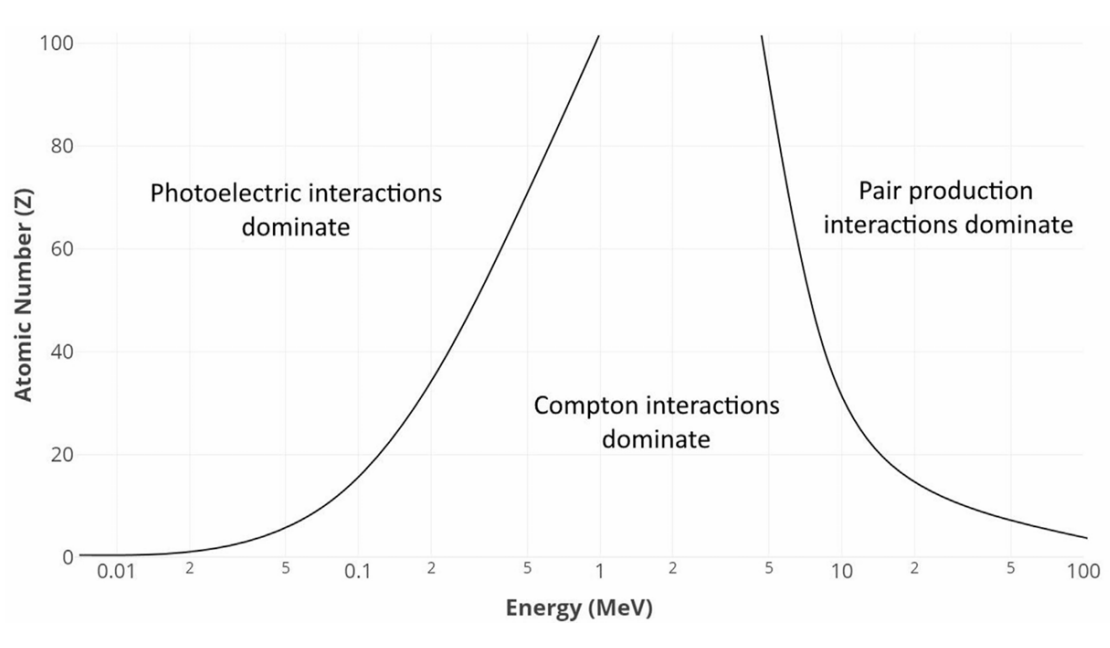
This chapter presents an overview of scintillating materials, their fundamental properties and their classification, it also examines the mechanisms governing the scintillation process including radiation-matter interactions and the role of the main performance parameters. In particular, attention is paid to inorganic scintillators notably LuAG, focusing on their structural and optical characteristics and the effects of Ce<sup>3+</sup> and Pr<sup>3+</sup> doping on garnet-based scintillators is discussed. Finally, this chapter explores our two motivations and objects which are the emerging research into alkali metal codoping as a means of improving scintillation efficiency and discusses the potential benefits and challenges of nanoscale scintillators in modern applications.

# I.1 Fundamentals of Scintillator Materials: Mechanisms, Properties, and Applications

The basis for understanding the difficulties and possibilities in optimizing rareearth-doped garnet scintillators (such as LuAG:Ce³+/Pr³+), which will be looked at in later chapters, is established by placing these principles in context. In addition to clarifying the current state of the art, this summary of concepts, mechanisms, and applications also identifies opportunities for innovation in next-generation radiation detection systems.

#### I.1.1 Radiation-matter interaction

The effectiveness of scintillating materials depends on their ability to convert ionizing radiation into detectable light based on the fundamental interactions between radiation and matter, this is dependent on the type of radiation, its energy and the atomic/structural properties of the material. Here we describe the main physical mechanisms and their implications for scintillator performance. Ionizing radiation can be divided into three main categories, each defined by its physical origin and the mechanism by which it interacts with matter. The charged particles such as alpha particles (helium nuclei), beta particles (high-energy electrons) and protons mainly interact through Coulomb forces causing atoms to ionize by stripping electrons from their orbitals. Uncharged particles such as neutrons which have no physical charge can transfer energy by collision or direct nuclear reactions so their detection depends on secondary charged particles or photon emission. Other electromagnetic radiation including x-rays and gamma rays react through the following three key processes as shown in Figure I.1: the photoelectric effect (absorption of photons and ejection of electrons, dominant in materials with high atomic numbers), Compton scattering (partial transfer of energy to free electrons) and pair production (conversion of photons into electrons and positrons, this interaction is only possible if the energy of the incoming photon is above 1.022 MeV). [34]



J.H.L. Mott, J.M. Daniel / Clinical Oncology 33 (2021) 451-454

**Figure I.1** The three primary photon interaction processes' respective significance in relation to photon energy and atomic number (Z) [34].

Such interaction patterns are important in the manner in which energy is deposited in a scintillating material, which influences critical performance parameters such as detection efficiency and resolution, as an example, high-energy gamma rays tend to favor dense, high-atomic-number scintillators such as lutetium garnet (LuAG), while the detection of neutrons often requires hydrogen-rich (for fast neutrons) or lithium-doped materials to improve capture cross sections (for thermal neutrons). Understanding these phenomena is essential to generating scintillators that are suitable for specific radiation types and applications. When radiation deposits energy, electron-hole pairs are formed, and these pairs migrate along the lattice and thermalize. The parameters of scintillation, which will be covered in section (2.4 Scintillation Parameters), are directly determined by the interaction of ionization density, carrier transport, and activator efficiency. For example, in our case, when doped garnets (LuAG:Ce³+) are exposed to ionizing radiation, the electron-hole pairs generated migrate through the lattice and are captured by activator ions (Ce³+), resulting in radiative recombination and photon emission.

#### I.1.2 Scintillator materials

When matter, whether it be solid, liquid, or gas, emits light without the use of heat, this is known as luminescence. The radiative recombination of an excited energy state to a lower, more relaxed state is the cause of this phenomenon. The system must be raised into this excited state by an external energy source in order to produce light. The specific form of luminescence is determined by the energy source: photoluminescence, electroluminescence, or chemiluminescence, depending on whether light, an electric current, or a chemical reaction is the energy source. Radioluminescence is the technique of irradiating a system with x-rays to produce light emission. In fact, radioluminescence is a particular kind of scintillation in which ionizing radiation is the excitation source.[35]

A material that can transform the energy from absorbed ionizing radiation into UV-visible light is called a scintillator and the associated physical process, scintillation [36] There are many different forms of ionizing radiation and the most commonly detected types are X-rays,  $\gamma$ -rays, neutrons, electrons and  $\alpha$ -particles, while materials that exhibit scintillation are known as scintillators [35] and they are essential parts of detectors for ionizing radiation. There are several different scintillator materials; some are extensively utilized and commercially available, while others are still being researched in labs. Because different applications demand distinct performance characteristics, scintillators come in a variety of forms [35].

Within months following Conrad Röentgen's 1895 discovery of X-rays, the first scintillation material CaWO<sub>4</sub> was employed in an X-ray screen. Over a century ago, this was the first known use of scintillating material. Rutherford's 1911 discovery of the atomic nucleus was aided by scintillation on ZnS-coated screens which was discovered through additional study (Crookes, 1904). ZnS powder, which is still utilized today as a phosphor in lights and televisions was a common scintillation material for nuclear tests by the 1930s. In the beginning, scintillation flashes were visually detected using microscopes, after Robert Hofstadter created NaI and proved that photomultiplier tubes (PMTs) could detect scintillation flashes, inorganic scintillators became widely used in the late 1940s[37] signifying the start of the age of scintillation counters. In the early 1950s, several inorganic scintillators were discovered, including CdWO4,[38] CsI:TI, [39] CsI, [40] CsF, [41] and Lil:Eu,[42]. Over the next two decades, scintillator research slowed, with only a few new materials CsI:Na,[43] CaF2:Eu, [44] and Bi<sub>4</sub>Ge<sub>4</sub>O<sub>12</sub> (BGO) [45] emerging.

However, the demand for high-density and fast-response materials for uses like industrial processes, high-energy physics, and medical diagnostics inspired a renewed curiosity in inorganic scintillators in the 1980s. This advancement was supported by developments in integrated circuits and computation, since newer applications required faster and more accurate data collection. The discovery of the very short emission component in BaF<sub>2</sub> [46,47] and its subsequent explanation [48] launched a search for new fast scintillators utilizing radiative core-to-valence transitions. Several new materials, including BaLiF<sub>3</sub>, KMgF<sub>3</sub>, CsCaCl<sub>3</sub>, etc. have since been developed. Among these, Ce-doped and Ce-based crystals have shown great promise as fast scintillators, leading to the exploration of many new compounds in the search for optimal scintillators[36].

#### I.1.3 Mechanisms of Scintillation

The scintillation mechanism involves multiple complex physical mechanisms, detailed in several studies [49]. The schematic diagram in Figure I.2 shows the scintillation mechanism for rare earth (RE) ion-doped crystals as luminescence enhancers. Because of their complex band structures, RE ions are among the most important groups of scintillators [48]. The scintillation process involves a series of distinct steps, each having a specific time scale:

- 1. **Absorption of ionizing radiation**: Once ionizing radiation, such as X-rays or gamma rays, interacts with the scintillator, it transmits its energy to the material, leaving it in a state of non-equilibrium. As a result, high-energy electrons and internal shell holes are created.
- 2. **Secondary excitation and multiplication**: Primary electrons trigger a cascade of secondary excitations, including electrons, holes, photons and plasmons. Highenergy electrons scatter inelastically, generating additional electron-hole pairs in a process known as multiplication. Electrons of low energy interact with phonons and thermally heat up. At this stage, ionized atoms can either emit photons (radiatively) or release secondary electrons through the Auger effect, with non-radiative decay being the most likely. The process continues until the energy of the particles falls below the ionization level.
- 3. **Electron-hole pair formation and thermalization**: Upon ionization, electron-hole pairs are formed, the number of which is proportional to the energy of the incident radiation. They lose energy as they interact with phonons, stabilizing at energies

- close to the band gap. This process of thermalization is fast with electrons moving to the conduction band and holes to the valence band.
- 4. **Migration of carriers and energy transfer**: Electrons and holes migrate through the material, transferring energy to the luminescent centers, which in turn emit light. The efficiency of this step is dependent on carrier spatial distribution; if the carriers are close to a luminescent center, there is a chance of radiative recombination. Otherwise, they may become trapped in defect sites or impurities, thus delaying scintillation, or even preventing it if deep traps are involved.
- 5. **Light emission and recombination**: The last stage is the recombination of electrons and holes. This can be radiative, leading to the emission of photons, or nonradiative, when the energy is lost as heat. The majority of modern scintillators are extrinsic, which means that luminescent centers such as Ce<sup>3+</sup> are intentionally introduced to enhance radiative recombination. In such materials, efficient energy transfer from the host matrix to the dopant ions leads to intense light emission.

Global scintillation kinetics are determined by the rate of light emission from the excited luminescent centers, which is directly related to the light yield, defined as the amount of light emitted per unit of energy deposited [48].

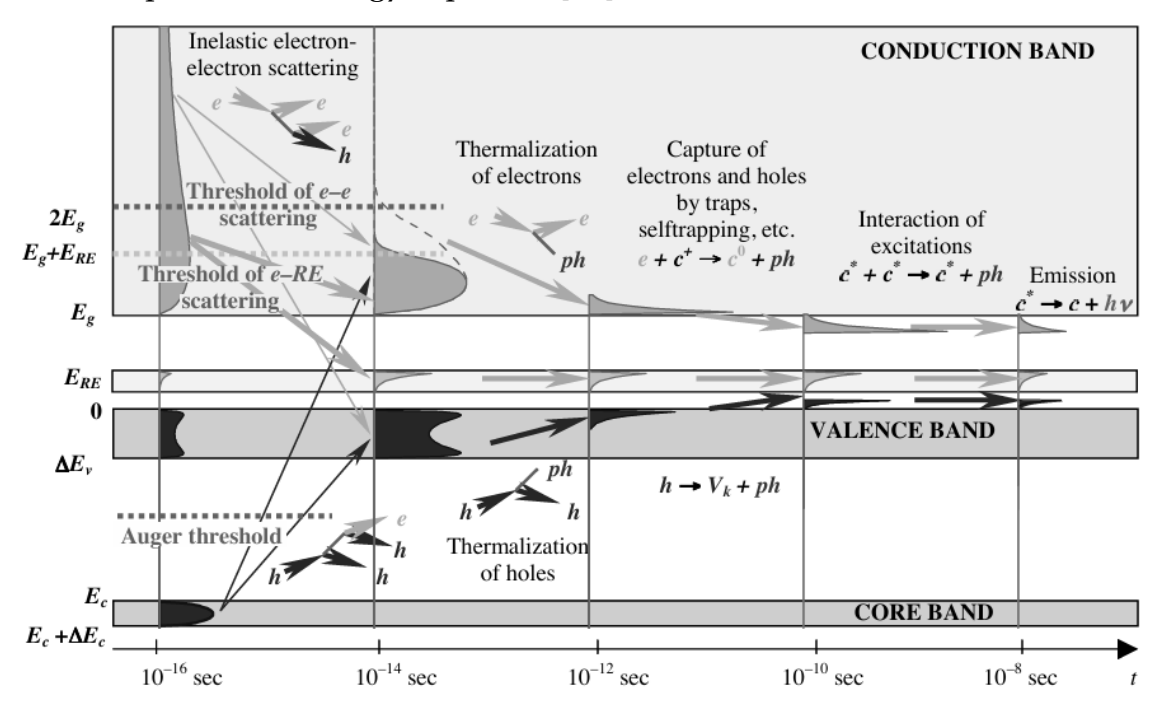


**Figure I.2** A schematic illustration of the scintillation mechanism in an inorganic scintillator. Scintillation process over time, highlighting the progression of particle energy through the various stages that contribute to scintillation emission [48,49].

#### I.1.4 Scintillation Parameters

The applicability of scintillator materials for particular applications is determined by a number of essential factors that quantify their performance. Here, we describe some of these parameters, their physical foundations, and their applications.

#### Light yield

Light yield, the most pivotal metric reflects a scintillator's ability to convert absorbed ionizing radiation energy into detectable ultraviolet or visible photons. It is quantified as:

$$L_R = \frac{N_{ph}}{E_{\nu}}$$
 [Photons/MeV]

where  $N_{ph}$  is the total photons emitted and Ey is the energy being deposited by the interacting gamma photon. For practical comparisons, sodium iodide doped with thallium (NaI:Tl) is the reference standard, with its light yield normalized to 100%. Other scintillators are evaluated relative to this benchmark.

In integrating detection systems, conversion energy efficiency  $(\eta)$  becomes relevant:

$$\eta = \frac{\langle h v_r \rangle N_{ph}}{E_{\gamma}}$$

where  $\langle hv_r \rangle$  is the mean energy of emitted photons.

#### **Scintillation Decay Time**

The decay time ( $\tau$ ) defines the time it take to the scintillation light intensity (I(t)) to drop to 1/e (~37%) of its initial value. For a single exponential decay:

$$I(t) = I(0). e^{-\frac{t}{\tau}}$$

Shorter decay times ( $\tau$ <100 ns) are critical for high-count-rate applications (e.g., time-of-flight PET). Real-world scintillators often exhibit non-exponential decay due to energy transfer between luminescent centers or quenching effects. These are empirically modeled as a sum of exponentials:

$$I(t) = \sum_{i} I_{i}(0). e^{-\frac{t}{\tau_{i}}}$$

#### **Energy resolution**

Energy resolution (*R*) determines a detector's ability to distinguish between closely spaced photon energies (**Figure I.3**). It is defined as:

$$R = \frac{\Delta E}{E} \times 100 \, [\%]$$

where  $\Delta E$  is the full width at half maximum (FWHM) of the photopeak at energy E (typically measured using a  $^{137}$ Cs source). Superior resolution (lower R) enhances spectroscopic accuracy.

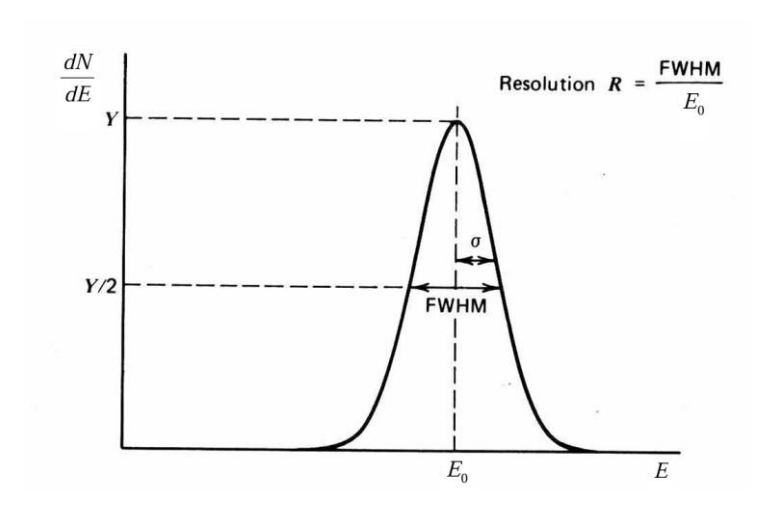


**Figure I.3** Pulse heigh spectrum. Definition of detector resolution [50].

#### **Density**

For gamma-ray detection and spectroscopy, inorganic heavy crystals are generally used due to their high density, which enhances interaction with ionizing radiation and enables efficient energy absorption in compact scintillators. For the detection of low-energy X-rays and gamma rays (<800 keV), materials with high atomic numbers (Z) are preferred, as the photoelectric effect ( $\sigma_{ph} \propto Z^5$ ) dominates the Compton effect ( $\sigma_{c} \propto Z$ ). In contrast, for the detection of high-energy beta rays, dense materials are required, although extremely high-Z components are less favorable due to increased backscatter. For medical dosimetry, tissue-equivalent scintillators with lower Z are essential to accurately reproduce the response of human tissue during dose measurements [50].

#### Afterglow

Afterglow refers to delayed luminescence caused by thermal release of charge carriers from defect-related traps. Its intensity and duration depend on defect concentration, irradiation dose, and temperature. Mitigation strategies include trap-state engineering (e.g., co-doping with Li<sup>+</sup>) and high-purity crystal growth.

#### Operational parameters durability

Radiation hardness or the long-term durability of the operating parameters is a crucial characteristic needed in most applications. Radiation damage is always the outcome of interactions between ionizing radiation and a scintillator, while the complex mechanism that causes radiation damage includes the host material as well as any impurities or flaws in the substance. These inhomogeneities raise the likelihood that radiation-induced point defects or color centers will occur in the crystal. The incident radiation may change the optical and scintillation properties of the crystal both while and after high doses are delivered. Irradiation can modify the scintillator's features in a number of ways, including the formation of color center absorption bands, the direct effect of radiation on luminescent centers, and changes to emission parameters (efficiency, spectrum, decay time). the creation of shallow traps that increase the level of afterglow, etc.

#### **Emission spectrum**

The emission spectrum describes the wavelength-dependent distribution of photons generated by a scintillator. Optimal detector efficiency requires spectral overlap between the scintillator's emission and the photosensor's quantum efficiency. For example: Photomultiplier Tubes (PMTs): Bialkali photocathodes peak at 280–500 nm (e.g., NaI:Tl, CsI:Tl) and Silicon Photodiodes: Efficient in the near-infrared (500–1100 nm; e.g., Ce³+doped garnets). Signal-to-noise ratios are directly impacted by mismatched spectra, which decrease photon gathering efficiency. Therefore, in order to meet detector requirements, material design must strike a compromise between host bandgap engineering and activator selection.

Finally, selecting a scintillator for a given application requires consideration of numerous additional features. We can recall the following: proportionality of response, cost, mechanical qualities (hardness, ruggedness, cleavage, etc.), index of refraction, hygroscopicity, thermal stability, transmission, etc.[3,4,20-23].

#### I.1.5 Classification of Scintillator Materials

Based on their composition, scintillation mechanism and performance in a particular application, scintillator materials are often divided into several categories. The main classes, their distinguishing traits, and their technological expertise are described below.

#### **Inorganic Scintillators**

Crystalline or ceramic materials with high densities, high effective atomic numbers ( $Z_{\rm eff}$ ), and effective energy conversion through activator ions (such as rare earths or transition metals) are known as inorganic scintillators. Among them that of rare earth doped scintillators are the most popular, particularly  $Ce^{3+}$  and  $Pr^{3+}$  ions.[3,4,15,21,24-27].

Single crystals	Ceramics	Glasses
NaI(Tl),CsI(Tl),Lu <sub>3</sub> Al <sub>5</sub> O <sub>12</sub> :Ce <sup>3+</sup> ,	$Gd_2O_2S:Pr^{3+}$ , $(Y,Gd)_3Al_5O_{12}:Ce^{3+}$	Ce³+-doped borosilicate glasses
$Gd_3Al_2Ga_3O_{12}$ : $Ce^{3+}$		
High light yield	Polycrystalline structure	Amorphous structure
High energy resolution Radiation	Cost-effective manufacturing,	Tunable composition
hardness	Moderate light yield	Low light yield
Medical imaging (PET/CT),	X-ray computed tomography	Neutron detection
High-energy physics calorimetry	(CT), security scanners	Radiation dosimetry

#### **Organic Scintillators**

Molecular fluorescence is the basis for organic materials which have fast decay rates ( $\tau$ <10 ns) but lower densities and  $Z_{\rm eff}$  [59,60,61].

Pure organic crystals	Plastic scintillators	Liquid scintillators
Anthracene	Polystyrene/polyvinyl toluene	Linear alkylbenzene (LAB) with
Stilbene	doped with p-terphenyl	fluorophores
High fluorescence efficiency	Moldable	Homogeneous detection medium
Hygroscopic and fragile	Lightweight	Scalable volumes
	Radiation-resistant	
	Particle physics (muon detection)	Neutrino experiments (e.g., Super-
	Radiation monitoring	Kamiokande)

#### **Hybrid and Nanoscale Scintillators**

New classes that use nanoscale phenomena or combine inorganic and biological components [62,63]:

Perovskite-Based Scintillators	Nanocomposites	Quantum Dots
CsPbBr <sub>3</sub> nanocrystals	Ce <sup>3+</sup> -doped garnet nanoparticles in polymer matrices	CdSe/ZnS core-shell nanocrystals
Tunable emission spectra	Flexibility	Size-tunable emission
Solution-processable.	Reduced self-absorption	High quantum yield
Poor stability under irradiation	Wearable radiation sensors	Multispectral X-ray imaging

However, image resolution is affected by inorganic scintillator afterglow and expensive production costs. More research is being done on co-doping with ions like Li<sup>+</sup> to inhibit trap states.[14,64,65]. Our work has developed co-doped LuAG:Ce/Pr powders using the low cost sol-gel process to address these issues and provide improved performance for advanced radiation detection at reasonable prices.

#### I.1.6 Applications of Scintillators

Scintillator materials are essential to modern radiation detection technologies and play important roles in a variety of fields, including industrial process monitoring, oil well logging, high-energy physics (e.g., calorimeters in particle colliders), homeland security (e.g., cargo inspection), and medical imaging (e.g., PET/CT scanners). Due to their unparalleled density, scintillation efficiency and response time, inorganic scintillators dominate both research and commercialization efforts, with a global market estimated to be worth over \$350 million in 2015. For applications that need fast, high-resolution detection, such real-time tumor tracking in radiotherapy or detecting fissile materials in security screenings, these criteria are essential. Heavy-metal hosts such as lutetium-based garnets (e.g., LuAG) activated by Ce³+ or Pr³+ have been the subject of much research in order to meet these demands.[56] Below, we go over a few of these applications fields.

#### Medical

Scintillators have been a vital part of medical imaging since 1895, when BaPt(CN)<sub>4</sub> was accidentally used to detect x-rays, producing the first radiographic image and revolutionizing diagnostics by enabling internal body vision. By transforming x-rays into visible light and enhancing the sensitivity of photographic film, intensifying screens also referred to as x-ray phosphors such as ZnS and CdWO<sub>4</sub> were created to improve x-ray detection. Digital imaging, x-ray videography, and contemporary 3D imaging devices like CT scanners were made possible by developments in scintillating materials and photodetectors. Scintillators are used in nuclear imaging methods such as PET and SPECT to identify gamma photons released by radiotracers that target particular tissues. Traditional BGO scintillators have been replaced by faster materials like LYSO and LSO (Lu<sub>2</sub>SiO<sub>5</sub>:Ce<sup>3+</sup>) because of their better performance. Scintillators which are frequently combined with optical fibers for precise detection, are also utilized in medical dosimetry for real-time radiation dosage monitoring during radiotherapy. These developments demonstrate how crucial scintillators are to radiation-based therapies and medical imaging [35,36,54,56].

#### **Homeland security**

Scintillating materials are essential for radiography imaging at border checkpoints and airports in homeland security. distinct x-ray energies are utilized to figure out item densities which are shown as distinct colors on security displays, with less restriction on radiation doses than medical imaging. Due to the larger volume of material, larger objects like cars need more penetrating gamma rays. The control of the movement of radioactive materials has become an absolute priority since the events of 11 September 2001. The latest systems can use real-time gamma-ray spectrometry, placed in high-traffic areas such as ports, borders and motorways, to identify specific isotopes of strategic importance, as well as radioactive items. High resolution scintillators with constantly improving capabilities, make this possible [35,36,54,56].

#### **High energy calorimetry**

In particle physics studies, where secondary particles are created by high-energy particle collisions and measured by calorimeters, scintillating materials are essential. These calorimeters which combine scintillators and photodetectors can detect particles with energy as high as TeV and need a lot of material to be effective. Electromagnetic showers are produced by high-energy interactions which calls for sophisticated detection systems that spur advancements in other domains like medical imaging. With varying performance requirements, scintillators are also utilized in space exploration, oil drilling, nuclear power plant control, radon detection, nuclear waste management, homeland ecological monitoring and industrial quality control [35,36,54,56].

## I.2 Inorganic Scintillators: Structural and Optical Properties of Garnet Systems (Lu<sub>3</sub>Al<sub>5</sub>O<sub>12</sub>)

Because of their hardness, garnets have been used for thousands of years as abrasives. Since the Bronze Age, they have also been used as jewels because of their high refractive index and beautiful color, which are the result of transition metal ions being inserted into tetrahedral or octahedral positions. The name "Garnet" in English comes from the Latin "Granatum" which means "many grains". It is related to the pomegranate fruit, which has a lot of red seeds that are structurally and color-similar to some dark red garnet gemstones [66]. Menzer's 1928 identification of the structural features of garnet-type compounds marked the beginning of research on these compounds, because of their complicated cation arrangement in their unit cell and cubic crystal structure, garnets can have their luminescent properties highly tuned by varying the {A}, [B], and (C) cation sublattices, it have a general stoichiometric formula of A<sub>3</sub>B<sub>2</sub>C<sub>3</sub>O<sub>12</sub>, where A, B and C represent distinct cation sublattices: A occupies dodecahedral sites (X sites), which can accommodate rare-earth ions like Y<sup>3+</sup>, Lu<sup>3+</sup>, Gd<sup>3+</sup>, Tb<sup>3+</sup>, or La<sup>3+</sup> as well as divalent ions like Ca<sup>2+</sup>. B Fills octahedral sites (Y sites) and can accommodate Al<sup>3+</sup>, Ga<sup>3+</sup>, Sc<sup>3+</sup>, Sb<sup>3+</sup> or In<sup>3+</sup> as well as ions with various charges like Mg<sup>2+</sup> or Mn<sup>2+</sup>. C occupies tetrahedral sites (Z sites) and generally includes Ga<sup>3+</sup> or Al<sup>3+</sup> but can also retain Si<sup>4+</sup>, Ge<sup>4+</sup> or Mn<sup>2+</sup> ions while preserving the garnet crystal structure [67,68]. The luminescent characteristics of host materials are intimately related to their crystal structure, with cell characteristics of a = b = c = 11.906 Å for Lu<sub>3</sub>Al<sub>5</sub>O<sub>12</sub> and a = b = c = 12.008 Å for comparable compounds, LuAG, or Lu<sub>3</sub>Al<sub>5</sub>O<sub>12</sub> has a cubic structure inside the Ia3d space group (230). A  $1 \times 1 \times 1$ LuAG unit cell is seen in Figure I.4 While Al3+ ions occupy two types of lattice sites sixcoordinated AlO<sub>6</sub> octahedra and four-coordinated AlO<sub>4</sub> tetrahedra joined by shared O<sup>2-</sup> ions Lu<sup>3+</sup> ions are coordinated with eight O<sup>2-</sup> ions, forming a dodecahedron symmetry D<sub>2</sub>d. For Lu<sup>3+</sup>, the effective ionic radii are 0.977 Å, for Al<sup>3+</sup> they are 0.535 Å, and for Mn<sup>4+</sup>, they are 0.53 Å. LuAG's Mn-O bond length is 1.864 Å. By replacing Lu with Y, the lattice parameters are increased, reduces Mn-Mn interactions and weakens the crystal field surrounding Mn<sup>4+</sup>, for instance by increasing atomic spacing. The fine tailoring of optical characteristics is made possible by LuAG's compositional flexibility.

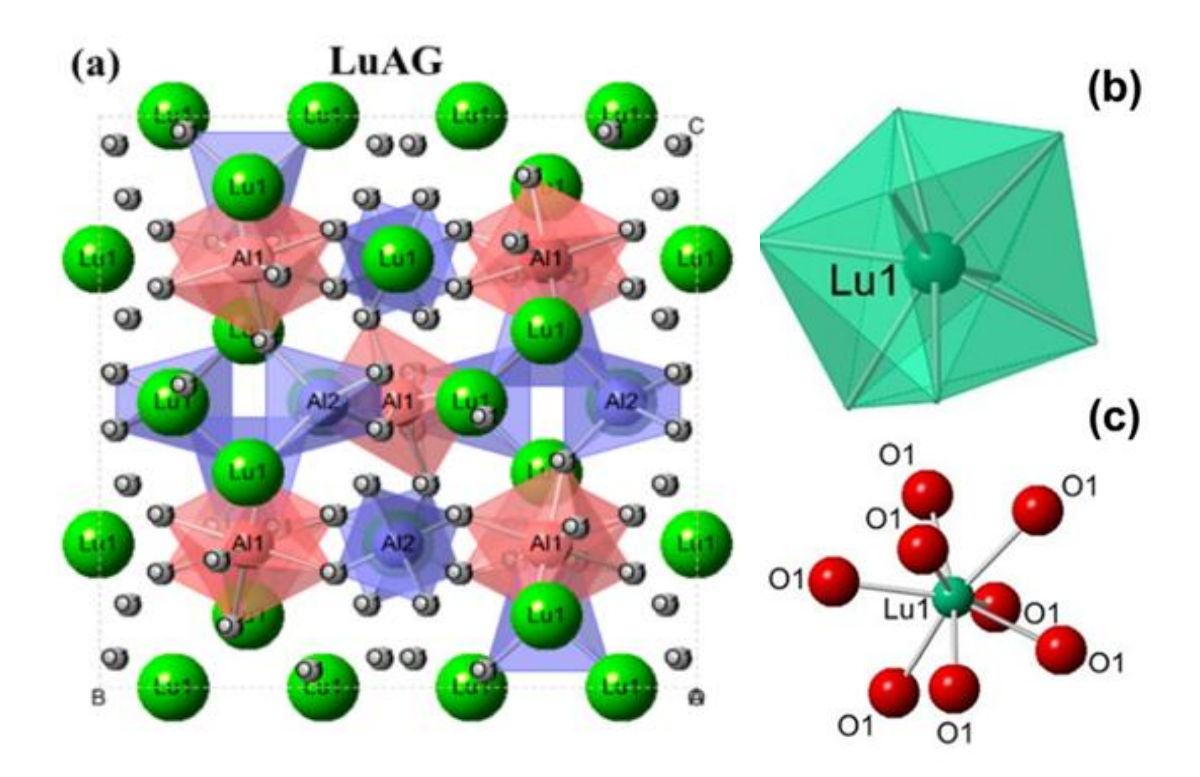


**Figure I.4** Unit cell illustration of  $Lu_3Al_5O_{12}$  crystal structures (a) Aluminum site of  $Lu_3Al_5O_{12}$  (c) [69].

It is crucial to comprehend the "Structure-Property Relationship" in order to create new useful materials and acquire more profound physical understanding, the foundation for adjusting material properties and finding novel phosphors for cutting-edge applications is crystal chemistry. A crucial class of inorganic materials, garnets are incredibly adaptable in functional applications due to their complex chemical composition and straightforward cubic crystal structure [66], due to its exceptional physicochemical characteristics, garnet is a well-known optical host material with great potential in applications like lasers, lighting, scintillation and magneto-optic devices. A range of rareearth and transition metal ions can be included into its lattice structure providing various doping sites that enable fine-tuning of its characteristics and precise control over local sites [70].

#### I.3 Rare Earth Dopants in Garnet Scintillators: Ce3+ and Pr3+

The process by which an ion, molecule or atom is activated by absorbing photons of a particular energy and then returns to its ground state by emitting photons is known as luminescence. Only specific elements can be used as phosphors, or optically active centers in luminescent materials. Lanthanides, yttrium and scandium are among the rare earth ions that are most frequently utilized in light-emitting materials for technical purposes [9,57,71]. The elements in the lanthanide series (Ln), which are found at the bottom of the periodic table, have electrons in their inner 4f shell, with an electron configuration of [Xe] 4f<sup>n</sup> for Ln<sup>3+</sup> ions, 3+ is the most prevalent and stable valence state for lanthanides and the number of electrons in the 4f shell denoted by n, ranges from 0 (an empty 4f shell) to 14 (a fully filled 4f shell) [66].

Aluminum garnet scintillators are usually doped with ions like  $Ce^{3+}$  or  $Pr^{3+}$  to produce fast and efficient light through 5d-4f transitions within the material's forbidden energy band (**Figure I.5**). The  $Pr^{3+}$  4f-5d absorption bands are located between the host lattice absorption and the  $Ce^{3+}$  absorption bands. The 5d-4f emission bands of  $Pr^{3+}$  and the absorption bands of  $Ce^{3+}$  overlap [73].

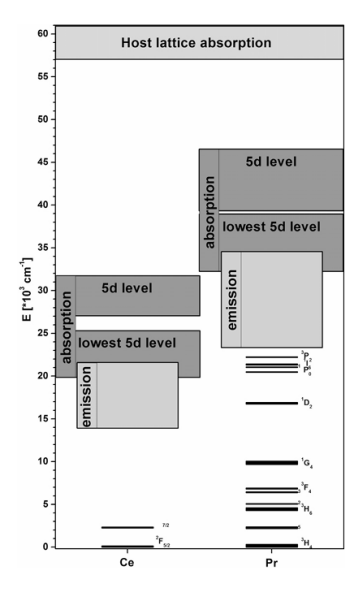


**Figure I.5** Trivalent Ce and Pr ions' 4f energy levels, as well as their 4f-5d absorption and emission bands, are displayed in the Dieke diagram [73].

#### I.3.1 Ce<sup>3+</sup>-Doped garnet phosphors

The electronic configuration of the trivalent cerium ion (Ce<sup>3+</sup>) is expressed as [Xe]  $4f^1$  6s<sup>2</sup>. Its ground state  $4f^1$  is split into two sublevels,  $2F_{5/2}$  and  $2F_{7/2}$ , due to spin-orbit coupling, with an energy separation of around 2000 cm-<sup>1</sup> (~0.25 eV). The excited state configuration,  $5d^1$ , undergoes splitting in the presence of a crystal field, resulting in two to five distinct components, as illustrated in figure 2.4. The total splitting energy of the crystal field reaches around 15,000 cm-<sup>1</sup> (~1.86 eV) [50,66,74-77].

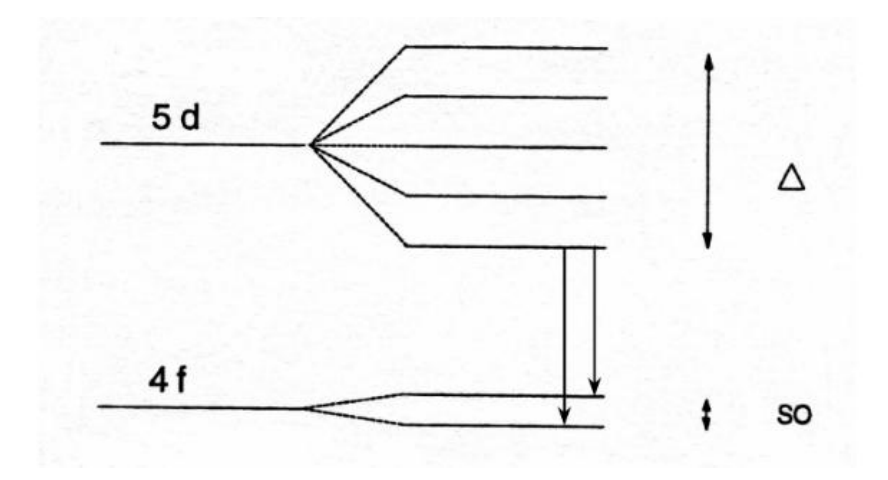


**Figure I.6** A simplified diagram of the energy levels of the Ce<sup>3+</sup> (4f<sup>1</sup>) ion. On the left, only the 4f and 5d electronic levels are shown, without taking into account additional interactions. On the right, the effects of spin-orbit coupling (SO) and crystal field splitting are illustrated. The spin-orbit interaction divides the 4f level into two sublevels, separated by around 2000 cm<sup>-1</sup>. The crystal field effect (Δ) divides the 5d level into five distinct components, covering an energy range of around 15,000 cm<sup>-1</sup> [66].

Ce³+-doped garnet phosphors are extensively used for a variety of applications in many fields, reflecting their versatility and unique properties. Some of the common applications for these materials are illustrated in **Figure I.7**, covering areas such as indoor and outdoor lighting, display backlights, solid-state lasers, flying spot scanning systems, traffic and automotive lights, plasma display panels, remanence materials, the dye industry, scintillators for medical imaging and homeland security, as well as transparent ceramics. **Table I.1** provides a summary of the main Ce³+-doped garnet phosphors, highlighting their chemical composition, photoluminescence (PL) and photoluminescence excitation wavelengths (PLE), as well as their specific applications [66].



**Figure I.7** Representative application areas for Ce<sup>3+</sup>-doped garnet phosphors [66].

**Table I.1** the applications of various Ce<sup>3+</sup>-doped garnet phosphors [66].

Application	<b>Chemical Composition</b>	$\lambda_{ex}$ (nm)	$\lambda_{em}$ (nm)
w-LED Phosphors	Y <sub>3</sub> Al <sub>5</sub> O <sub>12</sub> : Ce <sup>3+</sup>	470	532
	$Lu_3Al_5O_{12}$ : $Ce^{3+}$	440	505
	$Ca_3Sc_2Si_3O_{12}$ : $Ce^{3+}$	455	505
	$Tb_3Al_5O_{12}$ : $Ce^{3+}$	470	553, 620
	$Y_3Al_4GaO_{12}$ : $Ce^{3+}$	450	519
	$Y_3Sb_2Al_3O_{12}$ : $Ce^{3+}$	465	528
	$Y_3Al_{5-x}Si_xO_{12-x}N_x$ : $Ce^{3+}$ (x=0.1)	470	620-630
	$Y_3Mg_2AlSi_2O_{12}$ : $Ce^{3+}$	440	600
	CaLu <sub>2</sub> Mg <sub>2</sub> (Si, Ge) <sub>3</sub> O <sub>12</sub> : Ce <sup>3+</sup>	470	605
	CaLu <sub>2</sub> Al <sub>4</sub> SiO <sub>12</sub> :Ce <sup>3+</sup>	450	510-530
	$Mg_3Y_2Ge_3O_{12}$ : $Ce^{3+}$	466	555
	$MgY_2Al_4SiO_{12}$ : $Ce^{3+}$	452	566
	$Lu_3(Al,Mg)_2(Al,Si)_3O_{12}:Ce^{3+}$	450, 462	542-571
	$Ca_2GdZr_2(AlO_4)_3:Ce^{3+}$	417	500
	Ca <sub>2</sub> LaZr <sub>2</sub> Ga <sub>3</sub> O <sub>12</sub> : Ce <sup>3+</sup>	430	515
	$Ca_3Hf_2SiAl_2O_{12}:Ce^{3+}$	400	508
Scintillators	$Lu_3Al_5O_{12}$ :Ce <sup>3+</sup>	440	505
	$Tb_{2.2}Lu_{0.8}Al_5O_{12}$ : $Ce^{3+}$	459	565
	(Lu, Gd) $_3$ (Ga, Al) $_5$ O $_{12}$ :Ce $^{3+}$	345	530
	$Gd_3$ (Al, $Ga)_5O_{12}$ : $Ce^{3+}$	445	540-565
Afterglow Phosphors	$Y_3Sc_2Ga_3O_{12}$ : $Ce^{3+}$	440	500
	$Y_3Sc_2Ga_{3-x}Al_xO_{12}$ : $Ce^{3+}$	414	503
	$Mg_3Y_2(Ge_{1-x}Si_x)_3O_{12}$ : $Ce^{3+}$	455	580-595

#### I.3.2 Pr<sup>3+</sup>-Doped garnet phosphors

Pr<sup>3+</sup> is among the most versatile optically active ions, capable of emitting luminescence across a wide spectral range, from deep ultraviolet (UV) to visible and infrared regions [76]. Notably, it was the first ion shown to exhibit two-photon emission following vacuum ultraviolet (VUV) excitation [79]. Pr<sup>3+</sup> ions, in some host matrices, exhibit intense and fast luminescence due to the interconfigurational  $5d \rightarrow 4f$  emission transition [80]. Aluminum garnets are recognized as strong contenders for scintillator applications among various oxide materials, owing to their advanced development for laser hosts and features like optical transparency and ease of rare-earth doping. Lu<sub>3</sub>Al<sub>5</sub>O<sub>12</sub> garnets doped with Pr<sup>3+</sup> (LuAG) are a particularly attractive choice among them for attaining extremely effective scintillation [80]. As shown in Figure I.8, the Pr<sup>3+</sup> ion has an electron configuration of [Xe] 4f<sup>2</sup> and a complicated energy level structure that reaches up to about 25,000 cm<sup>-1</sup>. Its emission spectra can include transitions from the <sup>3</sup>P<sub>0</sub> and <sup>3</sup>D<sub>2</sub> levels, resulting in green-blue and red emissions, respectively, when excited by UV or visible light [81,82]. However, these emissions come from  $4f \rightarrow 4f$  transitions, which exhibit slow radiative decay, making them particularly unsuitable for scintillator applications where fast response times are required. In contrast, the  $5d \rightarrow 4f$  transitions in Pr<sup>3+</sup> are allowed by the electric dipole and much faster, making them more relevant for efficient scintillation. In addition,  $Pr^{3+}$  also exhibits a range of  $4f \rightarrow 4f$  transitions in the infrared (IR) spectrum, particularly from the <sup>1</sup>G<sub>4</sub> level upwards, which are valuable for other optical applications such as lasers and amplifiers [83]. Nevertheless, as far as scintillator performance is concerned, the focus remains on the faster  $5d \rightarrow 4f$ transitions.

**Figure I.8** The Pr<sup>3+</sup> ion's energy level scheme is made up of a dense network of energy levels that stretch up to about 25,000 cm<sup>-1</sup> [81].

## I.4 Enhancing Scintillation Performance via Alkaline Metal Co-Doping (Li<sup>+</sup>, Na<sup>+</sup>, K<sup>+</sup>)

Bright and fast scintillation properties of  $Ce^{3+}$  or  $Pr^{3+}$  activated rare-earth aluminum garnet scintillators such as  $(Lu,Y)_3Al_5O_{12}$  have made them highly promising for several fields applications as mentioned in section (2.6 applications of scintillators) . However, their performance remains limited by defects present in the garnet matrix, these defects, like oxygen vacancies and anti-site defects, impact the scintillation performance. Co-doping with monovalent ions  $Li^*$ ,  $Na^*$ , and  $K^*$  (specially Lithium) is one way to move these defects and improve structural photoluminescence and scintillation performance. This approach fits with one of our primary objectives, which is to look into the possibility of using alkaline metal co-doping by different content of  $Li^*$ ,  $K^*$  and  $Na^*$  to improve scintillation characteristics on  $LuAG:Ce^{3+}$  and  $LuAG:Pr^{3+}$  powders. A table summarizing previous research on the effects of co-doping with these ions and showing recent developments in garnet-based scintillators will be presented in this part.

**Table I.2** Summary of previous studies on the effects of Li<sup>+</sup>, Na<sup>+</sup>, and K<sup>+</sup> co-doping on the structural, photoluminescent, and scintillation performance of Ce<sup>3+</sup>- and Pr<sup>3+</sup>-doped garnet materials.

Study	Co-doping	Results
	pair	
A. K. Singh et	Li <sup>+</sup> codoping	- Boosts efficiency in both photoluminescent and
al.	Lanthanide	radioluminescent systems.
(2014) [10]	ions Ce³+ and	- Improved crystallinity, smoother surfaces, and
	Eu <sup>2+</sup> in Y <sub>2</sub> O <sub>3</sub> and	larger grains enhance material quality.
	$Gd_2O_3$	- Rare-earth activators populate crystal sites that
		maximize radiative pathways.
		- Charge compensation preserves the luminescent
		valence state of dopants (e.g., Eu³+, Ce³+).
		- Increased vacancies mediate energy transfer to
		activators, acting as sensitizers.

		- Lattice distortion enhances radiative transition
		probabilities, even for typically forbidden 4f→4f
		transitions.
K. Kamada et	Li⁺ codoping on	- Enhanced energy resolution.
al. (2016) [11]	GGAG: Ce <sup>3+</sup>	- Faster scintillation decay time.
K. Kamada et	LuAG: Ce <sup>3+</sup>	- And/or greater light output.
al. (2017) [12]	YAG: Ce <sup>3+</sup>	
Peter T.	Li cooping on	- Li <sup>+</sup> co-doping elevates light output, even under
Dickens et al.	$Ce_x:Y_{3-x}Al_5O_{12}$	high alumina (10% excess) conditions.
(2017) [65]	single crystal	- Long-decay emissions are reduced (trap
	Czochralski	suppression), while fast decay kinetics remain
	(CZ) method	stable.
		- Li <sup>+</sup> improves Ce <sup>3+</sup> transition efficiency (via PL)
		and reduces parasitic traps, synergistically
		enhancing scintillation.
M.V.	Li+ codoping	- In YAG:Ce, Li <sup>+</sup> ions migrate to interstitials with
Derdzyan et	on YAG:Ce and	charge compensation achieved by reducing anion
al.	LuAG:Ce	vacancies rather than replacing any lattice site or
(2018) [84]	polycrystalline	forming complexes with Ce.
	samples	- Li <sup>+</sup> ions in LuAG:Ce,Li do replace Lu <sup>3+</sup> sites, and
	prepared by	the production of O hole centers and the
	solid phase	conversion of Ce³+ to Ce⁴+ help achieve charge
	reactions;	balance.
	single crystals	- The scintillation decay characteristics of YAG:Ce
	grown by the	do not seem to be improved by Li co-doping;
	vertical	nonetheless, it might be helpful in lowering the
	Bridgman	amount of anion vacancies in YAG and YAG:Ce as
	method.	well as in enhancing transparency and UV
		resistance to X-ray irradiation.

Li <sup>+</sup> ,Na <sup>+</sup> , and K <sup>+</sup>	- LuYAG:Pr , Na achieved 34,000 ph/MeV light
cooping on	yield and 3.8% energy resolution (best-in-class for
$(Lu_{0.75}Y_{0.25})_3Al_5O_{12}$	oxides).
(LuYAG: Pr³+)	- Reduced afterglow via trap removal at 300 K
single crystals	(evidenced by thermoluminescence (TL) curve
Czochralski	analysis).
growth	- Monovalent co-dopants (e.g., Na⁺) mitigate
	parasitic traps and stabilize radiative pathways.
	- Positions LuYAG:Pr , Na as a leading material for
	precision radiation detection technologies.
	cooping on $(Lu_{0.75}Y_{0.25})_3Al_5O_{12}$ $(LuYAG: Pr^{3+})$ single crystals Czochralski

#### I.5. Nanoscale Scintillators: Emerging Opportunities and Challenges

The development of nanoscale scintillators and further research into their scintillation behavior at smaller dimensions has been stimulated by the progress made over the last ten years in the field of light-emitting nanostructured materials. Unlike bulk single crystals, complex processes are involved in the dissipation of energy in nanoparticles (NPs), where the repetitive motion of electrons and holes created by primary and subsequent excitation events frequently transcends the physical boundaries of the nanoparticle, implying that some of the energy that has been deposited is displaced and lost to the immediate environment [85]. The design of new highly efficient scintillator crystals and materials for the detection of ionizing radiation is at the focus of current research efforts worldwide, with a concentration on applications in medical diagnostic imaging [86-91]. NaI:Tl<sup>+</sup>, CsI:Tl<sup>+</sup>, Bi<sub>4</sub>Ge<sub>3</sub>O<sub>12</sub> (BGO), BaF<sub>2</sub>:Ce<sup>3+</sup>,  $Y_3Al_5O_{12}$ :Ce<sup>3+</sup> (YAG:Ce<sup>3+</sup>), lithium molybdate, YAG:Yb, and Tl<sub>2</sub>GdCl<sub>5</sub>:Ce<sup>3+</sup> are examples of inorganic scintillators [21,76,93-96]. Ionizing radiation detection is carried out by coupling a scintillator material with a conventional light detector, usually a photomultiplier tube (PMT), which measures the photons released, as shown in Figure I.9. Indeed, most scintillation research has focused on the visible photon emissions that PMTs can easily detect. The creation of crystalline powder scintillators is an alternative to expensive single crystals. Microcrystalline scintillator powders (MSPs), on the other hand, are generally limited to uses such as photostimulable storage displays and traditional X-ray screens [20,21,97,98]. This restriction results from MSPs' porous structure, which

scatters light and produces opacity [19,21]. Furthermore, MSPs' poor compatibility with gels and polymers limits their economic viability. Although they work well with polymer matrices, organic scintillators are incompatible with <sup>6</sup>Li, which makes them inappropriate for use as neutron scintillators [99]. Considering these limitations, it is expected that nano-scintillator powders (NSPs) will be ideal for sophisticated radiation detectors, which will find use in nuclear reactor radiation monitoring, security inspections, and medical diagnostics [100].

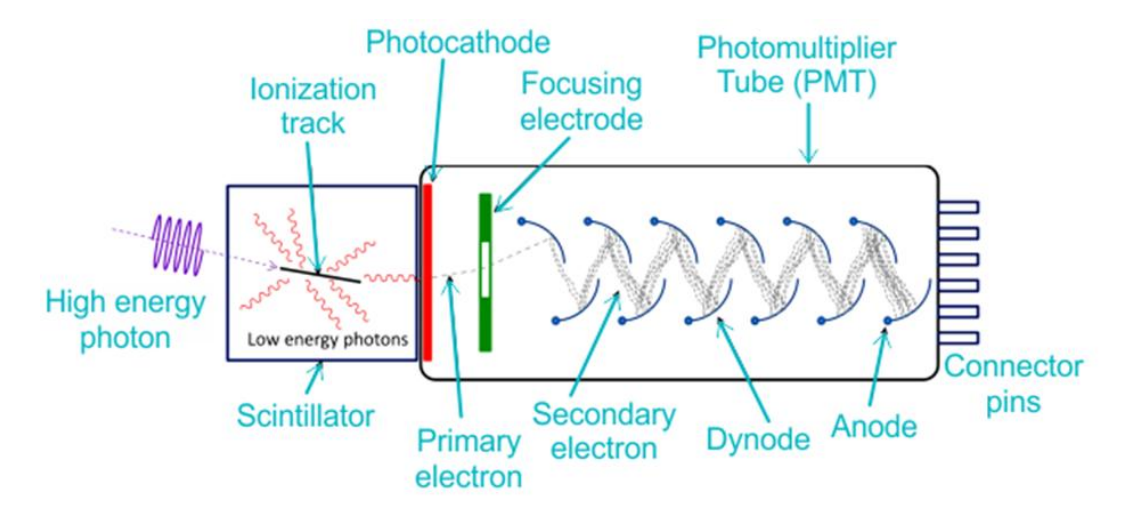


**Figure I.9** Diagram of a scintillation counter [85].

Controlling the scintillating material at the nanometric scale is an efficient way to improve scintillator performance. This calls for careful control of particle size in powder forms as well as accurate management of doping ion dispersion within the matrix. The intensity of X-ray-excited luminescence can be limited by the size of the nanoparticle, according to research on the radioluminescence of fluoride, oxide, and phosphate-based nanoparticles [26]. The content, size, and structure of nanoparticles (NPs) affect the design of nano scintillators. Surface forces produced in by smaller particles change structural characteristics, affecting bond angles and lattice constants and producing variations from bulk materials. Depending on which orbitals are involved, the influence may be more or less intense; for example, inner 4f orbitals may be more or less affected than outer 5d orbitals. **Figure I.10** illustrates the shifts in emission spectra between the bulk materials and the nanoparticles. In certain circumstances, this effect can have a major impact on luminescent properties, for example, the relative position between the  $4f^2$   $^1S_0$  state and the lowest level of the excited  $4f^1$   $5d^1$  configuration determines the

emission level of the Pr³+ ion [101-103]. Thus, depending on the size of the nanoparticle, this emission level may change in Pr³+-doped nanoparticles [104]. As shown in **Figure I.11**, where concentration quenching in NPs limits the propagation of excitation energy compared to bulk materials, structural differences also have an impact on optical performance. Additionally, the light scattering at grain boundaries causes transparency issues for nanoceramics which are favored for applications like PET because they are less expensive and produced more quickly than single crystals. In order to reduce light absorption and increase scintillation efficiency, advanced techniques seek to produce optically homogenous nanoceramics [26,104].

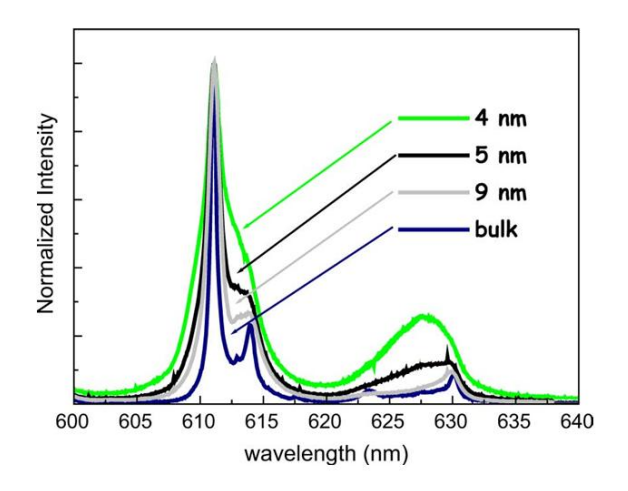


**Figure I.10** Eu<sup>3+</sup> doped  $Gd_2O_3$  fluorescence spectra at T=10K excitation at 580.7 nm (to  $4f^7$  7F<sup>0</sup>-  $^5D_0$ ). The fluorescence transition is equivalent to Eu<sup>3+</sup>'s  $4f^7$   $^5D_0$ -7F<sub>2</sub> [104].

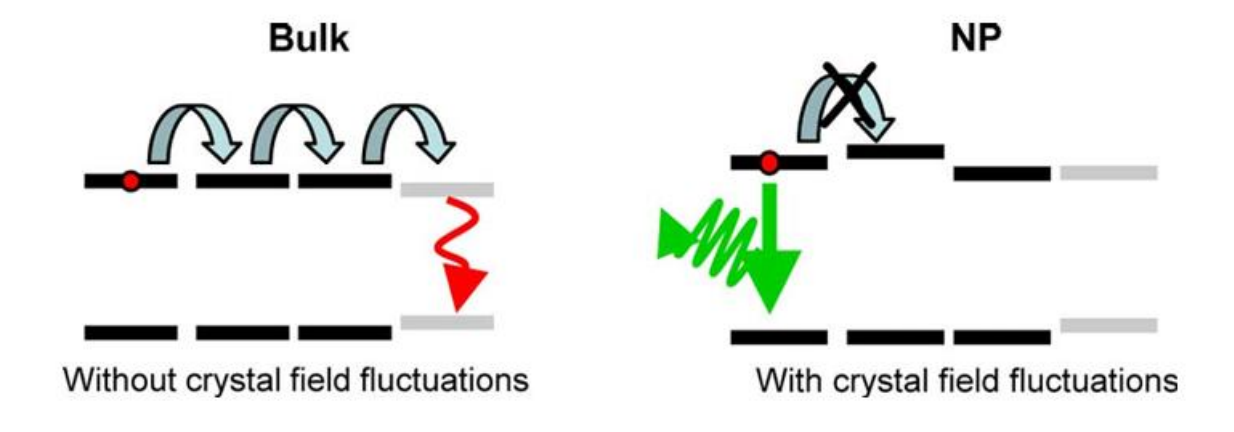


**Figure I.11** Effects of crystal field oscillations on concentration quenching: excitation energy can travel long distances in bulk materials (left) until it reaches a non-radiative defect (light grey) due to the alignment of energy levels (black lines) between dopant ions [104].

The development of nanomaterials has exploded, particularly in terms of novel synthesis methods and uses. Researchers are working to develop highly sensitive and reasonably priced materials to improve ionizing radiation detectors. As **Figure I.12** shows, these new uses illustrate the wider range of applications made possible by the characteristics of nanoparticles compared with their bulk counterparts. By combining knowledge from recent research with fundamental physics concepts, it is possible to estimate the effectiveness of treatments in a variety of circumstances [26]. This is why we have focused our efforts on using the low-cost sol-gel method to develop scintillating powders.

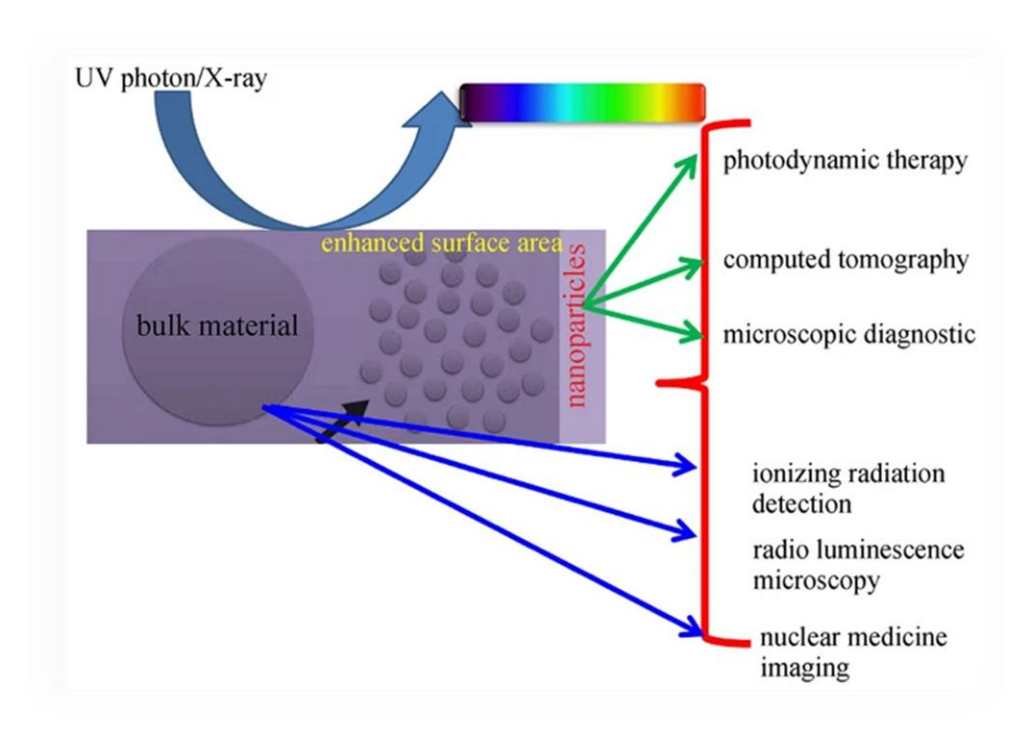


**Figure I.12** new uses illustrate the wider range of applications made possible by the characteristics of nanoparticles compared with their bulk counterparts.

#### Conclusion

In conclusion, this chapter has reviewed scintillating materials, their purpose and their numerous uses, Investigation of scintillation mechanisms and radiation-matter interactions has highlighted the importance of improving materials properties to develop high-performance radiation detectors. In particular, because of their impressive structural and optical characteristics, inorganic garnet-based scintillators especially LuAG have emerged as a key area of research and development. Enhancing their luminescence efficiency by adding Ce<sup>3+</sup> or Pr<sup>3+</sup> dopants, and co-doping with alkali metal ions (Li<sup>+</sup>, Na<sup>+</sup>, and K<sup>+</sup>) offers a feasible route to further improve performance.

## Chapter II

### **MATERIALS AND METHODS**

#### Introduction

The careful selection of materials, synthesis procedures and characterization techniques are essential to the result of any scientific research. In this chapter, the fundamental techniques used in the elaboration and study of  $Lu_3Al_5O_{12}$  garnet (LuAG) scintillators codoped with alkali metals ( $Li^+$ ,  $Na^+$  and  $Na^+$ ) and activated by rare earth ions ( $Ce^{3+}$  or  $Pr^{3+}$ ) are detailed, the powders were produced using sol-gel technique which is known for its accuracy in creating consistent, nano-sized materials of great purity.

In this chapter, the materials used in this study are described in detail with their composition, general information and selection criteria, together with a detailed description of the synthesis process, paying particular attention to the sol-gel procedure and optimization of the dopant concentration which is required to obtain the necessary structural, morphological and scintillation characteristics.

The structural properties and morphology of the particles are investigated using physical techniques such as X-ray diffraction (XRD), scanning electron microscopy (SEM) and energy-dispersive X-ray spectroscopy (EDS). While, their luminescent performance and trapping characteristics are evaluated using optical techniques such as photoluminescence (PL), radioluminescence (RL) and thermally stimulated luminescence (TSL). Finally, theoretical calculations and simulations based on density functional theory (DFT) are used to understand the electrical structure and defect states of codoped garnets and to support the experimental results.

#### **II.1 Materials**

#### **II.1.1 Starting Materials**

The necessary chemical precursors and starting materials to synthesise  $Lu_3Al_5O_{12}$  (LuAG) doped with rare earth ions ( $Ce^{3+}$  or  $Pr^{3+}$ ) and co-doped with alkali metal ions ( $Li^+$ ,  $K^+$  and  $Na^+$ ) are briefly summarized in the following table, the use of high purity precursor reagents to ensure homogeneity and consistency of the synthesized material which are necessary to obtain the best possible structural and optical properties, each precursor having a distinct function in the synthesis process:

Nº	Precursors	Nomination	Chemical purity (%)	Role
01	Lu <sub>2</sub> O <sub>3</sub> (acid Solvation)	Lutetium (III) oxide	99.999%	Lutecium source for Lu <sub>3</sub> Al <sub>5</sub> O <sub>12</sub> crystal structure
02	Al (NO <sub>3</sub> ) <sub>3</sub> , 9H <sub>2</sub> O	Aluminum nitrate nonahydrate	99.0%	Aluminum source
03	Ce (NO <sub>3</sub> ) <sub>3</sub> , 6H <sub>2</sub> O	Cerium nitrate hexahydrate	99.9%	dopant precursor for Ce <sup>3+</sup> ions (activator for PL/RL)
04	Pr(NO <sub>3</sub> ) <sub>3</sub> 6H <sub>2</sub> O	Praseodymium nitrate hexahydrate	99.9%	dopant precursor for Pr³+ ions (activator for PL/RL)
05	LiOH H₂O	lithium hydroxide monohydrate	Laboratory grade	co-dopant precursor for Li <sup>+</sup> ions
06	КОН	Potassium hydroxide	Laboratory grade	codopant precursors for K <sup>+</sup> ions
07	NaOH	Sodium hydroxide	Laboratory grade	codopant precursors for Na <sup>+</sup> ions
08	$\mathrm{HNO}_3$	Nitric Acid	65%	pH adjuster and complexing agent
09	CH₃COOH	Acetic acid	Analytical grade	Chelating agent and pH stabilizer
10	HOCH <sub>2</sub> CH <sub>2</sub> OH	ethylene glycol	Analytical grade	Polymerization agent and gel forming additive
11	(NH <sub>3</sub> ) H2O	Ammonia	34%	pH regulator
12	$C_2H_6O$ (EtOH)	Ethanol	Analytical grade	Cleaning agent
13	De-ionized water			Solvent

#### II.2 Synthesis Methodology

#### II.2.1 Sol-Gel Synthesis Process

Sol-gel methods have become a flexible and economical method for creating sophisticated materials such as glasses, ceramics, powders, fibers, and thin films throughout the last thirty years [31]. By using molecular precursors such metal alkoxides or acetates, this solution-based technique allows for exact control over the distribution of particle sizes, shape, and material composition. One major benefit is its capacity to generate homogeneous, highly pure nanomaterials, which is especially important for luminescent applications where emission characteristics rely on dopants like rare-earth or transition metal ions (e.g.,  $Ce^{3+}$ ,  $Eu^{3+}$ ) [32]. Furthermore, compared to traditional solid-state synthesis, sol-gel technique has several advantages, such as increased precursor reactivity, better compositional homogeneity, lower sintering temperatures, and scalability [1,3]. Recent developments show that sol-gel chemistry can be applied to elaborate oxide systems. This method has been successfully used to create cerium-doped lutetium aluminum garnet ( $Lu_3Al_5O_{12}$ :Ce), a potential scintillator material, by taking advantage of its capacity to achieve controlled crystallization and homogeneous dopant distribution at lower processing temperatures [3].

In this work, Lu<sub>3</sub>Al<sub>5</sub>O<sub>12</sub> (LuAG) powders doped with Ce<sup>3+</sup> and Pr<sup>3+</sup> ions and co-doped with different concentrations of alkaline metal ions (Li<sup>+</sup>, Na<sup>+</sup>, and K<sup>+</sup>) were synthesized using the sol-gel method at laboratory of the **Algiers Nuclear Research Centre (CRNA)**. The synthesis process steps are presented in **figure II.1** and explained in details in the next section (**3.2 Optimization of Co-Doping Concentrations**), starting by preparation of precursors mentioned in previous section (**2.1 Starting Materials**).

By precisely controlling the dopant and co-dopant concentrations, the sol-gel process guaranteed the produced powders' repeatability. This method works especially well for creating phosphor and scintillator materials, where improving optical qualities requires uniformity and purity.







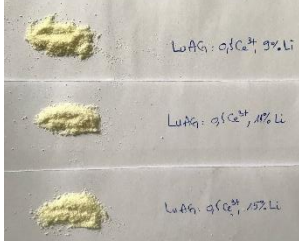
**Precursors** + **solvent** 

**Sol-solution** 

Thermal drying



Xerogel

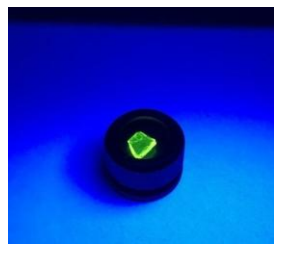






**Powders** 









LuAG:1at. %Pr3+, x at. %Li+

SC LuAG:Ce3+

LuAG:0.5at.% Ce, x at. % Na<sup>+</sup>

LuAG:Ce,Li

**Figure II.1** Synthesis process steps and final products of some codoped LuAG:Ce and LuAG:Pr by different content of Li, Na and K powders prepared - **CRNA Algiers.** 

#### II.2.2 Optimization of Co-Doping Concentrations

A series of  $Lu_3Al_5O_{12}$  (LuAG) garnet powders activated by  $Ce^{3+}$  or  $Pr^{3+}$  and co-doped with alkaline metal ions such as ( $Li^+$ ,  $Na^+$  and  $K^+$ ) were prepared using sol gel method, as listed in **2.1 Starting Materials** the precursors used include  $Lu_2O_3$  (99.99%),  $Al(NO_3)_3$  9 $H_2O$  (99.0%),  $Ce(NO_3)_3$  6 $H_2O$  (99.9%),  $Pr(NO_3)_3$  6 $H_2O$ , lithium hydroxide monohydrate LiOH  $H_2O$ , Potassium hydroxide KOH, Sodium hydroxide NaOH, nitric acid ( $HNO_3$ ), acetic acid ( $CH_3COOH$ ), ethylene glycol ( $HOCH_2CH_2OH$ ) and ammonia ( $NH_3$ ) of analytical grade were used as starting materials. During the synthesis the experiments parameters were kept constant, the concentration of alkaline metal ions is the only variable.

To optimize cooping concentrations, non-co-doped and x at. % Li\* (x = 0, 1, 3, 5, 7, 9, 11 and 15) co-doped 0.5 at%  $Ce^{3+}$ -Lu<sub>3</sub>Al<sub>5</sub>O<sub>12</sub> garnet powders were prepared by sol-gel method. Lu<sub>2</sub>O<sub>3</sub> (99.999%), Al(NO<sub>3</sub>)<sub>3</sub>, 9H<sub>2</sub>O (99.0%), Ce (NO<sub>3</sub>)<sub>3</sub>, 6H<sub>2</sub>O (99.9%), LiOH H<sub>2</sub>O lithium hydroxide monohydrate, nitric acid (HNO3), acetic acid (CH<sub>3</sub>COOH), ethylene glycol (HOCH<sub>2</sub>CH<sub>2</sub>OH) and ammonia (NH<sub>3</sub>) of analytical grade were used as starting materials. To form LuAG powder, stoichiometric Lu<sub>2</sub>O<sub>3</sub> and Al(NO<sub>3</sub>)<sub>3</sub>, 6H<sub>2</sub>O (Lu/Al = 3/5 in mole ratio) were used. During the synthesis, all the experimental parameters were fixed, only the codoping contents of Li\* (K\* or Na\*) contents (at. %) was varied. The procedure used in this study for synthesis of cerium-doped lutetium aluminum garnet (Lu<sub>3</sub>Al<sub>3</sub>O<sub>12</sub> or LuAG) with composition (Lu<sub>0.995-x</sub>Li<sub>x</sub>)<sub>3</sub> Ce<sub>0.015</sub>Al<sub>5</sub>O<sub>12</sub>: Li<sub>x</sub> (x = 0.01, 0.03, 0.05, 0.07, 0.09, 0.11, 0.15) is shown in a flow diagram **Figure II.2.** 

To begin, 25 ml of de-ionized water was mixed with 28 ml of nitric acid (HNO<sub>3</sub>). In this first step, stoichiometric  $Lu_2O_3$  was then dissolved in the resulting mixture. The mixed solution was stirred at  $150^{\circ}$ C for 40 minutes, resulting in a clear and homogeneous solution. In the second step, stoichiometric aluminum nitrate was dissolved in the resulting solution at a molar ratio of Lu: Al = 3:5. Then, the corresponding stoichiometric amount of cerium nitrate was added to the solution. Acetic acid (AA) was introduced to the solution with a molar ratio of  $CA:M^{3+} = 1$  ( $M^{3+}: Lu^{3+} + Al^{3+} + Ce^{3+} + Li^{+}$ ). Subsequently, ethylene glycol (EG) was added to the solution at a molar ratio of EG:CA = 2:1. The solution was continuously stirred for several hours. The solutions were modified to achieve a pH value of 1 by incorporating ammonia solution (NH<sub>3</sub>). Afterward, the solution was subjected to drying at 120 °C until foam formation occurred. Subsequently, the foam was annealed in a programmable muffle furnace, exposed to air, at a temperature of 1100 °C for a duration of 2 hours. The doping concentration of  $Ce^{3+}$  was consistently

maintained at 0.5 at. % (Chapter III Codoping Effects of Li<sup>+</sup>, K<sup>+</sup>, and Na<sup>+</sup> on LuAG:0.5%Ce<sup>3+</sup> Scintillating Powders). And the doping concentration of Pr<sup>3+</sup> was consistently maintained at 1 at. % (Chapter IV Codoping Effects of Li<sup>+</sup>, K<sup>+</sup>, and Na<sup>+</sup> on LuAG:1%Pr<sup>3+</sup> Scintillating Powders), ensuring a high emission intensity.

To study the effect of co-doping by Li<sup>+</sup> , K+ and Na+ ions on Lu<sub>3</sub>Al<sub>5</sub>O<sub>12</sub>:Ce<sup>3+</sup> and Lu<sub>3</sub>Al<sub>5</sub>O<sub>12</sub>:Pr<sup>3+</sup> properties, the same steps were followed [1]. Furthermore, for comparison, a 0.1 at. % Ce<sup>3+</sup> doped LuAG single crystal was grown by Czochralski (Cz) following the conditions published in ref [106].

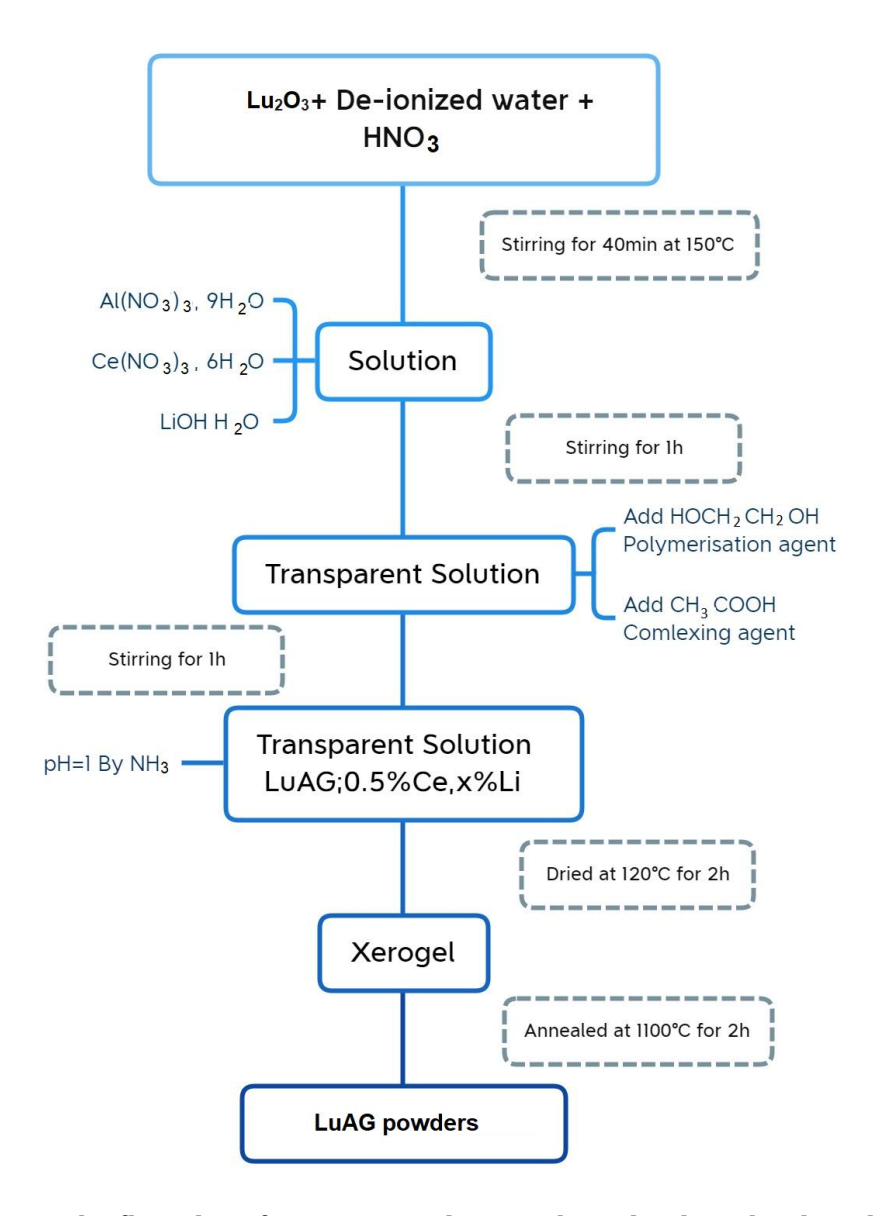


**Figure II.2** The flow chart for LuAG powders synthesis by the sol-gel method [1].

#### II.3. Characterization Techniques

#### **II.3.1 Physical Characterization**

#### II.3.1.1 X-ray Diffraction (XRD)

X-ray diffraction (XRD) is an essential tool for characterizing different types of materials. It is a very powerful and non-destructive technique used to investigate the crystalline structure of materials, such that understanding the structure is therefore crucial for adapting growth conditions and designing functional properties. XRD provides essential information on the phase composition, crystallite size, lattice parameters and degree of crystallinity of synthesized powder materials.

A scheme of the X-ray diffraction physical process may be found in **Figure II.3**, where a sequence of atomic planes spaced d apart are impacted by an X-ray beam with a wavelength  $\lambda$ . The angle of incidence with respect to the atomic planes is  $\underline{\theta}$ , which is the angle at which the X-ray beam scatters on the planes. The following equation describes the relationship between the X-rays scattered by the first and second planes. The distance in Figure 1 that is indicated in orange indicates the optical path difference between related to two rays scattered by the first and second planes. Therefore, it is easy to demonstrate from geometrical considerations that constructive interference will happen at specific angles,  $\underline{\theta}_B$ , as a function of the two planes' distance from one another.

$$n\lambda = 2d_{hkl}\sin\theta_B \tag{1}$$

The well-known Bragg Equation 1 is represented by the subscript hkl of the crystallographic plane, where d is the interplanar spacing related to the Miller indices and  $\underline{\theta}_B$  is the Bragg angle. First-order diffraction is represented by n=1, second-order diffraction by n=2, and so on. The variable n is an integer known as the diffraction order. All XRD measurements are based on the Bragg Equation, which determines the link between the lattice spacing and the angular position of the diffracted X-rays [107].

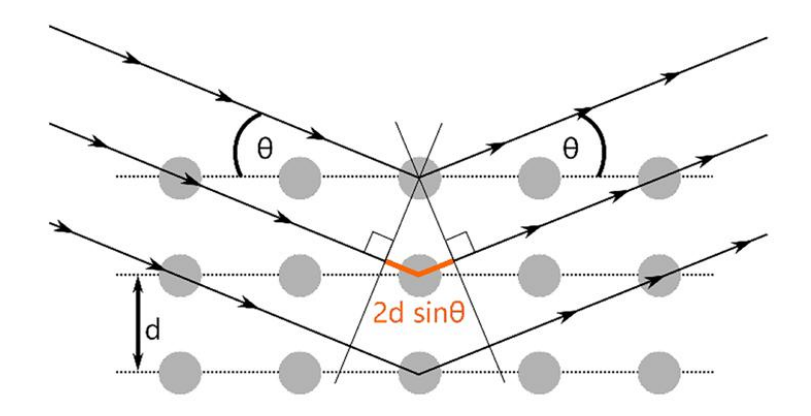


**Figure II.3** Visualisation of the Braggs equation. [107]

In our study, The XRD analyses were performed at the **Algiers Nuclear Research Centre (CRNA)** shown in **figure II.4**, where it was used to both confirm the successful formation of the garnet phase  $(Lu_3Al_5O_{12})$  and to assess the effect of codopants by different content of different alkaline metals  $(Li^+, K^+, Na^+)$  on structure properties of synthetized materials.

The phase identification and the related properties of the produced powders were investigated by X-ray diffraction (XRD) technique a PANanlytical X'Pert (Philips) PRO system with Cu K $\alpha$  radiation (k = 1.54059 Å) operated at 45 kV and 40 mA. Symmetric (h-h) scans were performed from 10 to 902 h with a step width of 0.02. All the data were processed by X'Pert High Score plus Software with commercial databases (FWHM deduction and peak identification) [1].



Figure II. 4 X-ray diffraction (XRD) technique a PANanlytical X'Pert (Philips) PRO -CRNA Algiers.

#### II.3.1.2 Morphological Analysis

Using scanning electron microscopy (SEM), the morphological properties of the synthesized powders, co-doped with varying concentrations of Li<sup>+</sup>, Na<sup>+</sup>, and K<sup>+</sup>, were investigated. Detailed information on the size, shape and surface texture of the particles was obtained using this technique. Moreover, energy dispersive X-ray spectroscopy (EDS) was used to complement the SEM analysis, providing compositional and elemental data. Overall, the above techniques provided a complete understanding of the material microstructure and chemical composition of the prepared samples.

In our study, Morphological images and EDX measurements of the prepared samples were carried out using a JEOL JSM-5400 scanning electron microscope at **Tunisian Petroleum Activities Company (ETAP)** shown in **figure II.5.** 

#### II.3.1.2.1 Scanning Electron Microscopy (SEM)

The scanning electron microscope (SEM) offers one of the most versatile tools available for both investigating and analyzing the morphology of the material's microstructure and characterizing its chemical composition. Details on the SEM method and how it works is available in reference [108].

#### II.3.1.2.2 Energy Dispersive X-ray Spectroscopy (EDS)

Energy dispersive X-ray spectrometry (EDS) is a measurement technique that determines the intensity of X-ray emission as a function of X-ray photon energy (Fitzgerald et al., 1968; Goldstein et al., 2003). Details on EDS technique is available in reference [109].





Figure II.5 JEOL JSM-5400 Thermoscientific Scanning Electron Microscope- ETAP Tunisia

#### II.3.2 Optical Characterization

#### II.3.2.1 Photoluminescence Spectroscopy (PL)

Photoluminescence (PL) spectroscopy is a powerful, non-destructive optical characterization technique used to study the electronic and optical properties of materials. Details on PL setup and specific experimental parameters are available in reference [110].

In this study, the photoluminescence steady state and time resolved measurement to analyse the optical properties of the synthetized powders were conducted at the **Algiers Nuclear Research Center (CRNA)** (**figure II.6**) and at **Materials science department, Università degli Studi di Milano-Bicocca** (**figure II.7** and **II.8**). It provided valuable insights into the effect of codoping on luminescence properties of codoped LuAG:Ce<sup>3+</sup> and LuAG:Pr<sup>3+</sup> by different content of Li<sup>+</sup>, K<sup>+</sup>, and Na<sup>+</sup> scintillating powders.

The room temperature emission and excitation photoluminescence spectra were carried out using Perkin-Elmer (LS-50B) luminescence spectrometer utilizing a Xe lamp as the excitation source. PL time decay measurements were carried out with a FLS980 Spectrometer (Edinburgh Instruments) featuring a pulsed light emitting diode (EPLED-340) with 920 ps pulse width as the excitation source. The detector was a Hamamatsu R928P photomultiplier tube working in time-correlated single photon counting (TCSPC) mode [1].

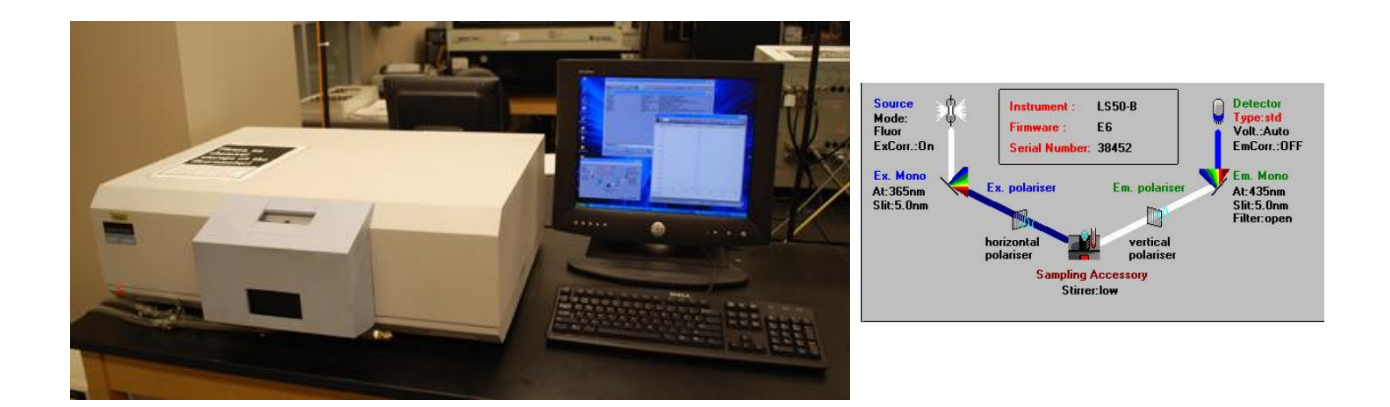


Figure II.6 Perkin-Elmer (LS-50B) luminescence spectrometer -CRNA Algiers.

#### II.3.2.2 Radioluminescence (RL)

In this study, the Radioluminescence measurement, both steady state and time resolved, were conducted at the **Materials Science Department**, **Università degli Studi di Milano-Bicocca**. Steady state RL was performed by using a homemade apparatus featuring a CCD (Jobin-Yvon Symphony II) coupled to a monochromator (Jobin-Yvon Triax 180) operating in the 200-1100 nm range as detection system with slits of 0.1 mm (7 nm bandpass), grating density 100 grooves/mm and 0.5 s integration time (**Figure II.7**). RL excitation was obtained by X irradiation through a Be window, using a Philips 2274 X-ray tube with tungsten target operated at 20 kV, 20 mA.





**Figure II.7** Homemade instrumental setup for radio- thermo- and photo-luminescence-**Unimib Italy**.



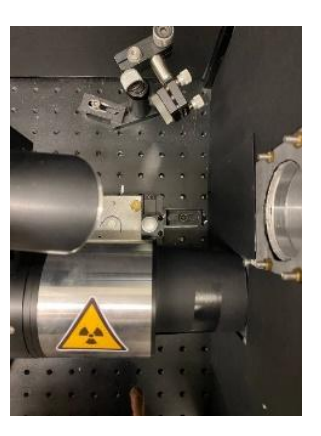


Figure II.8 Instrumental setup for PL and scintillation decay-Unimib Italy.

#### II.3.2.3 Thermally Stimulated Luminescence (TSL)

An important method for examining trapping states and how they affect a material's luminescence characteristics is Thermally Stimulated Luminescence (TSL). TSL is very helpful for figuring out the energy levels of traps inside a material and the thermal stability of trapped charge carriers. It entails heating a sample gradually after it has been exposed to radiation, these releases trapped charge carriers which then recombine at luminescent centers to produce a detectable light emission [111].

In our work, TLS measurements on the synthesized powders were performed at the Materials Science Department, Università degli Studi di Milano-Bicocca using the apparatuses shown in figure 9. It provides an insight into the trapping depth distribution, charge carriers and defect states dynamics in the materials that could influence prompt radiative recombination, TSL measurements was carried out both above room temperature (300 K - 650 K) and at low temperatures (10 K to 320 K) (figure II.9).



**Figure II.9** wavelength-resolved thermally stimulated luminescence below and above room temperature, X-ray spectroscopy apparatuses – **Unimib Italy**.

#### II.3.3 Theoretical Calculations and Simulations

Materials can be analyzed under extreme conditions such as high temperatures and pressures, using advanced laboratory techniques. However, it is still a challenge to characterize luminescent materials because of their sensitivity and the precision required to manipulate them, in these case, theoretical approaches, in particular electronic structure calculations, are a useful complement to experimental studies and provide a better understanding of the observed phenomena.

#### II.3.3.1 Density Functional Theory (DFT) Simulations via VASP

Density functional theory (DFT) is one of the most practical tools for investigating the physico-chemical characteristics of materials, it is a basic ab initio method that has its origins in quantum mechanics. Depending on the size of the system, DFT provides a quantitative model for simulating the behavior of materials and for allowing experimental and theoretical results to be compared. The VASP (Vienna Ab-initio Simulation Package), designed by Kresse and Furthmuller [112], is essentially based on the Mermin formulation [113] and employs a series of exchange-correlation functions, such as those of Perdew [114], Hedin and Lundquist [115], and Ceperley and Alder [116], together with Kresse and Furthmuller. We used this package to perform the DFT calculations in our work. VASP is based on a plane wave and pseudopotential formalism. In our simulations, the projector augments wave (PAW) method was chosen because of its high precision [117-119], contrary to ultra-soft pseudopotentials, the PAW method takes into account the exact valence wave functions including the central region nodes which ensures accurate results. This method was at the basis of the calculations carried out as part of this study.

A condensed diagram of the VASP software is displayed in **Figure II.10**. This program uses an iterative matrix cross-section method to solve the Kohn-Sham equations. Davidson's technique [120,121] serves as the foundation for the solution algorithm. The system employs the effective Broyden-Pulay approach to mix the charge density during self-consistent iterations [122-124]. By taking into account the derivatives of the free energy with respect to the atomic locations, the Hellmann-Feynman theorem [125] is used to determine the forces acting on the ions. Whether a quasi-Newton method or a conjugate gradient method is used to optimize the geometry [126].

VASP uses 4 files (**figure II.10**) which are detailed in **table II.1**:

**POSCAR**: this file contains information about the geometry of the cell and the position of the ions.

**INCAR**: this is the central file of the input files, because it is from this file that it is possible to determine the nature of what is being done and the method used. It contains the parameters specifying the electronic state of the system, the functional used (in our case GGA) and the algorithm used for geometric optimization, as well as the maximum number of optimization cycles.

**POTCAR**: this file contains the pseudo potential of each atom used in the calculation. It also contains information about each atom (e.g. mass, valence, reference energy and cut-off energy).

**KPOINTS**: this file contains the k-points chosen to describe the system under study. This choice must be adapted to the shape of the cell.

The output files are:

**OUTCAR**: this is the file which gives the total energy of the system using the four input files and it also includes the calculation steps.

**CONTCAR**: this file is similar to POSCAR, but contains the position of the ions after relaxation (this is given in INCAR).

**CHGCAR**: this file is used to calculate the magnetic charge density.

**PROCAR**: for each band, the atomic and orbital location of the electrons can be found. Note that the wave function is calculated by projecting the wave functions onto harmonic spheres which are characterized by an RWIGS radius which must be specified in the INCAR file (if the RWIGS is not specified, the PROCAR file is not obtained).

**EIGENVAL**: this file contains the Kohn-Sham eigenvalues, i.e. the energy level of the different bands, for each k-point value.

**OSZICAR**: this file gives information about the speed of convergence of the calculation.

**DOSCAR**: this file contains the densities of state for the entire system and then for each atom.

**WAVECAR**: this file gives the plane waves that have been calculated.

LOCPOT: contains the potential of an electron in each parallelepiped of the grid.

**IBZKPT**: gives details of the k-points used in the calculation.

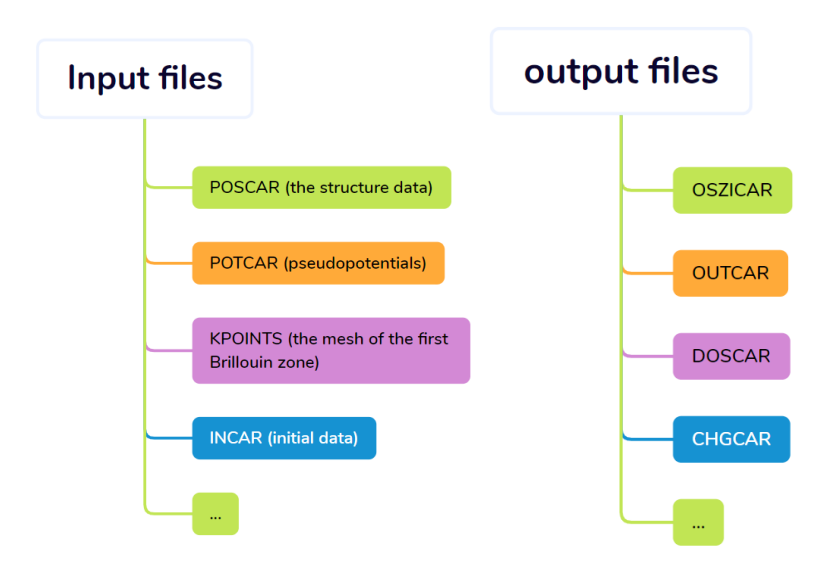
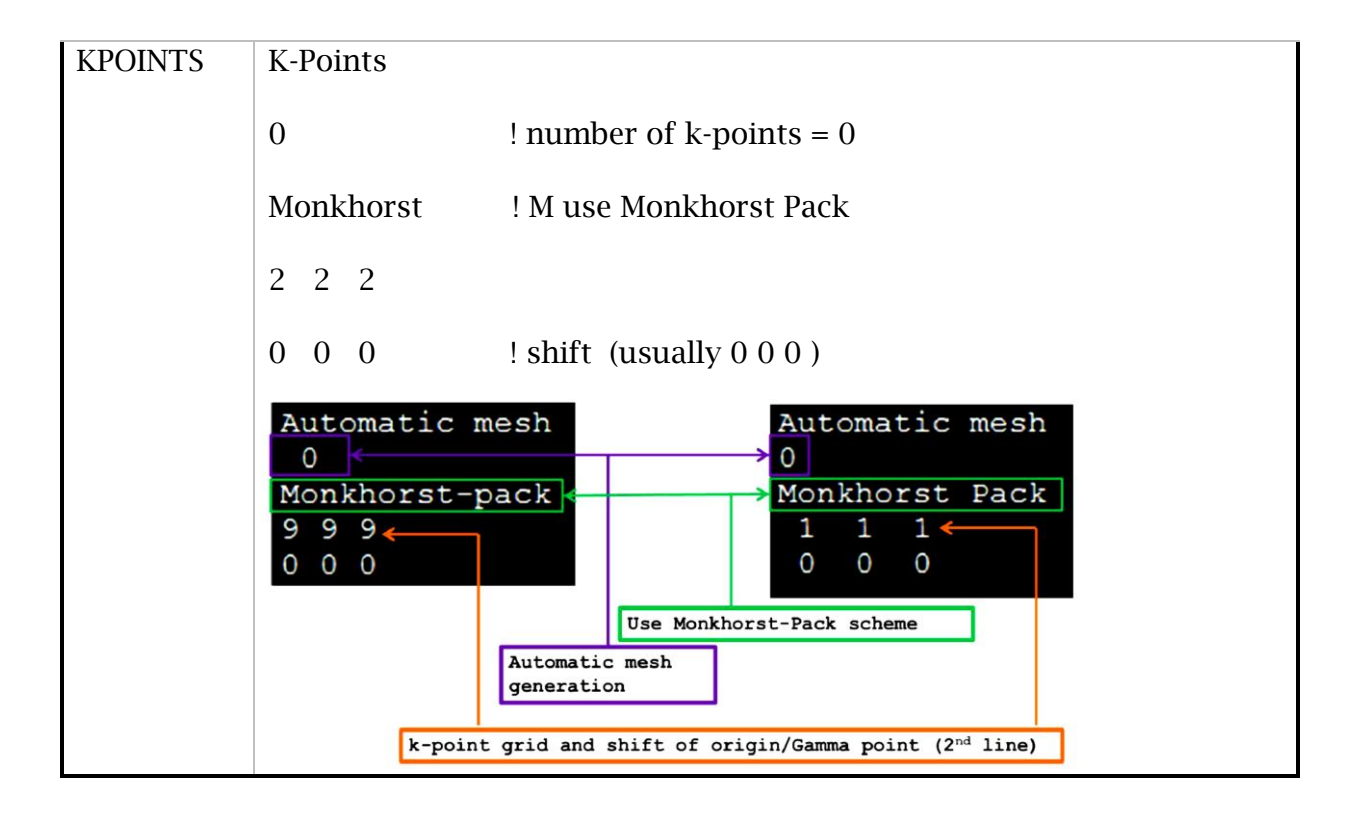


Figure II.10. VASP input and output files.

**Table II.1** The different files used in the calculations.

POTCAR	Packages available for psuedepotentials and electronic configuration			
	in the pseudopotential's directory (paw, pawGGA, pawPBE)			
	PAW_PBE 0 08Apr2002			
	Pseudo PAW potential of oxygen  LEXCH - PE  EATOM = 432.3788 W 31.789 Ry			
	Number of valence electrons			
	IUNSCR = 0 unscreen: lin 1-nElectronic configuration of valence  RPACOR = .000 partial core radius  POMASS = 16.000; ZVAL = 6.000 mass and val			
	RCORE - 1.520 outmost cutoff radius RWIGS - 1.550; RWIGS820 wiscer-self ENMAX - 400.000; ENMIN - 300.000 eV Functional used to construct the ICORE - 2 local potential			
	LCOR - T correct aug charges pseudopotential  LPAW - 605.392 Minimum cutoff recommended for this atom			
	DEXC = .000 Finding Cutoff recommended for this atom  RMAX = 2.264 core radius for proj-oper  RAUG = 1.300 factor for augmentation sphere  RDEP = 1.550 radius for radial grids  QCUT = -5.520; QGAM = 11.041 optimization parameters			
POGGA P	CLICETTA VIOLO			
POSCAR	SYSTEM: Y2O3			
	1.000000 10.69999			
	0.000000 10.69999 0.000000			
	0.000000 0.000000 10.69999			
	48 32			
	Direct			
	0.390350 0.151450 0.380370			
	0.890350 0.651450 0.880370			
	0.109650 0.848550 0.880370			
	0.609650 0.348550 0.380370			
	0.609650 0.651450 0.119630			



#### II.3.3.2 Defect State Calculations

In our research, all calculations are based on DFT [127,128] implemented in the Vienna ab initio simulation package (VASP) code [129]. The interaction between ions and electrons is described by the projector augmented-wave method. The total energy is calculated using the Perdew-Burke-Eznerhof (PBE) exchange-correlation functional, and the electronic structure performed using GGA-PBE pseudopotential. The Brillouin zone was sampled with a mesh of  $4\times4\times4$  for relaxation and self-consistent field (SCF) calculation. For the total and partial density of states, we used a k-point mesh  $8\times8\times8$ , centered at the Gamma point, the total energy convergence criterion was set to 10-6 eV, the maximum component of force acting on any atom in the relaxed geometry was less than 0.01 eV/A, the maximum stress below 0.05 GPa, and a maximum displacement between cycles of below 0.003 Å. [1]. The result is presented in **chapter III**.

#### Conclusion

The materials, synthesis process and characterisation methods used in our study were all thoroughly covered in this chapter. Codoped LuAG:Ce and LuAG:Pr by different content of Li<sup>+</sup>, K<sup>+</sup>, and Na<sup>+</sup>, scintillating powders were successfully synthetized using solgel process which is adaptable and cost-effective method with exact control over codoping concentrations.

X-ray diffraction (XRD) and Scanning electron microscopy (SEM) were used for providing information on the morphological characteristics and crystalline structure, energy-dispersive X-ray spectroscopy (EDS) was used to complementary verified the elemental composition. A detailed understanding of optical properties such as the luminescent behavior, defect states, and scintillation characteristics of the produced powders was made possible by optical and scintillation characterisation techniques like photoluminescence (PL), radioluminescence (RL), and thermally stimulated luminescence (TSL). In addition, the theoretical simulations based on Density Functional Theory (DFT) performed using VASP software have further supported our experimental findings through an improved understanding of the crystalline structure, the defect states and their effects on the material's properties.

Results and discussions derived from the methods and techniques reported in this chapter will be detailed in Chapter 3, focusing on LuAG:0.5 at. %Ce³+ co-doped with different Li⁺, K⁺ and Na⁺ contents, and in Chapter 4, focusing on LuAG:1 at. %Pr³+ codoped with the same alkali metal ions. Such information will be crucial for optimising scintillation efficiency and progressing the development of LuAG-based materials for advanced optical applications.

# Chapter III

CODOPING EFFECTS ON LuAG:Ce3+

#### Introduction

This chapter investigates in detail the structural, morphological and optical properties of sol-gel synthesized aluminum lutetium garnet (LuAG) doped with 0.5% Ce<sup>3+</sup> and co-doped with alkali ions (Li<sup>+</sup>, K<sup>+</sup>, Na<sup>+</sup>). The study aims to understand the effect of codoping by monovalent alkali ions on the structure, morphological, luminescent and scintillation properties of LuAG:Ce<sup>3+</sup> powder material to optimize its performance as a scintillating material, by including both experimental characterizations and density functional theory (DFT) simulations.

The chapter starts with a structural analysis, using X-ray diffraction (XRD) to study the changes in both crystal lattice and phase purity due to alkali codoping. The analysis is supported by VASP simulations that provide theoretical insight into defect formation, charge compensation processes and atomic level structures in the codoped material.

Morphological analysis involves scanning electron microscopy (SEM) to study grain size, shape and surface characteristics while Energy Dispersive X-ray Spectroscopy (EDS) is used to confirm the material's elemental composition and dopant composition. This analysis allows a relationship to be built up between the synthesis process, the addition of doping materials and the resulting microstructure. The optical properties of codoped samples are investigated by photoluminescence and radioluminescence studies. Steady-state photoluminescence measurements are performed to evaluate emission spectra and intensity under light excitation, while time-resolved photoluminescence studies the lifetime of excited states and the energy transfer dynamics. In the same way, steady-state and time-resolved radioluminescence measurements evaluate the material's response to ionizing radiation and provide essential insights into its scintillation performance.

Additionally, Thermally Stimulated Luminescence (TSL) is used to analyse trap states in the materials bandgap providing essential information about its scintillation performance. High temperature TSL measurements reveal deep traps acting as competitors of the luminescence centers in capturing the free ionized charges while low temperature TSL studies identifies shallow traps that could affect the processes of scintillation by causing a delayed recombination and afterglow. These measurements allow a better understanding of the way alkaline codoping affects the material's ability to accumulate and release energy which is critical to enhance scintillation efficiency.

Linking experimental data with computational models, the aim of this chapter is to provide a comprehensive understanding of the way in which codoping by alkali ions affects LuAG:Ce<sup>3+</sup> at several scales from atomic level defects to the macroscopic optical behavior. This understanding is helping to advance the development of materials for scintillation with enhanced efficiency and sensitivity.

## III.1 Codoping effects of Li<sup>+</sup>, K<sup>+</sup>, and Na<sup>+</sup> on LuAG:0.5%Ce<sup>3+</sup> scintillating powders

#### III.1.1 Structural analysis

**Figure III.1** shows the XRD patterns of Lu<sub>3</sub>Al<sub>5</sub>O<sub>12</sub>: 0.5 at. % Ce<sup>3+</sup> co-doped by different content of Li<sup>+</sup> alkali metal cation Lu<sub>3</sub>Al<sub>5</sub>O<sub>12</sub> 0.5 at. % Ce<sup>3+</sup>, x at. % Li<sup>+</sup> (x = 1, 3, 5, 7, 9, 11 and 15 at. %) samples. It is obvious that all the diffraction peaks of the samples can be well indexed to the cubic phase (JCPDS no. 73–1368), with *Ia3d* as the space symmetry group. Also, one can see that all samples present LuAlO<sub>3</sub> (LuAP) as an impurity phase (peak at 34.563°), except for the sample with 5 at % Li<sup>+</sup>, which exhibits a pure LuAG phase. In the LuAG structure (**Figure III.2**), Lu<sup>3+</sup> is located in a distorted centered cubic geometry surrounded by eight equivalent  $O^{2-}$  atoms in a site close to  $D_2$  symmetry [130]. The  $Al^{3+}$ ion occupies two inequivalent sites. At the first site Al3+ is linked to six equivalent O2atoms (16a) to form corner-sharing AlO<sub>6</sub> octahedra (O<sub>h</sub>) and at the second site, Al<sup>3+</sup> is bonded to four equivalent  $O^{2-}$  atoms (24d) forming corner-sharing AlO<sub>4</sub> tetrahedra ( $T_d$ ). The O<sup>2-</sup> atom is linked in a 4-coordinate geometry to two equivalent Lu<sup>3+</sup> and two Al<sup>3+</sup> atoms [130]. Roughly, one can say that co-doping with Li<sup>+</sup> ions does not induce significant changes in the host structure. **Table III.1** shows the structural parameters for samples of LuAG: 0.5%Ce<sup>3+</sup> co-doped with different content of Li<sup>+</sup>. In addition, all powder samples present the same preferential orientation peak (420) compared to JCPDS no. 73-1368. Also, the sample with 5 at % Li<sup>+</sup> exhibits the highest intensity for all main diffraction peaks compared to other samples, where the intensity remains unaffected by the Li<sup>+</sup> content as shown in Figure III.3a. Furthermore, one can observe that the intensity ratio between (321) and (400) diffraction peaks decrease for 1, 3 and 7 at. % Li<sup>+</sup> compared to that of JCPDS no. 73-1368 and the other samples, thus promoting the growth of crystallites following the orientation (400). In addition, it is important to note also the change in the peak positions as presented in **Figure III.3b.** 

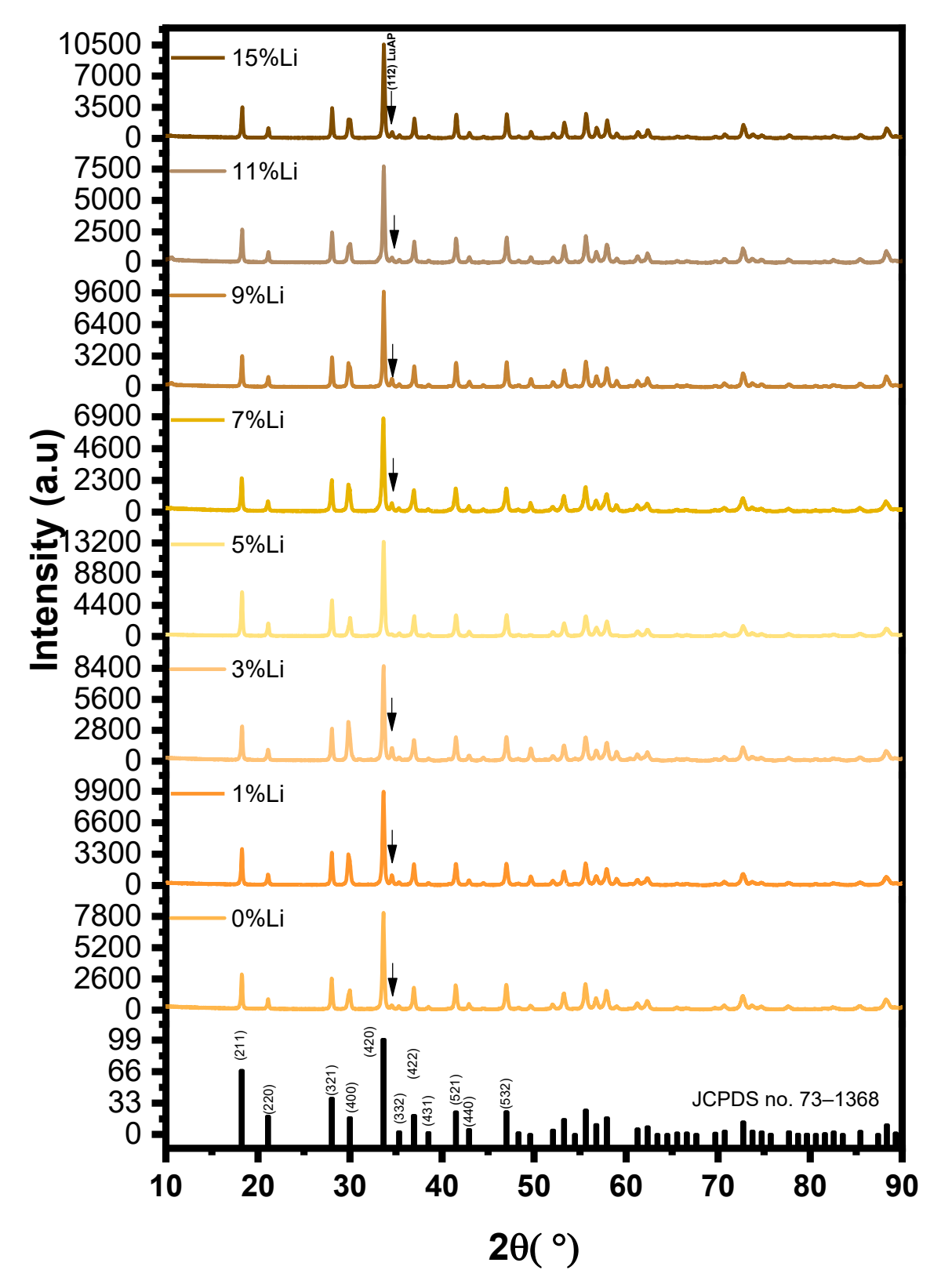


**Figure III.1** XRD patterns of  $Lu_3Al_5O_{12}$ : 0.5 at. % Ce<sup>+3</sup>, co-doped with different  $Li^+$  co-doping concentration [1].

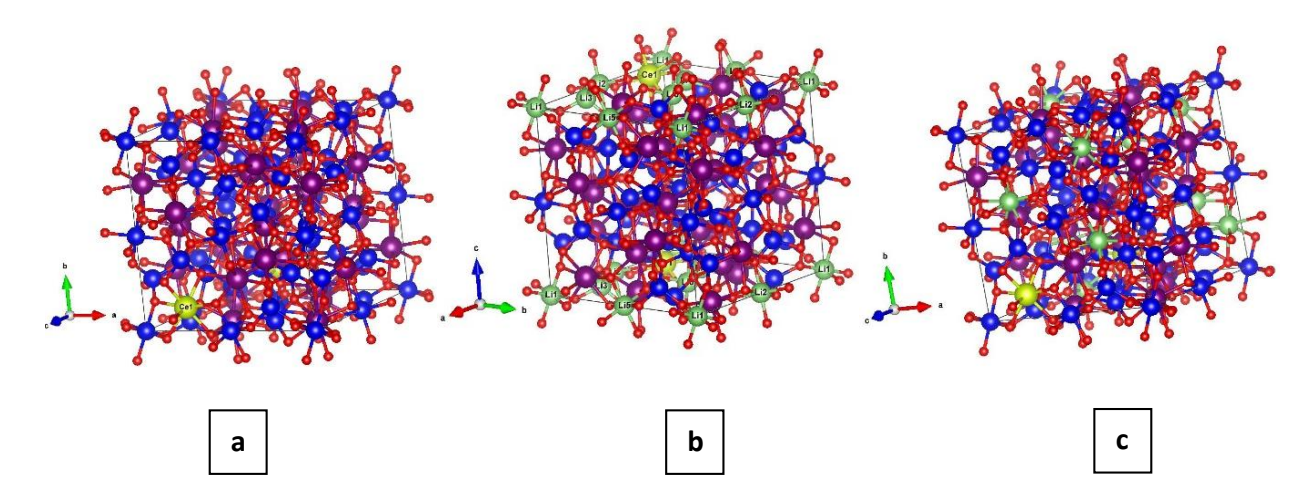


**Figure III.2** Structure configurations containing, (a) LuAG doped Ce, (b) LuAG:Ce co-doped Li<sub>Al</sub> substitute defect, and (c) LuAG:Ce co-doped Li<sub>Lu</sub> substitute defect. Green, red, blue, purple and yellow spheres represent Li, O, Al, Lu and Ce atoms, respectively [1].

a = 11.9060 Å (1368-073-01)

#### Crystallite size D and strain ε

Scherrer-approach

$$D_{sch} = \frac{0.9 \times \lambda}{\beta_{sample} \cos \theta}$$

Where  $D_{\text{Sch}}$  is the crystallites size in nm,  $\lambda$  the wavelength of Cu K $\alpha$  radiation in nm,

 $\beta_{\text{sample}} = \sqrt{\beta_{exp}^2 + \beta_{int}^2}$ ,  $\beta_{\text{exp}}$  is the full width at half maximum in the (420) reflection,  $\beta_{\text{int}}$  is the correction factor for instrument broadening and h the diffraction angle.

Williamson-Hall approach

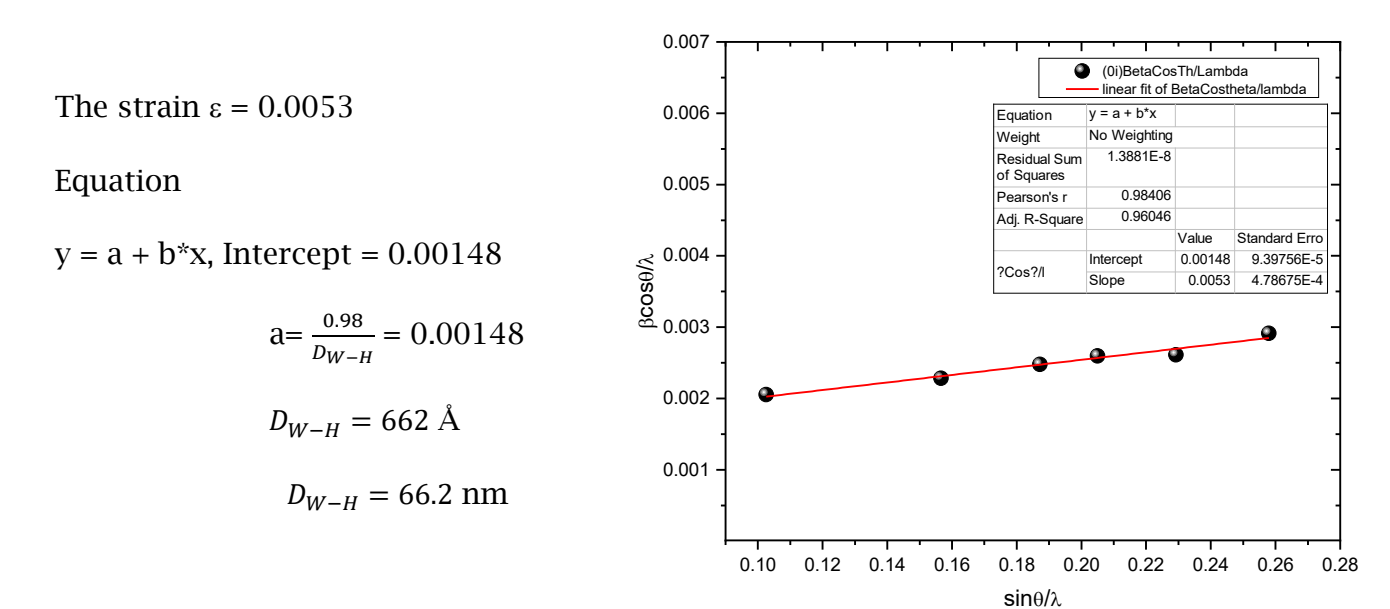
$$\frac{\beta \cos \theta}{\lambda} = \frac{k}{D_{W-H}} + \frac{\varepsilon \sin \theta}{\lambda}$$

 $(\lambda = 1,54439 \text{ Å}, \text{ Shape factor } k = 0.98)$ 

The strain  $\epsilon$  is calculated from the slope of the plot of  $\beta \cos\theta/\lambda$  gainst  $\sin\theta/\lambda$  and the effective crystallite size  $(D_{\text{\tiny W-H}})$  is calculated from the intercept to  $\beta \cos\theta/\lambda$ , respectively.

#### Pure LuAG:Ce

(hkl)	2 θ (°)	FWHM	$\theta$ (rad)	FWHM (rad)	$\frac{\sin \theta}{\lambda}$	$\frac{\beta\cos\theta}{\lambda}$	Height
		(°)		(rad)			[cts]
211	18.2368	0.184	0.1591461	0.0032114	0.102613432	0.00205312	1924
321	28.0007	0.208	0.2443522	0.0036302	0.156649436	0.0022808	1791
420	33.6112	0.229	0.29331305	0.0039968	0.187210072	0.00247742	5624
422	36.9153	0.242	0.32214676	0.0042237	0.205002376	0.00259418	1272
521	41.471	0.247	0.36190275	0.0043109	0.229251918	0.00261056	1492
532	46.9621	0.281	0.40982163	0.0049043	0.257995544	0.00291264	1507



Same steps were followed for the other Li<sup>+</sup> content

**Table III.1** Structural parameters for samples of LuAG: 0.5% Ce<sup>3+</sup> co-doped with different content of Li<sup>+</sup>

% Li	a (Å)	ε (%)	$D_{W-H}(nm)$	D <sub>Sch</sub> (nm)
0	11.917	$0.0053 \pm 4.79$ E-4	66.2	36
1	11.915	$0.00502 \pm 8.45$ E-4	62.4	36
3	11.918	$0.00409 \pm 0.00165$	62.4	39
5	11.9154	$0.00396 \pm 6.46$ E-4	53.5	35
7	11.923	$0.00535 \pm 0.00182$	53.8	32
9	11.917	$0.00148 \pm 2.24\text{E-4}$	50.5	40
11	11.914	$0.0006 \pm 4.02\text{E-}4$	45.5	41
15	11.909	$0.00116 \pm 5.87$ E-4	47.1	40

Indeed, **Figure III.3b** presents the variation of the peak position  $(2\theta)$  as a function of Li<sup>+</sup> co-doping concentration for the main indicated intense diffraction orientations. One can see that 2θ (°) presents the same profile for all Li<sup>+</sup> contents, indicating that Li<sup>+</sup> has the same influence for all powder diffraction peaks, which can also indicate that Li<sup>+</sup> is inserted in the same way in the different nanoparticles. It is noted that the sample codoped with 7 at. % presents the highest shift towards low angles. Following the variation of the Li<sup>+</sup> concentration, three volume regions can be roughly distinguished, as displayed in **Figure III.3c.** The first region ranges from 0 to 5 at. %, where a fluctuation around an average value is observed, indicating an almost constant behavior. This can be explained by the occupation of Li<sup>+</sup> ions at both interstitial and substitutional sites for low Li+ content. The second region, from 5 to 7 at. %, shows the volume apparently increases, in which one can infer that Li<sup>+</sup> ion might occupy the Al sites due to the difference in ionic radii for six and four coordination number (for CN = 6,  $R_{Li+}$  = 76 pm and  $R_{Al3+}$  = 53.5 pm, for CN = 4,  $R_{\text{Li+}}$  =59 pm and  $R_{\text{Al3+}}$  = 39 pm,). The last region from 7 to 15 at. %, indicates that the LuAG volume decreases due to domination of Li<sup>+</sup> substitutional occupation  $(Li_{Lu_{3+}})$  (for CN= 8,  $R_{Li+}$  =92 pm and  $R_{Lu_{3+}}$  = 97.7 pm). Furthermore, knowing that the Full Width at Half Maximum (FWHM) of diffraction peaks can be interpreted in terms of lattice strain and crystalline size. The crystal lattice strain generated by the annealing temperature is determined from the Williamson-Hall relationship [131]:

$$\beta \times \frac{\cos \theta}{\lambda} = \frac{1}{D} + \eta \sin \theta / \lambda \tag{1}$$

Where  $\beta$  is the full width at half maximum  $\beta = [(\beta_{hkl})_{Measured}^2 - (\beta_{hkl})_{Instrumental}^2]^{1/2}$ ,  $\lambda$  is the X-ray wavelength,  $\theta$  is the diffraction angle, D is the effective crystallite size and  $\eta$  is the effective strain.  $\lambda$  is the wavelength of the X-rays (0.154056 nm).

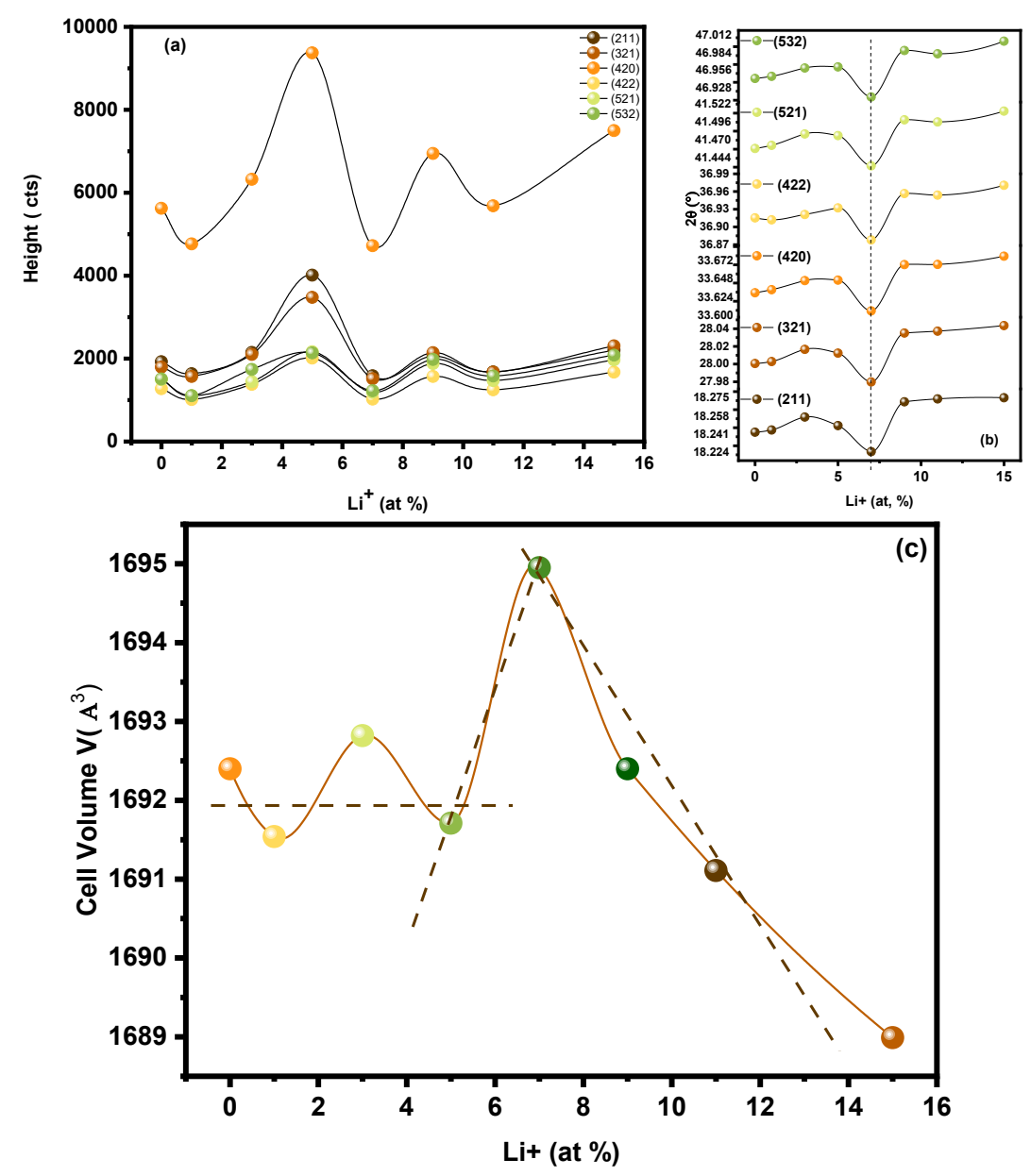


**Figure III.3** (a) Height (cts), (b)  $2\theta$  (°) and (c) the crystal cell volume V(ų) as a function of Li<sup>+</sup> codoping concentration [1].

In **Figure III.4**, we display the variation of the crystallite size and strain with Li<sup>+</sup> co-doping content. One can observe that for Lu<sub>3</sub>Al<sub>5</sub>O<sub>12</sub>: 0.5 at. % Ce<sup>3+</sup>, the crystallite size decreases with an increase in Li<sup>+</sup> co-doping concentration from 66 nm to 47 nm. On the other hand, the strain exhibits the same behavior as the crystallite size, except for 5 at. %, where it increases and then resumes its decline, as shown in **Figure III.5**. Usually, the strain evolves in the opposite direction to the crystallite size. In fact, with a decrease in size, the concentration of the defects at the surface increases, which in turn increases the strain as well. In our case, one can infer that the addition of Li<sup>+</sup> ions reduces the defect content in Lu<sub>3</sub>Al<sub>5</sub>O<sub>12</sub>: 0.5 at Ce<sup>3+</sup> nanocrystallites.

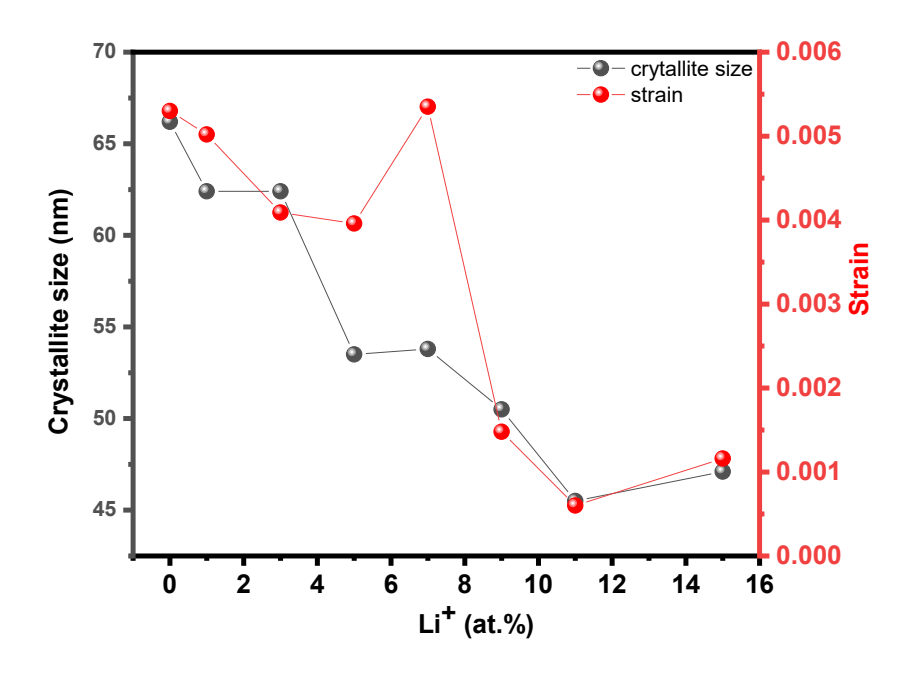


**Figure III.4** Variation of crystallite size calculated by Williamson-Hall formula and the strain with against the Li<sup>+</sup> content [1].

Although the detailed structural analysis of LuAG:Ce,Li has been presented, it is also important to study the effects of codoping with other alkali metal ions, such as Na $^+$  and K $^+$ . Such ions that differ in their ionic radii and charge compensation structures provide a better understanding of the effects of codoping on the structural properties of LuAG:Ce. In the current study, the structural properties of Lu<sub>3</sub>Al<sub>5</sub>O<sub>12</sub>:0.5 at. % Ce<sup>3+</sup> codoped with varying concentrations of Na $^+$  and K $^+$  were analyzed using X-ray diffraction (XRD). The same experimental methodology and synthesis conditions used in the Li $^+$  codoping study were applied here to ensure both consistency and comparability.

XRD patterns of  $\text{Lu}_3\text{Al}_5\text{O}_{12}$ :0.5 at. %  $\text{Ce}^{3+}$  co-doped with  $\text{Na}^+$  and  $\text{K}^+$  (1, 3, 5, 7, 11, and 15 at. %) are presented in **Figure III.5** and **Figure III.6**, respectively. All diffraction peaks align with the cubic garnet structure (JCPDS no. 73-1368) and the *Ia3d* space group symmetry, confirming that the primary LuAG phase is preserved. The samples exhibit a preferential orientation along the (420) plane, consistent with JCPDS no. 73-1368.

For Na<sup>+</sup> co-doping, the highest peak intensities are observed at 1 at. % and 7 at. %, while for K<sup>+</sup> co-doping, the strongest peaks appear at 5 at. % and 15 at. %. The variation in diffraction peak positions indicates lattice expansion with increasing codopant content, more noticeably for K<sup>+</sup> due to its larger ionic radius.

The derived structural parameters for Na<sup>+</sup> and K<sup>+</sup> co-doped samples, including lattice constant (a), crystallite size (D), and strain ( $\varepsilon$ ), are summarized in **Table III.2** and **Table III.3**. A comparison with Li<sup>+</sup> co-doping shows similar structural behavior with preservation of the cubic phase (JCPDS no. 73-1368), but with distinct trends due to differences in ionic radius.

For Na $^+$  co-doping, the lattice constant varies between 11.916 Å and 11.936 Å, suggesting that Na $^+$  ions may occupy both interstitial and substitutional sites at low concentrations, while substitutional incorporation dominates at higher concentrations. The crystallite size increases significantly compared to the undoped sample (66.2 nm), with a maximum of 129.2 nm at 11 at. %, and other high values also noted at 1, 5, and 7 at. %.

In the case of  $K^+$  co-doping, the lattice constant increases slightly, reaching a maximum of 11.929 Å at 11 at. %, indicating substitutional incorporation of  $K^+$  at  $Lu^{3+}$  sites. The crystallite size increases with doping, peaking at 108.1 nm at 11 at. %, followed by a decrease to 93.3 nm at 15 at. %, which may be due to increased lattice distortion and defect formation at high dopant levels.

These results confirm that both Na<sup>+</sup> and K<sup>+</sup> co-doping impact the structural parameters of LuAG:Ce, and provide valuable insight into how alkali ions influence crystallinity and lattice behavior in garnet-type scintillators.

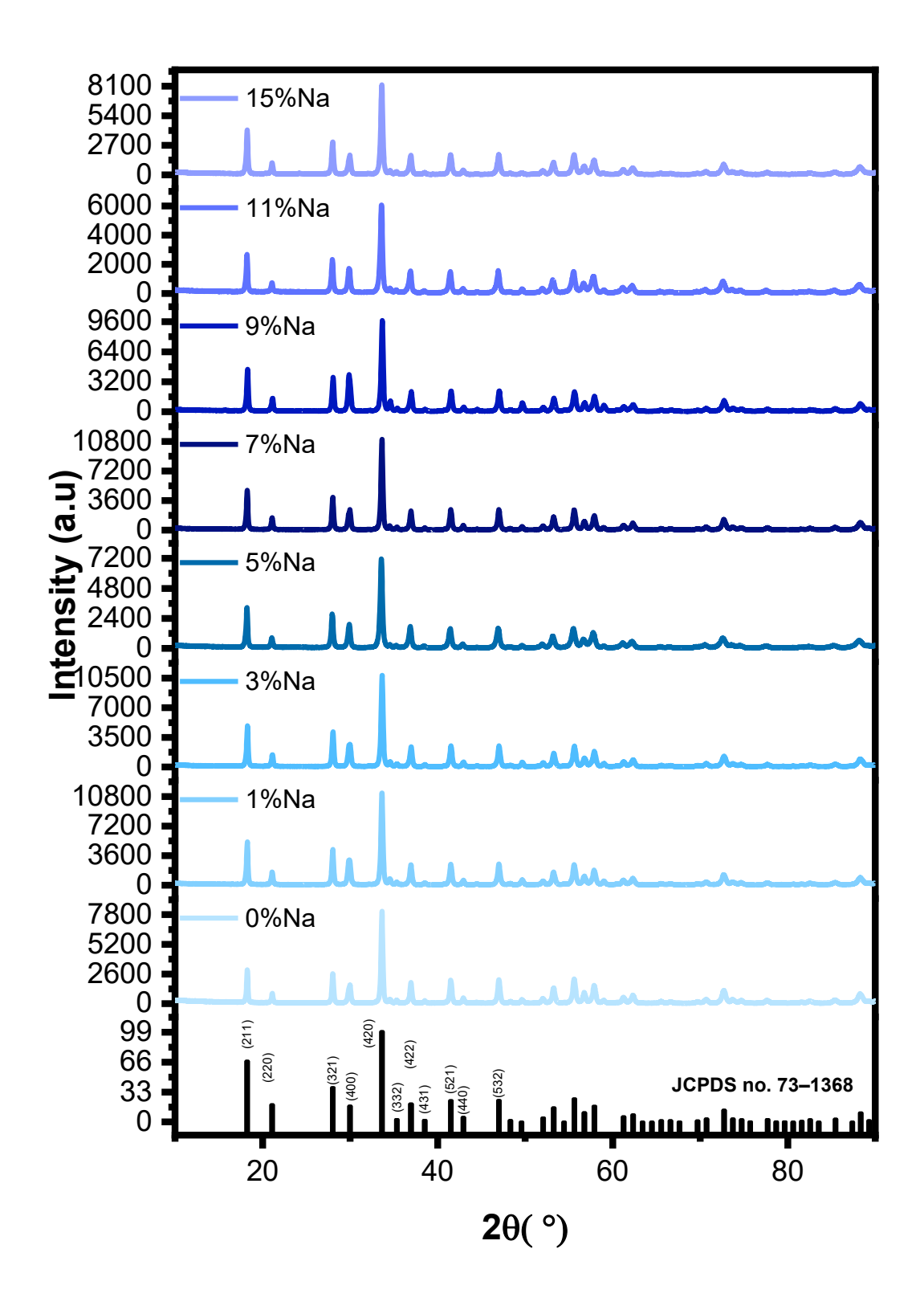


**Figure III.5** XRD patterns of Lu<sub>3</sub>Al<sub>5</sub>O<sub>12</sub>: 0.5 at. % Ce <sup>+3</sup>, co-doped with different Na<sup>+</sup> co-doping concentration.

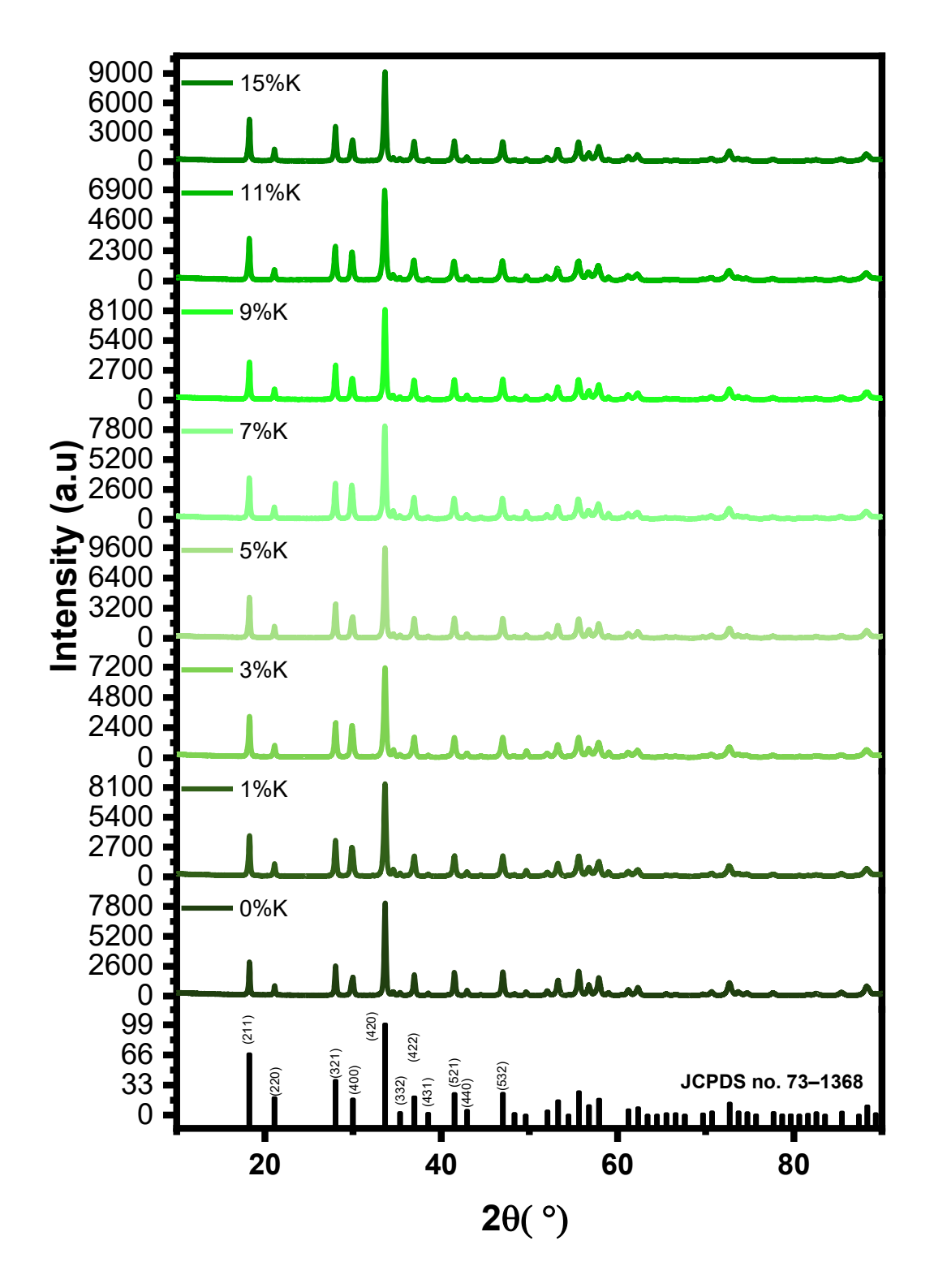


**Figure III.6** XRD patterns of Lu $_3$ Al $_5$ O $_{12}$ : 0.5 at. % Ce  $^{+3}$ , co-doped with different K $^+$  co-doping concentration.

**Table III.2** Structural parameters for samples of LuAG: 0.5% Ce<sup>3+</sup> co-doped with different content of Na<sup>+</sup>.

% Na	a (Å)	ε (%)	$D_{W-H}$ (nm)	D <sub>Sch</sub> (nm)
0	11.917	$0.0053 \pm 4.79$ E-4	66.2	36
1	11.919	$0.00198 \pm 1.99$ E-4	100.7	66
3	11.916	$0.00217 \pm 4.55$ E-4	100.1	64
5	11.936	$0.00464 \pm 5.34$ E-4	124.4	55
7	11.918	$0.00191 \pm 4.25$ E-4	101.0	69
9	11.916	$0.00249 \pm 0.00101$	99.0	64
11	11.932	$0.00416 \pm 6.08\text{E-}4$	129.2	58
15	11.921	$0.00353 \pm 5.24\text{E-4}$	114.5	61

**Table III.3** Structural parameters for samples of LuAG: 0.5% Ce<sup>3+</sup> co-doped with different content of K<sup>+</sup>.

% K	a (Å)	ε (%)	$D_{W-H}(nm)$	D <sub>Sch</sub> (nm)
0	11.917	$0.0053 \pm 4.79$ E-4	66.2	36
1	11.922	$0.00137 \pm 0.00302$	84.4	58
3	11.923	$0.00367 \pm 8.72$ E-4	100.9	56
5	11.921	$0.00271 \pm 4.53E-4$	99.2	61
7	11.926	$0.00365 \pm 7.14$ E-4	102.9	57
9	11.920	$0.00154 \pm 0.00194$	81.6	59
11	11.929	$0.00479 \pm 8.85$ E-4	108.1	51
15	11.924	$0.00277 \pm 5.28E-4$	93.3	58

Contrary to Li<sup>+</sup>, codoping of LuAG:Ce<sup>3+</sup> with Na<sup>+</sup> and K<sup>+</sup> leads to greater lattice expansion and local deformation as a direct consequence of their larger ionic radii. While crystallite size peaks at low codoping concentrations for all three alkali ions, the maximum size obtained with Na<sup>+</sup> and K<sup>+</sup> significantly exceeds that of Li<sup>+</sup>. These findings highlight the significant influence of ionic radius and codoping concentration on structural stability and crystallinity.

In summary, Na<sup>+</sup> and K<sup>+</sup> codoping modifies the structural properties of LuAG:Ce<sup>3+</sup> compared to Li<sup>+</sup> in a unique way, at optimized concentrations, phase purity is preserved, but these larger ions introduce lattice distortions and distinct crystallite growth patterns. These ion-specific effects offer a valuable route map for garnet-based scintillator engineering, allowing precise control of structural properties to meet targeted performance requirements in radiation detection or imaging applications.

#### **III.1.2 VASP simulation**

To carry out the *DFT* calculations, we considered the different possible situations in which Li<sup>+</sup> can be placed. We placed the Li<sup>+</sup> ion in substitution at the two inequivalent Al sites (Li<sub>Al</sub>) (the 24d site with the  $T_d$  symmetry and the 16a site with the  $O_h$  symmetry) and the Lu site (Li<sub>11</sub>) and in some interstitial positions as shown in **Figure III.2**. We applied the same calculation method for each situation and studied the electronic properties. It is worth noting that the calculations were done without any correction (DFT+U). It is important to note that for the interstitial configuration, the system did not reach the ground state (not converged). The **Figure III.7**, depicts the calculated density of states (DOSs) of LuAG:Ce co-doped Li<sub>11</sub>, LuAG: Ce co-doped Li<sub>11</sub>. For substitutional Li<sub>11</sub>, the partial density of state (PDOS) does not show the 4f state of the cerium ion in the LuAG bandgap. In contrast, in the case in which Li is on Al ( $Li_{Al-24d}$ ), the *PDOS* shows a very pronounced double 4f state in the bandgap, situated at 2.07 eV above the valence band maximum. Furthermore, by calculating the formation energy, we found that Li<sub>Al</sub> is more stable on the 24d site than on the 16a site by 0.36 eV. The calculated total energy of the system for each situation are -1249.571 eV, -1250.210 eV and -1246.958 eV for LuAG: Ce, LuAG:Ce, Li<sub>Al</sub> and LuAG: Ce, Li<sub>Lu</sub> respectively. One can see that in Li<sub>Al-24d</sub> situation, the system is much more stable than the Li<sub>11</sub> and without Li<sup>+</sup>. Recently, Derdzyan et al [132] showed that Li<sup>+</sup> in LuAG: Ce bulk material is localized at Lu<sup>3+</sup> sites with charge compensation caused by  $Ce^{3+} \rightarrow Ce^{4+}$  conversion and the creation of anion vacancies. In contrast, Wu et al. [133] showed that the Li<sup>+</sup> ions prefer to dominantly occupy the fourfold coordinated interstitial sites and fourfold coordinated Al sites in LuYAG codoped with Li<sup>+</sup> and Pr<sup>3+</sup> single crystal and codoping with Li does not induce the conversion of stable Pr<sup>3+</sup> to Pr<sup>4+</sup>. Furthermore, it can be assumed that the concentration of isolated Lu<sup>3+</sup> and Al<sup>3+</sup> ion vacancies

as dominant acceptor defects are slightly reduced by Li co-doping, while deep oxygen vacancies  $V_0$  are generated. Thus, reducing the hole trapping energy and cross sections by inserting the codopant Li, especially into the aluminum site (24d) can increase the hole trapping probability by  $Ce^{3+}$  and improve light efficiency.

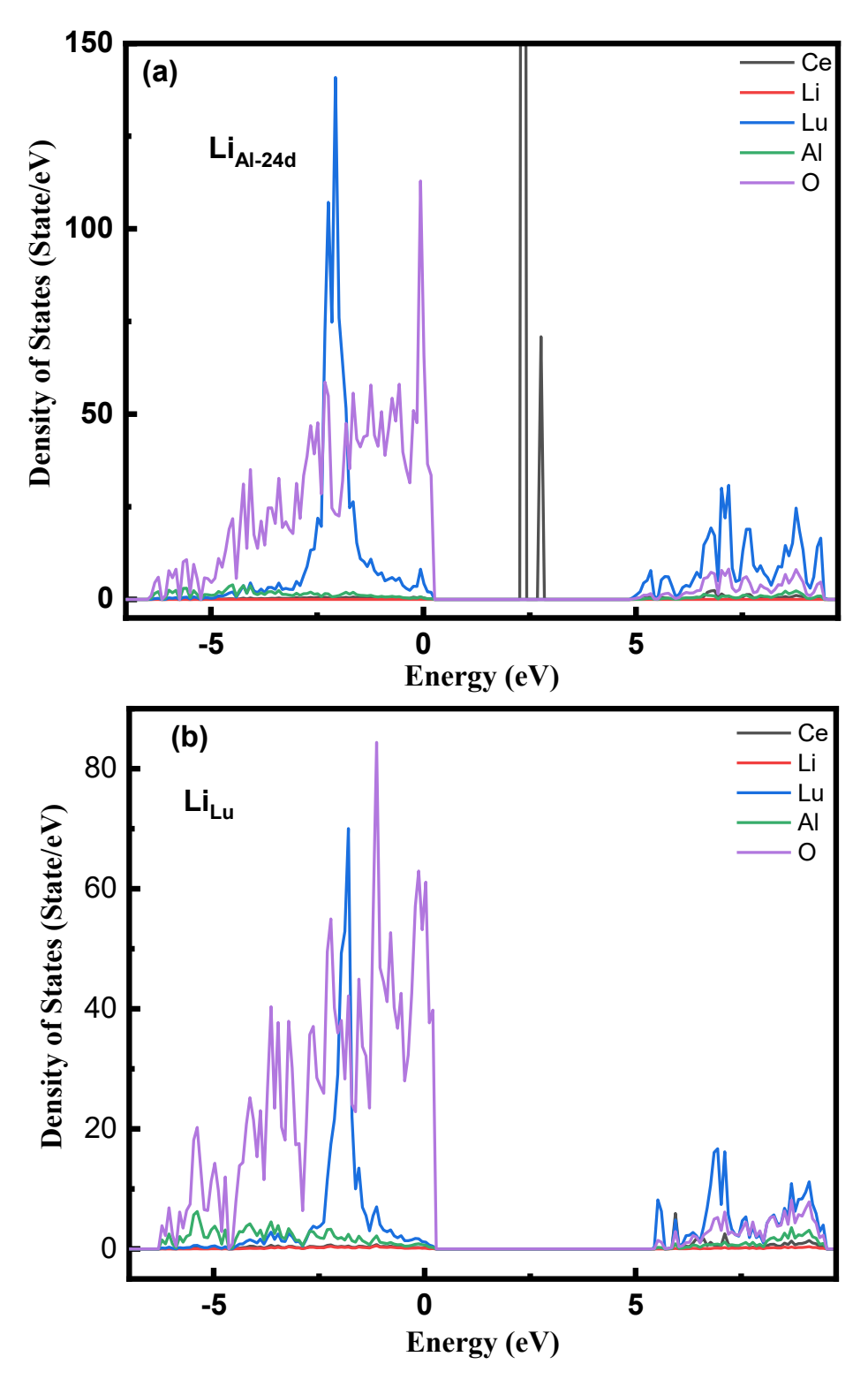


**Figure III.7:** Density of State for (a): LuAG:Ce co-doped  $\text{Li}_{\text{Al-24d}}$  substitute defect, (b) LuAG: Ce co-doped  $\text{Li}_{\text{Lu}}$  [1].

#### III.1.3 Morphological analysis

Surface morphology is one of the important factors affecting the performance of scintillator nanoparticles. **Figure III.8** shows the FE-SEM images of three samples, namely LuAG:  $Ce^{3+}$ , x at. % Li<sup>+</sup> (x = 0, 5 and 15). The FESEM images show that the addition of Li resulted in a change in the morphology of the materials. From the Figure III.8. one can observe that LuAG: Ce<sup>3+</sup> without Li<sup>+</sup> presents cubic-shaped particles connected by one of their faces (see enlarged figure inset), exhibiting a dense surface. These particles in cubic form are themselves constituted by the agglomeration of LuAG nano-crystallites. As the Li<sup>+</sup> content increases, the morphology loses its cubic shape and begins to become spherical with better dispersion and the particle size is reduced, indicating slight agglomeration (Figure III.8 and insets). Also, the SEM image analysis confirmed that the addition of Li<sup>+</sup> co-doping resulted in a decrease in the crystallinity of the materials, which is in good agreement with XRD analysis (Figure III.1). EDS of the top view of the powder samples was performed. The estimation of the atomic percentage (at. %) for each sample was made at three different points on the surface and we give an average. As shown in **Figure III.8,** the elemental composition of the samples is presented. In table III.4, we present the stoichiometric ratios between the different elements found. From table III.4, we note that the sample with 5 at % Li<sup>+</sup> provides ratio values close to that the theoretical one (ideal), due to the absence of LuAP parasitic phase.

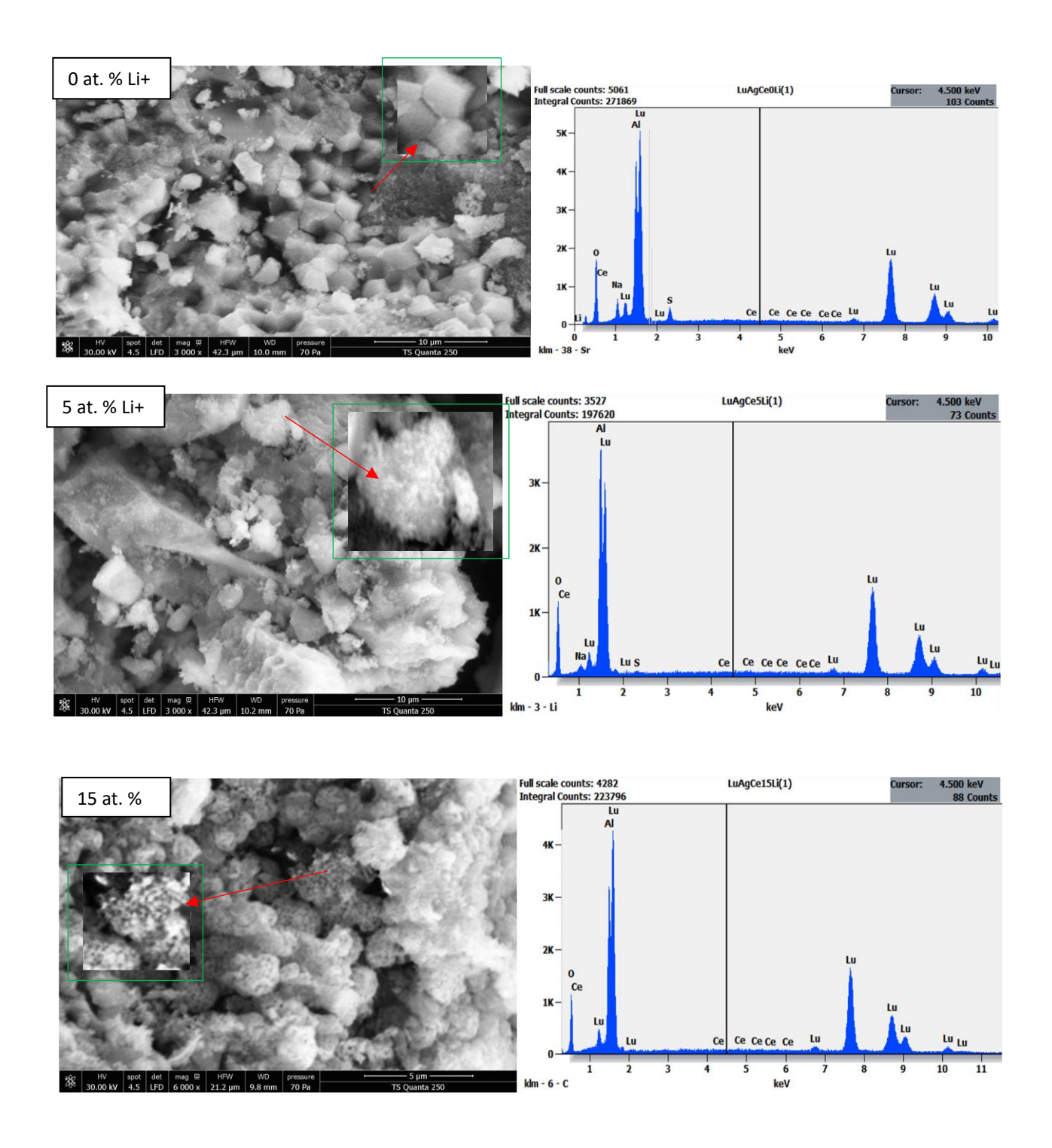


**Figure III.8:** Left: FE-SEM images of three samples, namely LuAG:  $Ce^{3+}$ , x at. %  $Li^{+}$  (x = 0, 5 and 15), insets, enlarged regions corresponding to the origins of the arrows. Right the corresponding attached EDS spectra [1].

 $\textbf{Table III.4} \ \ Stoichiometric \ ratios \ between \ the \ different \ elements \ in \ Lu_3Al_5O_{12} : Ce^{3+}, \ Li^{+}$ 

Elements	% atomic	R(Lu/Al) = 0.6	R(O/Al) = 2.4	R(O/Lu) = 4	
	0%Li <sup>+</sup>				
Lu	12.26				
Al	22.81	0.54	2.84	5.29	
0	64.89				
Ce	0.04				
	5%Li⁺				
Lu	13.94				
Al	22.38	0.62	2.84	4.56	
0	63.60				
Ce	0.08				
	15%Li <sup>+</sup>				
Lu	16.68				
Al	19.58	0.85	3.25	3.81	
0	63.69				
Ce	0.05				

## **III.1.4 Photoluminescence study**

The photoluminescent properties of LuAG:Ce (Lutetium Aluminum Garnet doped with Cerium) were investigated with a particular focus on the effects of Li<sup>+</sup> co-doping. This detailed study explored how Li<sup>+</sup> influences emission intensity, peak positions, and overall luminescence efficiency. To provide a benchmark for comparison, The results were compared to single-crystal (SC) LuAG:Ce, which serves as a reference for optimal performance.

While this section briefly discusses the impact of Na<sup>+</sup> and K<sup>+</sup> co-doping, the primary emphasis was on LuAG:Ce,Li due to its distinct behavior and potential for enhancing photoluminescence properties. Additional analyses including spectroscopic measurements were carried out in the case of Li<sup>+</sup> co-doping to gain a deeper understanding of the material's properties.

### III.1.4.1 photoluminescence steady state

displays the room-temperature **Figure** III.9a emission spectra of Lu<sub>2·985-x</sub>Li<sub>x</sub>Ce<sub>0·015</sub>Al<sub>5</sub>O<sub>12</sub> powders co-doped with varying Li<sup>+</sup> concentrations. The samples were synthesized via the sol-gel method and calcined at 1100 °C for 2 hours. All spectra were measured under an excitation wavelength of 450 nm (corresponding to the Ce<sup>3+</sup> transition from the ground state to the  $5d_1$  energy level) within the 450-630 nm range. The emission spectra exhibit intense, broad, and asymmetric bands, which were deconvoluted into two Gaussian components separated by approximately 1500 cm<sup>-1</sup> (as shown in **Table III.5**). These bands correspond to spin-allowed electric dipole transitions from the lowest  $5d_1$  energy level of  $Ce^{3+}$  to the  ${}^2F_{5/2}$  and  ${}^2F_{7/2}$  states of the 4f ground level. Furthermore, the influence of Li<sup>+</sup> co-doping on the integrated emission intensity is presented in **Figure 9b**. Among the co-doped samples, the highest intensity is observed at 5 at. % Li<sup>+</sup>, although it remains below that of single-crystal LuAG:Ce (SC) and similar to the Li<sup>+</sup>-free sample. In general, the addition of Li<sup>+</sup> reduces the photoluminescence (PL) intensity compared with indoped LuAG:Ce and LuAG:Ce SC. This reduction is due to the possibility of Ce<sup>4+</sup> formation and/or quenching processes such as transfer of energy to surface defects or impurity ions by synthesis conditions. Notably, the highest luminescence intensity for many rare-earth-doped nanomaterials is typically obtained in larger crystallite size samples due to better crystallinity. In this study, though, PL intensity does not directly correlate with crystallite size in a function of Li<sup>+</sup> concentration (**Figure III.9c**). There are similar observations in the literature including the reports by Ferreiro et al. for Nd3+-doped ZnO nano-materials [5] as well as Ningombam et al. for YVO<sub>4</sub>:Eu<sup>3+</sup> nano-crystals [6]. Ningombam et al. reported that the crystallite size of YVO<sub>4</sub>:Eu<sup>3+</sup> increases with increasing of Li<sup>+</sup> codoping, the highest PL intensity was found to be produced at an optimum 5% Li<sup>+</sup> concentration followed by a decrease at higher codoping concentrations as a result of luminescence quenching. The luminescence efficiency depends not only on crystallite size but also on factors such as phase purity, Ce<sup>3+</sup>/Ce<sup>4+</sup> ratio, and defect density. Smaller crystallites tend to have more grain boundaries, leading to dangling bonds or disordered atomic arrangements that can quench luminescence. Phonons associated with surface vibrations in nanocrystals can further introduce non-radiative relaxation pathways, limiting luminescence efficiency [134]. Furthermore, the superior luminescence observed at 5 at. % Li<sup>+</sup> is likely related to the formation of a phase-pure garnet structure. In the absence of parasitic phases, all Ce<sup>3+</sup> ions are expected to occupy Lu<sup>3+</sup> sites in the LuAG garnet, contributing to green emission. Conversely, the presence of parasitic phases such as LuAlO<sub>3</sub> (LuAP) may cause some Ce<sup>3+</sup> ions to substitute Lu<sup>3+</sup> in these secondary phases, leading to UV emission and reduced green emission intensity [135]. The addition of Li<sup>+</sup> ions as a codopant improves both morphological regularity and crystallinity leading to a smoother and more uniform spatial distribution of Ce<sup>3+</sup> ions, as observed in both X-ray diffraction (XRD) and scanning electron microscopy (SEM) data. Another possibility to compensate for the charge imbalance caused by oxygen vacancies is produced during heat treatment through Li<sup>+</sup> substitution for Ce<sup>3+</sup> or Lu<sup>3+</sup> in LuAG material's properties [136]. On the other hand, excess Li<sup>+</sup> codoping (>5 atomic %) leads to crystallographic defects on the surface that reduce the efficiency of light emission which establishes an optimal Li<sup>+</sup> concentration of 5 at. % to balance structural integrity and luminescent performance. Such observations are consistent with previous studies for instance, Ponkumar et al. [137] showed that the optimum Li<sup>+</sup> concentration in ZrO<sub>2</sub>:Eu<sup>3+</sup> results from interdependent factors including charge balance tuning, lattice deformation and phase transitions. In the same way, Shanbhag et al [138] found an increase in the luminescence in CaTiO<sub>3</sub>:Sm<sup>3+</sup> with progressive Li<sup>+</sup> addition up to a threshold concentration above which quenching of the emission dominates. However, in LuAG:Ce ceramics, Zhang et al [137] reported that maximum luminescence was observed at 3 wt.% LiF additive and that higher concentrations reduced the intensity of emission comparable trends have been observed in other systems, such as Li<sup>+</sup> co-doped  $Y_3Al_5O_{12}$ :Tm<sup>3+</sup>, ZnO:Tb<sup>3+</sup>, and BaSiF<sub>6</sub>:Dy<sup>3+</sup>, where optimal Li<sup>+</sup> concentrations enhanced PL intensity by improving crystallinity, modifying local environments, and acting as a charge compensator [139-141].

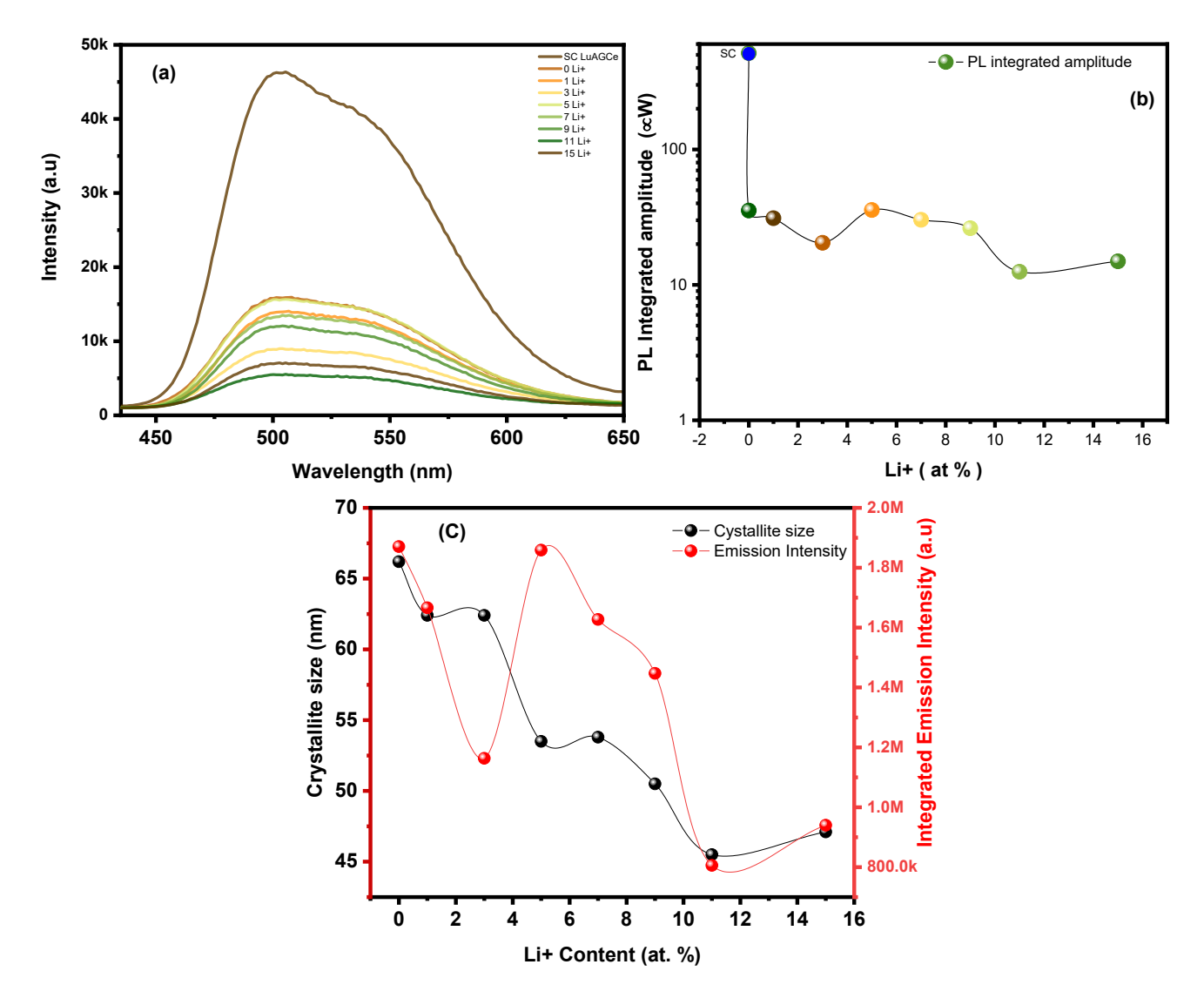


**Figure III.9 (a)** Room temperature emission spectra of Lu<sub>2.985-x</sub>Li<sub>x</sub>Ce<sub>0.015</sub> Al<sub>5</sub>O<sub>12</sub> Co-doped by different content of Li<sup>+</sup> powders and single crystal (SC) **(b)** Variation of integrated intensities with Li<sup>+</sup> co-doping concentrations **(c)** Variation of integrated intensities as well as crystallite size in function of Li<sup>+</sup> content [1].

All samples present the same excitation spectra as shown on the right side of **Figure III.10**, which consist of two broad intense bands centered around 450 nm and 347 nm. These bands correspond to the absorption of the incoming radiation by  $Ce^{3+}$  ions. Specifically, the excitation bands originate from electric-dipole inter-configurational transitions between the4f<sup>1</sup> ground state ( ${}^{2}F_{5/2}$ ) and the first and second excited energy

levels of the 5d1 configuration (5d<sub>1</sub> and 5d<sub>2</sub>), respectively. Furthermore, the higher excitation states of  $Ce^{3+}$  (5d<sub>3</sub>, 5d<sub>4</sub>, 5d<sub>5</sub>) and the host can also be observed. [1]

Due to the strong interaction of the 5d state electrons with the crystal lattice, the 4f-5d absorption and the 5d-4f emission mainly depend on the host. Therefore, it is important to estimate and analyze the main spectral parameters resulting from the  $4f\leftrightarrow 5d$  transitions indifferent hosts. These parameters are namely the crystal field splitting and the electron-vibration interaction (EVI) of the 5d electronic states of  $Ce^{3+}$  with a crystal lattice environment. When  $Ce^{3+}$  ion is inserted in LuAG material, its 5d level is lowered relative to its position in the free ion by a quantity referred to as spectroscopic redshift D (LuAG) [57]. (Fig.9) and determined from the excitation spectrum using the following expression:

$$D(Ce^{3+}, LuAG) = E(Ce^{3+}, Free) - E(Ce^{3+}, LuAG)$$
 (2).

Where  $E(Ce^{3+}, free)$  is the excitation energy of the free  $Ce^{3+}$  ion from the 4f ground level to the lowest 5d level, and  $E(Ce^{3+}, LuAG)$  is the corresponding energy in the LuAG material.  $E(Ce^{3+}, free)$  was taken equal to 49340 cm<sup>-1</sup> [57].

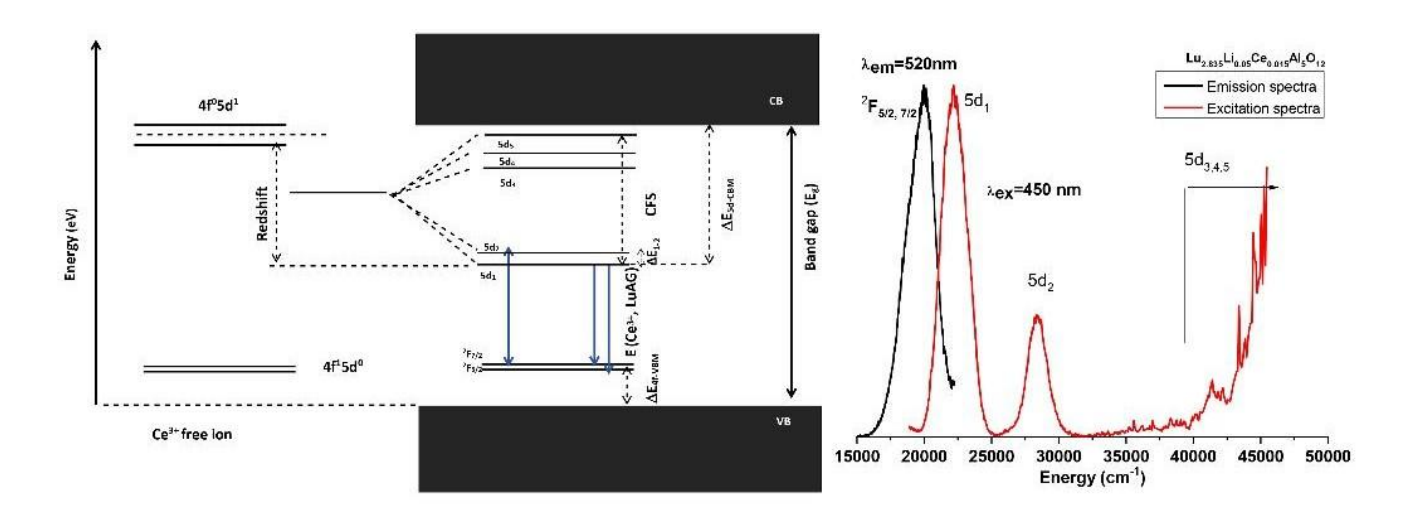


**Figure III.10** Right, Excitation and emission spectra of LuAG: 0.5%Ce<sup>3+</sup>Co-doped by Li<sup>+</sup> powders. Left: Ce<sup>3+</sup> 4f and 5d level positions relative to LuAG electronic bands. The band gap (Eg), The redshift D (Ce<sup>3+</sup>, LuAG), the Crystal Field Splitting (CFS), the lowest 4f ↔5d energy transition E (Ce<sup>3+</sup>, LuAG), and the energies  $\Delta E_{4f\cdot VB}$ ,  $\Delta E_{5d\cdot CB}$  are shown [1].

**Figure III.11** illustrates the variation in crystal field splitting between the lowest 5d₁ and  $5d_2$  levels ( $\Delta E_{12}$ ) and the redshift ( $\Delta (Ce^{3+}, LuAG)$ ) as a function of Li<sup>+</sup> content, including data for the single crystal (SC). It is evident that both  $\Delta E_{12}$  and  $\Delta (Ce^{3+}, LuAG)$  follow a similar trend, except for the SC and the sample co-doped with 1 at. % of Li<sup>+</sup>. This observation suggests that the  $\Delta E_{12}$  splitting significantly influences the redshift, it was found that the large redshift in the  $RE_3(Al_{1-x}Ga_x)5O_{12}$  garnet family must be attributed to the additional  $\Delta_{12}$  splitting of the 5d levels [142]. As known that the 5d states strongly interact with crystal lattice and the  $4f \leftrightarrow 5d$  excitation and emission transitions are essentially host-dependent. Therefore, it is important to analyze the main spectral features of  $4f \leftrightarrow 5d$  transitions for different Li<sup>+</sup> contents in LuAG: Ce<sup>3+</sup> host material and also to estimate the basic parameters of the electron-vibrational interaction (EVI) of the 5d electronic states of Ce<sup>3+</sup> with the crystal lattice environment. To this purpose, a single configuration coordinate model [76]. Additionally, evaluating the fundamental parameters of the electron-vibrational interaction (EVI) for the 5d electronic states of Ce<sup>3+</sup> within the crystal lattice environment provides valuable insights into the luminescent behavior of these materials.

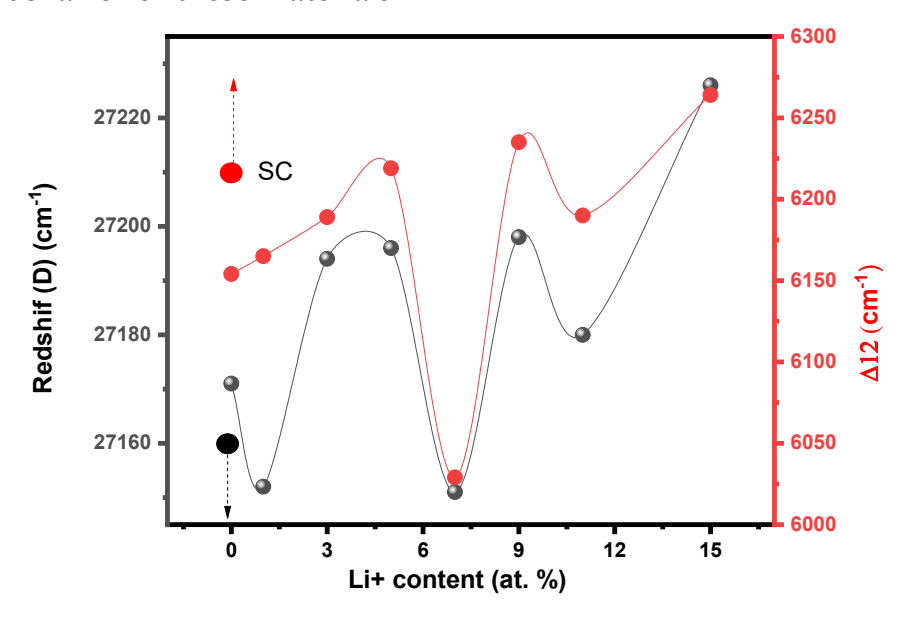


**Figure III.11** Variation of the crystal field splitting of the lowest  $5d_1$ - $5d_2$  levels ( $\Delta_{12}$ ) as well as redshift (D (Ce<sup>3+</sup>, LuAG)) as a function of Li<sup>+</sup> content. Values for the single crystal (SC) are shown [1].

To achieve this, we used a single configuration coordinate model [20], illustrated in **Figure III.12**, which is based on quantum mechanics and allows precise fitting of the

emission band. This approach enabled us to determine several important spectroscopic parameters related to electron-phonon interactions. These include the positions of the emission and excitation bands, the Stokes shift ( $\Delta$ ES), the redshift (D(LuAG)), the Zero Phonon Line (ZPL) energy, the effective phonon energy ( $\hbar\omega$ ), and the Huang-Rhys coupling constant (S).

In fact, the Stokes shift is considered as the energy difference between the absorption and the highest energy ( $5d\rightarrow 2F_{5/2}$ ) Gaussian emission maximum bands. Furthermore, the Huang-Rhys parameter (S) measures the strength of electron-phonon coupling and is directly proportional to the Stokes shift ( $\Delta$ ES). The effective phonon energy ( $\hbar\omega$ ) was also calculated for LuAG:Ce<sup>3+</sup> co-doped with Li<sup>+</sup> [74].

By analyzing these parameters, we gain a deeper understanding of how Ce<sup>3+</sup> ions interact with the crystal lattice and how these interactions affect the luminescent properties of Li<sup>+</sup> co-doped LuAG materials.

$$\Delta E_{\rm S} = (2S - 1) \,\hbar \omega \tag{3}$$

$$\Gamma(T) = FWHM(T) = \sqrt{8ln2}. \,\hbar\omega. \left[ S. \coth\left(\frac{\hbar\omega}{2.kT}\right) \right]^{1/2}$$
(4)

Where  $\Gamma(T)$  represents the full width at half maximum *(FWHM)* of the emission band and k is the Boltzmann constant. By solving the system of equations (3) and (4), the values of S (Huang-Rhys coupling constant) and  $\hbar\omega$  (effective phonon energy) were determined for each Li<sup>+</sup> content using the experimental data summarized in **Table III.5**.

From the table, it can be observed that the single crystal (SC) exhibits strong electron-phonon coupling, with S=5.99, which is higher than that of the nanomaterials, indicating an intermediate coupling for the latter. Additionally, the effective phonon frequency ( $\hbar\omega$ ) for the SC is smaller than that of the nanomaterials. The SC sample also shows a larger Stokes shift compared to the nanomaterials, suggesting stronger self-absorption due to Ce<sup>3+</sup> at the nanoscale. Ogiegło et al. [144] reported a significant Huang-Rhys coupling constant (S=9) determined at low temperatures. For the SC in this study, the result aligns well with previously published values, including S=6.6 for LuAG:Ce<sup>3+</sup> reported by Nair et al. [145] and S=6 for Ce<sup>3+</sup> luminescence in YAG:Ce<sup>3+</sup> garnet material as noted by Bachmann et al. [146].

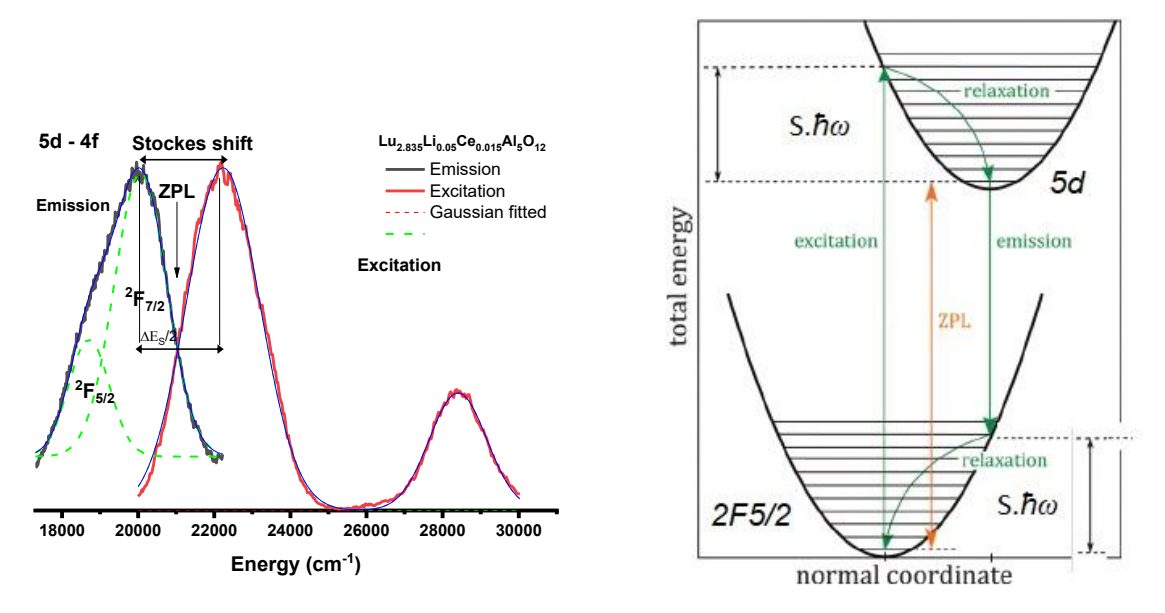


**Figure III.12** Emission and excitation spectrum fitted by two Gaussian curves showing the Stokes Shift and ZPL. Franck–Condon diagram of the ground and excited states of the optical center in solids.

**Table III.5** Excitation and emission maxima, *FWHM*, Stokes shift, Huang-Rhys parameters of LuAG: Ce<sup>3+</sup>, Li<sup>+</sup>nanophosphors and that of single crystal (SC).

spectroscopic	0% Li	1% Li	3% Li	5% Li	7% Li	9% Li	11% Li	15% Li	SC
quantity									
$5d_1$	22169	22188	22146	22144	22189	22142	22160	22114	22614
$5d_2$	28323	28353	28335	28363	28218	28377	28350	28378	29394
$5d-4f_{5/2}$	20302	20276	20331	20302	20298	20259	20341	20314	20018
$5d-4f_{7/2}$	18506	18518	18562	18477	18500	18445	18398	18503	18457
FWHM	1729	1617	1568	1694	1693	1678	1888	1611	1361
$(5d-4f_{5/2})$									
$\Delta E(5\mathbf{d}_1-5\mathbf{d}_2)$	6154	6165	6189	6219	6029	6235	6190	6264	6780
D (Ce <sup>3+</sup> , LuAG)	27171	27152	27194	27196	27151	27198	27180	27226	26726
Stokes shift	1867	1913	1815	1842	1891	1883	1819	1800	2595
ħω	463	407	400	451	443	437	542	422	236
S	2.518	2.851	2.768	2.541	2.635	2.653	2.179	2.634	5.996

Following the detailed analysis of LuAG:Ce,Li a brief study was carried out to investigate the effect of Na<sup>+</sup> and K<sup>+</sup> co-doping on the photoluminescence (PL) properties of LuAG:Ce.

**Figure III.13** illustrates the excitation and emission spectra of LuAG:Ce , codoped with different concentrations of sodium Na<sup>+</sup> (right) and potassium K<sup>+</sup> (left). These co-dopants are used to study their effects on the optical properties of the phosphorescent material, in particular its 5d-4f transitions which are typical of Ce<sup>3+</sup> ions. Both Figures exhibit broad excitation bands measured under emission wavelength  $\lambda_{em}$ = 510 nm for LuAG:Ce,Na and  $\lambda_{em}$ = 520 nm LuAG:Ce,K in the UV and visible regions, typical of Ce<sup>3+</sup> ions. These bands correspond to electronic transitions from the ground state (4f) to the excited states (5d) of Ce<sup>3+</sup>, increasing the concentration of Na<sup>+</sup> or K<sup>+</sup> leads to notable shifts in peak position and intensity changes. This indicates that the codopants affect the local crystal field around the Ce<sup>3+</sup> ions, changing their energy levels.

The emission spectra of both figures were measured at an excitation wavelength of 440 nm (LuAGCe,Na) and 450 nm (LuAGCe,K) in the range 450-630 nm, which corresponds to the  $Ce^{3+}$  transition from the ground state to the  $5d_1$  energy level. Both codopants affects luminescence enhancement at low concentrations, but less effectively than  $Li^+$ . Their larger ionic radii, however, introduce lattice distortion at higher levels leading to quenching effects.  $K^+$  shows slightly more distortion than  $Na^+$  due to its larger size.

The different spectra suggest that Na<sup>+</sup> and K<sup>+</sup> codoping have a different impact on the crystal structure. The results suggest that Li<sup>+</sup> codoping holds the most potential for improving the performance of LuAG:Ce, particularly for applications in scintillators and light-emitting devices. Careful control of the dopant concentration is essential to achieve optimal results.

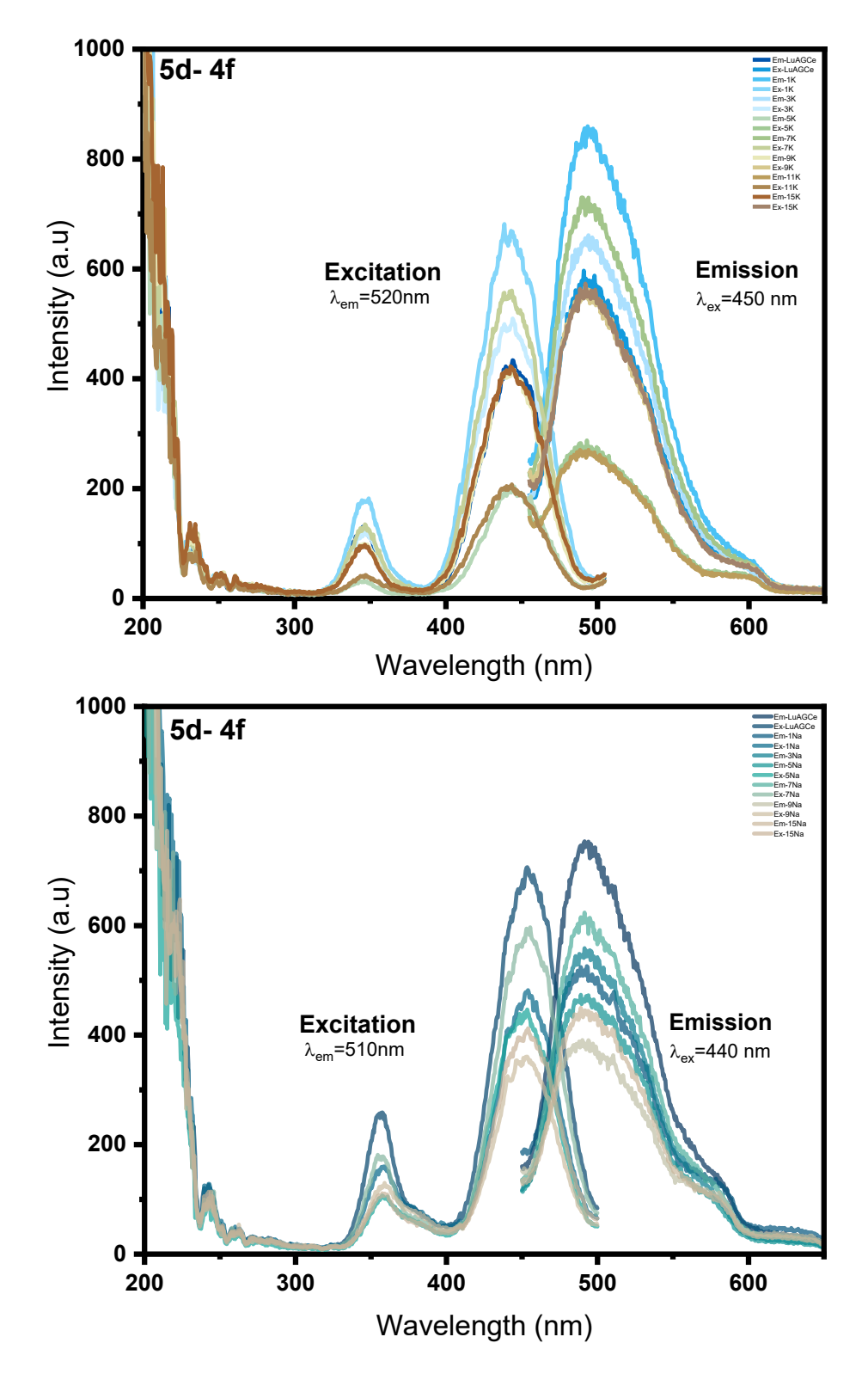


**Figure III.13** Room temperature emission and excitation spectra of LuAG: 0.5 at. %  $Ce^{3+}$  Codoped by different content of  $K^+$  (top) and by different content  $Na^+$  (bottom) powders.

This table outlines that  $\text{Li}^+$  coding offers the best luminescence enhancement due to its effective charge compensation and minimal lattice distortion, making it preferable to  $\text{K}^+$  and  $\text{Na}^+$  codopants.

Parameter	SC LuAG:Ce	LuAG:CeLi	LuAG:CeK	LuAG:CeNa	
Emission intensity	Highest (Reference)	Enhanced (Optimal at 5 at. %)	Moderate improvement	Moderate improvement	
Optimal dopant	/	5 at. % Li+	Low concentration (> 5 at. %)	Low concentration (> 5 at. %)	
Luminescence Quenching			Significant at > 5 K	Noticeable at > 5 Na	
Crystal distortion	Minimal at low Minimal levels		Moderate at high content	Moderate at high content	
Charge compensation	/	Most effective	Effective at low content	Effective at low content	
Defect formation	Minimal	Low (optimal condition)	Moderate at high cooping	Moderate at high cooping	
Overall performance	Reference	Best codopant (optimal Li)	Less effective than Li	Comparable to K but less effective than Li	

## III.1.4.2 Time resolved photoluminescence

**Figure III.14a** shows the room-temperature PL decay curves for LuAG: 0.5% Ce<sup>3+</sup> powders co-doped with Li<sup>+</sup>, along with the decay curve for the single crystal (SC). After deconvolution taking into account the instrument response function (IRF), all decay curves were accurately fitted using a three-exponential function

I (t) =  $A_1 \exp\left(-\frac{t}{\tau_1}\right) + A_2 \exp\left(-\frac{t}{\tau_2}\right) + A_3 \exp\left(-\frac{t}{\tau_3}\right) + I_0$ , where  $A_1$ ,  $A_2$  and  $A_3$  are the corresponding initial intensities of the pulse shape components and  $I_0$  is a time independent background intensity. For the LuAG:Ce<sup>3+</sup> single crystal (SC), the PL decay curve is best described by a single exponential function, as shown in **Figure III.14b**. The decay times extracted from the fits are summarized in **Table III.6**. The contribution of the j<sup>th</sup> decay component  $\tau_j$  (with j=1, 2, 3) is calculated using the following formula:

 $W_{j} = \frac{A_{j}\tau_{j}}{\sum_{i=1}^{3}A_{i}\tau_{i}}$ , where  $A_{i}$  and  $\tau_{i}$  are the amplitude and decay time of the i<sup>th</sup> component, respectively [1].

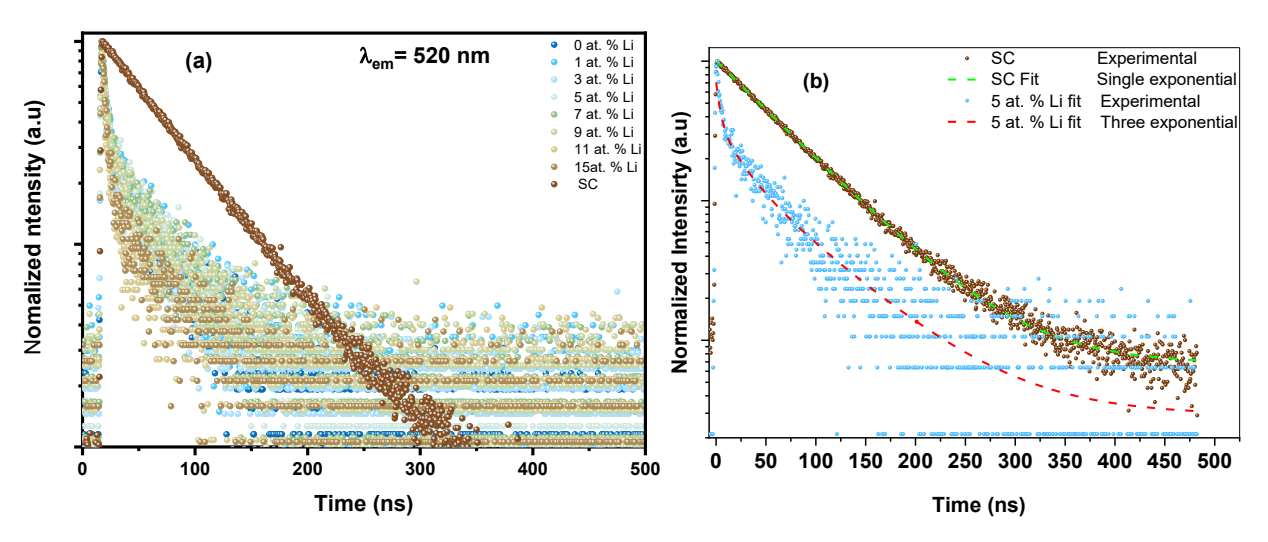


**Figure III.14 (a)** PL decay curves of LuAG: 0.5% Ce<sup>3+</sup>co-doped by Li<sup>+</sup> powders as well as that of SC with Li<sup>+</sup> content, **(b)** Monoexponential and three exponential fits for the emission decay curves of LuAG: Ce<sup>3+</sup> SC and LuAG: Ce<sup>3+</sup>, 5 at. % Li<sup>+</sup> powder respectively [1].

The presence of fast decay components in some garnets has been variously attributed. Kucera et al [147] explained the 3 ns fast component in GdYAG:Ce<sup>3+</sup> as being caused by parasitic energy transfer from the 5d<sub>1</sub> level of Ce<sup>3+</sup> to defect states or impurity ions. Similarly, in Ce<sup>3+</sup>-doped LuAG epitaxial films, the fast components are related to the non-radiative energy transfer between Ce<sup>3+</sup> ions and defects [148]. In this study, the third

decay component ( $\tau_3$ ) presented in **Table III.6** agrees with the decay of the conventional Ce<sup>3+</sup> emission in the LuAG host material. The observed decay times are consistent with values in the literature for Ce-doped aluminum garnets. For example, a decay time of 63 ns has been reported for LuAG:Ce<sup>3+</sup> single crystals (SC) [149], 50 ns for single crystal films (SCF) [150], and 59 ns for LuAG:Ce<sup>3+</sup> powders [151].

**Figure III.15a** shows the dependence of the decay time of  $Ce^{3+}$  emission  $(\tau_3)$  in LuAG as a function of Li<sup>+</sup> content. Compared to SC, LuAG: 0.5% Ce<sup>3+</sup> powders co-doped with different concentrations of Li<sup>+</sup> show distinct behavior as a function of Li<sup>+</sup> content. For low concentration (0-5 at. %), the lifetime increases, reaching a maximum at 5 at.%. This behavior suggests a reduction in the probability of a non-radiative transition, probably due to the presence of Li<sup>+</sup>. This behavior suggests a decrease in non-radiative transition probabilities, probably due to a reduction in extinction defects at the nano crystallite surface as a result of improved crystallinity at lower Li+ contents. At higher concentrations (5-15 at. %), the lifetime decreased. This reduction can be attributed to deteriorating crystallization and changes in the local environment of Ce<sup>3+</sup> ions, resulting in the formation of surface defects. These defects can increase non-radiative relaxation pathways, reducing PL lifetime. In nanomaterials, the increase in specific surface area also tends to contribution to shorter Ce<sup>3+</sup> lifetimes compared to single crystals, as previously reported [152]. These findings highlight the complicated interplay between Li<sup>+</sup> concentration, defect densities and the surface effects, that collectively affect the photoluminescence decay dynamic in LuAG:Ce<sup>3+</sup> powders.

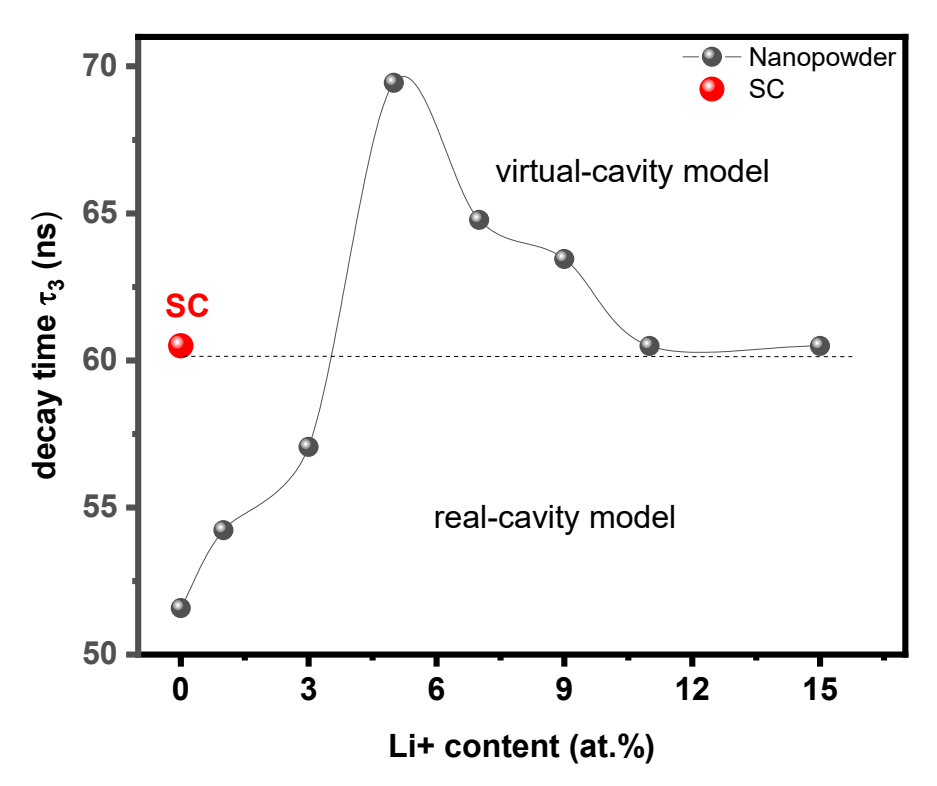


**Figure III.15a** variation of the experimental Ce<sup>3+</sup> decay time ( $\tau_{exp} = \tau_3$ ) against Li<sup>+</sup> content as well as of SC [1].

**Table III.6** Summary of the radiative decay parameters for Ce<sup>3+</sup> in LuAG: Ce<sup>3+</sup>, Li<sup>+</sup>nanophosphors and single crystal (SC) [1].

Li+	$Ce^{3+}$	0 at. %	1 at. %	3 at. %	5 at. %	7 at. %	9 at. %	11 at.	15 at.	SC
content	free							%	%	
$\tau_1$ (ns)		1.72	2.44	2.41	3.76	2.81	2.42	1.50	1.15	
$\tau_2(ns)$		6.97	15.58	10.74	20.49	12.85	10.17	6.49	6.49	
$\tau_3$ (ns)	30*	51.58	54.23	57.06	69.44	64.78	63.45	60.49	60.49	61.37
$\chi_{RC}$		2.64	2.78	2.93				3.09	3.09	
Xvc					5.18	5.60	5.70			
$\langle 5d r 4f \rangle$		0.0487	0.0463	0.0440	0.0300	0,0298	0,0299	0.0416	0.0416	
	0.025*									
$n_{eff}$		$1.65_{\text{RC}}$	$1.70_{\scriptscriptstyle RC}$	$1.76_{\scriptscriptstyle RC}$	$1.77_{\text{\tiny VC}}$	$1.81_{\text{\tiny VC}}$	$1.82_{\text{\tiny VC}}$	$1.82_{\hbox{\tiny RC}}$	$1.82_{\scriptscriptstyle RC}$	1.84
Filling factor x		0.773	0.833	0.904	0.916	0.964	0.976	0.976	0.976	1

\*ref:[57]

The variations in decay time values as reported in the literature are mainly attributed to microstructural differences between nano-garnet powders, single crystals and single crystal films, as well as differences in Ce3+ content. Indeed, for LuAG:Ce3+ co-doped with different content of Li<sup>+</sup>, from 0 to 5 at. % the lifetime increases and from 5 to 15 at. % decreases with a maximum at 5 at % content. This may indicate a decrease in nonradiative transition probabilities due to the decrease in quencher defects on the grain boundaries between the crystallite's domains, caused by low Li<sup>+</sup> content. For high Li<sup>+</sup> concentrations (greater than 5 at. %), crystallization deterioration with the change in Ce<sup>3+</sup> ion surroundings may generate surface defects that can be a trigger non-radiative relaxation, and generally, a shorter lifetime can reflect Ce<sup>3+</sup> luminescence on the surface. Furthermore, due to the increased specific surface area of LuAG nanomaterials, the PL lifetime of Ce<sup>3+</sup> was shorter than that of the ideal SC crystal. These defects act as nonradiative relaxation centers, reducing the lifetime of the photoluminescence. In generally, shorter lifetimes reflect Ce<sup>3+</sup> luminescence occurring at or close to the surface of nano crystallites. In additional, the increase in the specific surface area of LuAG nanomaterials compared to single crystals contributes to a reduction in the lifetime of Ce<sup>3+</sup> photoluminescence. These observations underline the interaction between Li<sup>+</sup> concentration, defect density and microstructural differences, all of which play a critical role in the determination of the decay dynamics of LuAG:Ce<sup>3+</sup> materials [152].

In light of the photoluminescence results, the potential of LuAG:Ce,Li powders as scintillators has been investigated further. This study focuses on the understanding of the effect of Li<sup>+</sup> codoping on scintillation properties, including thermally stimulated luminescence (TSL), radioluminescence (RL) and decay under pulsed X-ray excitation. These properties are essential for evaluating material performance in practical scintillation applications. Particular attention is focused on the role of lithium codoping in defect formation mechanisms and its impact on scintillation efficiency. By investigating how Li<sup>+</sup> affects defect creation and stabilization, as well as its influence on energy transfer processes, this study aims to better understand the interaction between codoping, structural modifications and scintillation performance in LuAG:Ce materials.

## Local-field effect on Ce<sup>3+</sup> spontaneous radiative emission

Furthermore, for the powders, previous works have reported that the radiative decay process strongly depends on both the size and shape of the particles besides the effective

refractive index ( $n_{eff}$ ) [151-154]. In fact, since the nanocrystallites (NCs) occupy only a small fraction of the total volume, the effective refractive  $n_{eff}$  index considers these particles surrounded by the medium with refractive index  $n_{med}$ . One may evaluate an effective index of refraction[155]:

$$n_{eff}(x) = x n_{bulk} + (1-x) n_{med}$$
 (5)

Here x presents the "filling factor" showing what fraction of space is occupied by the nanocrystallites (volume fraction = volume of NCs/volume of medium). For nanocrystallites, *n* is consequently replaced by  $n_{eff}(x)$ . It is important to note that the use of  $n_{eff}$  is valid only when the average size of the particles is much smaller than the wavelength of light, which is true in this study [155], [156]. It is well known that the spontaneous emission lifetime of emitter centers can be changed by modifying the surrounding dielectric [157], making them different from the vacuum, and the determination of the nanomaterial optical properties remains an issue. From this perspective, different theoretical models have been developed to predict the dependence of the lifetimes and the refractive index, especially for Eu<sup>3+</sup> and Ce<sup>3+</sup> rare earth ions. However, differences in radiative lifetime trends as a function of refractive index depend on the chosen model, which varies according to the circumstances [18]. In fact, all models and experimental studies are based on the fact that the only contribution to the spontaneous radiative lifetime comes from the electric dipole moment. This dipole moment's strength does not change when the surrounding medium varies [52]. The spontaneous radiative emission rate  $\Gamma_{ij}$  of electric dipole transition from an initial state i to a final state *f* can be expressed as [72]:

$$\Gamma_{if} = \frac{64\pi^4}{3h} \chi v_{if}^3 \left| \vec{\mu}_{if} \right|^2 \tag{6}$$

Where  $\vec{\mu}_{if}$  is the electric dipole moment  $-e \ \vec{r}_{if}$  between the initial state i to a final state f,  $v_{if}$  is the emission wave number and  $\chi$  is an enhancement factor due to the dielectric medium, which equals  $n[(n^2+2)/3]^2$  for the virtual (VC)- and  $n[3n^2/(2n^2+1)]^2$  for the real-cavity (RC) models [78]. The lifetime of the state can be calculated as the inverse of the total emission rate as  $1/\Gamma_{if}$ . For Ce<sup>3+</sup> ion, the electric dipole allowed emission  $5d \to 4f$ , which the electric dipole moment is proportional to the radial integral  $\langle 5d|r|4f \rangle$ . The radiative lifetime of Ce<sup>3+</sup> ions in different host materials (different refractive indices) has been considered by Duan and Reid [92]. Furthermore, for Ce<sup>3+</sup> ions, as it is known that the splitting between  ${}^2F_{5/2}$  and  ${}^2F_{7/2}$  final even sublevels is much smaller than the average

energy difference between the lowest 5d (5d<sub>1</sub>) and 4f states, one can assume that the final states f have the same energy, i.e., the average wave number  $v_{if}$  in **equation 6**, which leads to the total spontaneous emission rate being independent of the wave function of the initial 5d state, and can be written as [92]:

$$(1/\tau_r)_{VC,RC} = 4.34 \times 10^{-4} |\langle 5d|r|4f \rangle|^2 (\chi)_{VC,RC} \bar{\nu}^3$$
(7)

With the following rough assumptions, the radial integral  $\langle 5d|r|4f \rangle$  is considered constant for both LuAG as SC (bulk) and nanomaterial. Also, the measured lifetime  $\tau_{exp}$  of Ce<sup>3+</sup> is considered as the radiative one  $\tau_r$ . One can estimate the refractive index for each sample as follows:

For virtual-cavity model:

$$\left(\frac{\tau_{SC}}{\tau_{nano}}\right)_{Exp} \times (n_{SC}^2 + 2)^2 \times n_{SC} = n_{nano}^5 + 4n_{nano}^3 + 4n_{nano}$$
 (8)

For real-cavity model:

$$\left(\frac{\tau_{SC}}{\tau_{nano}}\right)_{Exp} \times \frac{(2n_{SC}^2 + 1)^2}{n_{SC}^5} = \frac{1}{n_{nano}^5} + \frac{4}{n_{nano}^3} + \frac{4}{n_{nano}}$$
 (9)

Following the adequate model for each sample, using the solutions of **equations 8 and 9**, which are the effective refractive index ( $n_{eff} = n_{nano}$ ), one can calculate the filling factor. Considering that LuAG: Li<sup>+</sup>, Ce<sup>3+</sup>, powders are surrounded by the air, then  $n_{med} = n_{air} = 1$ . Using the data of the **table III.6** with the refractive index of LuAG (SC) as 1.84 [105] the effective refractive index ( $n_{eff}$ ) and the optical filling factor (x) of the LuAG: Li<sup>+</sup>, Ce<sup>3+</sup> powder are calculated and given in the **table III.6**. **In Figure III.15a**, we display the variation of the experimental Ce<sup>3+</sup> decay time ( $\tau_{exp} = \tau_3$ ) against Li<sup>+</sup> content as well as of SC. One can see that depending on Li<sup>+</sup> content, there are two regions compared to that of SC. From 0 to 3 at. % presents  $\tau_{exp}$  smaller than that of SC and from 5 to 15 at. % is higher than that of SC. So that the values of x and  $n_{eff}$  have physical meaning (x < 1 and  $n_{eff} < n_{SC} = 1.84$ ), the real-cavity model (RC) is applied to the first region, from 0 to 3 at. % and virtual-cavity model (VC) to the second region from 5 et 15 at%. Furthermore, one can calculate  $\langle 5d|r|4f \rangle$ . From the measured lifetime  $\tau_{exp}$  and emission wavelength  $\lambda$  (520 nm) as [92]:

$$|\langle 5d|r|4f\rangle|_{exp} = \left[\frac{1}{4.34 \times 10^{-4} \times (\tau_{exp})(\chi_{VC,RC}) \times \bar{\nu}^{3}}\right]^{1/2}$$
 (10)

In **Figure III.15b**, we show the variation of the effective refractive index ( $n_{eff}$ ) as well as PL emission intensity against Li<sup>+</sup> content. We can roughly observe that PL intensity evolves oppositely to that of the effective refractive index, which can relate to the light extraction [143].

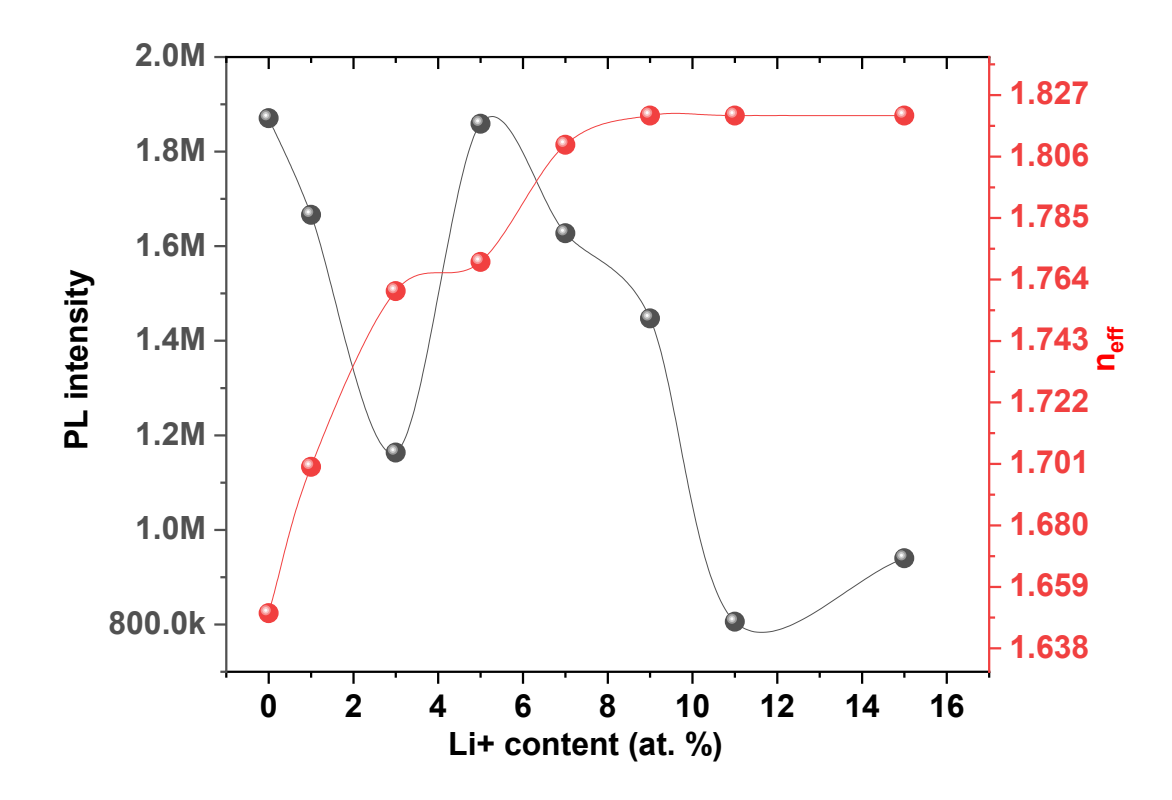


**Figure III.15b** variation of the effective refractive index  $(n_{eff})$  and the PL emission intensity against Li<sup>+</sup> content.

#### III.1.5. Radioluminescence

#### III.1.5.1 Radioluminescence steady state

**Figure III.16** shows the radioluminescence (RL) spectra of LuAG:Ce, Li+ powders with different lithium concentrations from 0 to 15 at. %, compared with LuAG:Ce single crystal (SC) and BGO scintillator powder. The previous figure shows the visual appearance of the synthesized powders under UV irradiation and standard lighting conditions, highlighting their response to photoluminescence. The presence of active luminescent centers is highlighted by photoluminescence emission under UV light, however scintillation performance under ionizing radiation is not directly correlated with photoluminescence emission. Thus, the RL spectra remain the primary reference for evaluating scintillation efficiency. The spectra show each sample's RL amplitude as a function of energy (in photons/eV and photons/nm). The addition of Li<sup>+</sup> notably impacts both the intensity and its spectral form of the RL emission. In particular, specific concentrations of Li<sup>+</sup> lead to increased amplitudes of peak compared to the SC and BGO references. Here, the emission peak near 2.5 eV corresponds to the 5d-4f transitions characteristic of Ce<sup>3+</sup> ions in the LuAG host matrix. Such improved luminescence efficiency is probably related to effective charge compensation and to the reduction in defect-related quenching routes made possible by Li<sup>+</sup> coding. Furthermore, RL spectra disclose distinct patterns associated probably with Pr<sup>3+</sup> contamination. The presence of a peak at 700 nm suggests an incoherent distribution of Pr<sup>3+</sup> in the samples. This uncontrolled variation in Pr<sup>3+</sup> content may introduce further spectral contributions which influence overall emission, justifying further analysis to decouple its impact from the Li<sup>+</sup> codoping mechanism.

The integrated RL amplitudes as summarized in the plot, reveal a non-linear relationship with Li<sup>+</sup> concentration. A clear dip is observed before the RL output increases, reaching maximum values at 7% and 15% Li<sup>+</sup>. These compositions display the brightest luminescence, with RL output comparable to that of SC and BGO, showing a significant improvement in their scintillation properties.

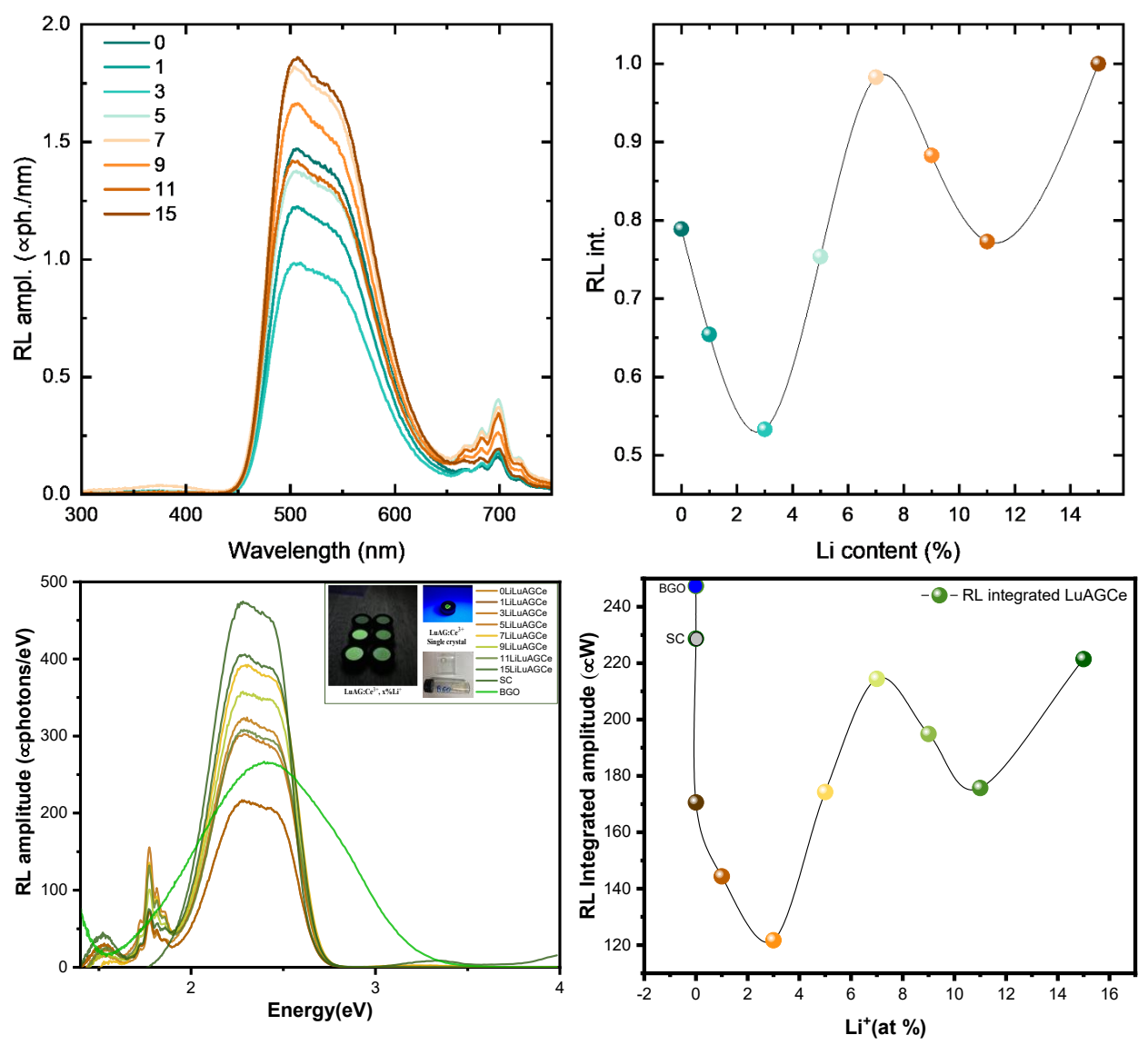


**Figure III.16** Radioluminescence spectra of LuAG: 0.5 at. % Ce<sup>3+</sup> codoped by different content of Li<sup>+</sup> powders, single crystal (SC) and BGO (left). Variation of intensities with Li<sup>+</sup> co-doping concentrations (right).

# III.1.5.2 Time resolved pulsed radioluminescence

**Figure III.17** presents the radioluminescence (RL) decay curves under pulsed X-ray excitation for LuAG:Ce<sup>3+</sup> powders codoped with different Li<sup>+</sup> contents (1, 3, 5, 7, 9, 11, and 15 at.%) alongside the LuAG:Ce<sup>3+</sup> single crystal (SC) used as reference. The aim of these measurements was to study the effect of Li<sup>+</sup> codoping on scintillation decay behavior.

The decay curves clearly show that no matter what the Li<sup>+</sup> concentration, all LuAG:Ce<sup>3+</sup>,Li<sup>+</sup> powders show faster scintillation decay than the single crystal (SC), this indicates that

the sol-gel synthesized powders contribute to more efficient charge transfer processes and reduced trapping, which accelerates light emission. In addition, no sign of slow components (afterglow) is detected in the measured time window, underlining the purity and efficiency of energy transfer in the synthesized LuAG:Ce<sup>3+</sup> powders.

While minor variations in decay time are observed between different levels of Li<sup>+</sup> doping, their impact is relatively minimal compared to the overall improvement in decay rate over SC. This suggests that Li<sup>+</sup> co-doping systematically improves the scintillation properties of LuAG:Ce<sup>3+</sup> powders by affecting the local surroundings of Ce<sup>3+</sup> ions and improving charge compensation.

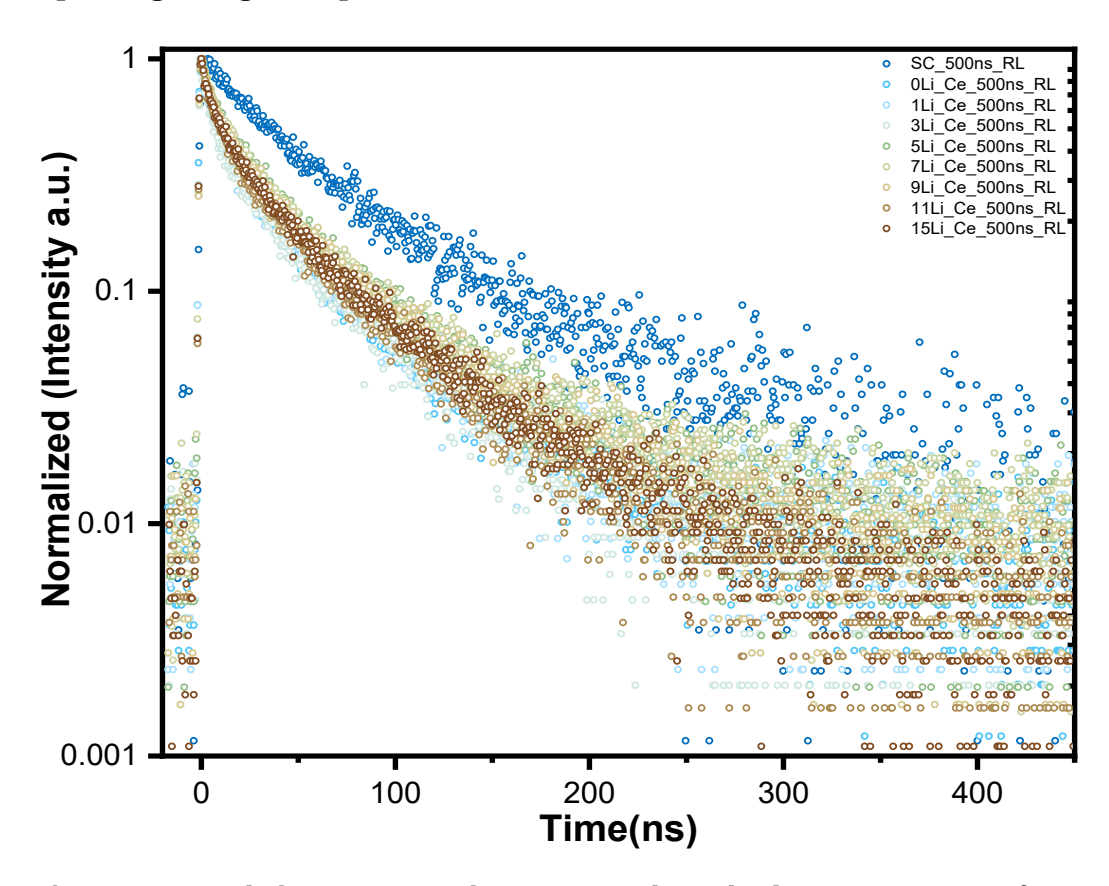


**Figure III.17** Radioluminescence decay time under pulsed X-ray excitation of LuAG:Ce<sup>3+</sup>, x at. % Li<sup>+</sup> powders and LuAG:Ce<sup>3+</sup> single crystal.

These findings confirm that Li<sup>+</sup> co-doped LuAG:Ce<sup>3+</sup> powders maintain high luminescence efficiency and offer faster scintillation decay, making them promising candidates for advanced scintillation applications.

## III.1.6. Thermally Stimulated Luminescence TSL

In this section we investigate the thermally stimulated luminescence (TSL) properties of LuAG:Ce<sup>3+</sup> powders co-doped with Li<sup>+</sup> under a variety of excitation conditions. TSL measurements provide an insight into the traps depth distribution, charge carriers and defect states dynamics in the materials. Two different types of TSL experiments have been carried out:

### III.1.6.1 TSL above room temperature

**Figure III.18** shows TSL glow curves above room temperature under X-ray excitation for LuAG:Ce<sup>3+</sup> powders co-doped with different Li<sup>+</sup> concentrations (1,2,3,5,7,9,11 and 15 at. %), showing a clear dependence of the glow curves on the Li<sup>+</sup> content, with variations in intensity and peak position with temperature.

The TSL peaks appear within a temperature range of approximately 300 K to 550 K. Notable variations in the intensity and position of these luminescence peaks are observed which result from the thermal release of charge carriers that are trapped in the material and then recombine at the Ce<sup>3+</sup> luminescence centers, resulting in characteristic light emissions. Hence, that process is a key indicator of how efficiently a material can store and release energy. However, the TSL intensity is proportional both to the trap concentration and to the efficiency of the luminescent centers. To try to take this into account and to separate these two contributions, we divided the TSL intensity be the one observe in RL. The outcome is a value which is more directly related the traps concentration only. As the Li<sup>+</sup> is introduced into the LuAG: Ce<sup>3+</sup> matrix, this significantly modifies the intensity of the TSL peaks but not their position. This suggests that these high temperature peaks are associated to intrinsic defects which are present regardless of Li co-doping. Li, however, can affect the probability of formation of this point defect and, consequently, their concentration. For instance, samples codoped with 7% at. % of Li<sup>+</sup> show a pronounced increase in TSL intensity which suggests that the concentration of these traps is increasing and that charge trapping is becoming more significant. This however seem to have no detrimental effect on the scintillation efficiency considering that the RL intensity is nevertheless high compared to the other samples. Also, for higher concentrations of Li<sup>+</sup>, the glow curve shape is not significantly altered, only its intensity is in fact affected.

The figure on the right shows integrated TSL intensity as a function of Li<sup>+</sup> content, normalized to RL intensity. It is interesting to note that a non-linear trend is observed, reflecting variations in charge trapping density as Li<sup>+</sup> content varies. In the context of TSL, a greater signal generally indicates a higher charge trapping density. However, it's important to note that for scintillation purposes, a weaker SLI signal is actually more favorable, as it involves fewer charge traps. In this study, TSL intensity is greatest at 7% Li<sup>+</sup> concentration, indicating the highest traps density at this level. Even with the increase in traps, radioluminescence (RL) performance remains high, which suggests that the presence of these additional traps does not significantly affect scintillation efficiency.

These results highlight that while Li<sup>+</sup> co-doping influences the formation of charge traps, it does not necessarily degrade the scintillation response. LuAG:Ce<sup>3+</sup>'s ability to maintain good RL output, even at higher trap densities, demonstrates its robust energy transfer and reduced non-radiative losses. These attributes means that LuAG:Ce<sup>3+</sup> co-doped with Li<sup>+</sup> can tolerate increased trapping without compromising its scintillation properties, which makes it attractive for certain applications where charge storage and efficient light emission are both required.

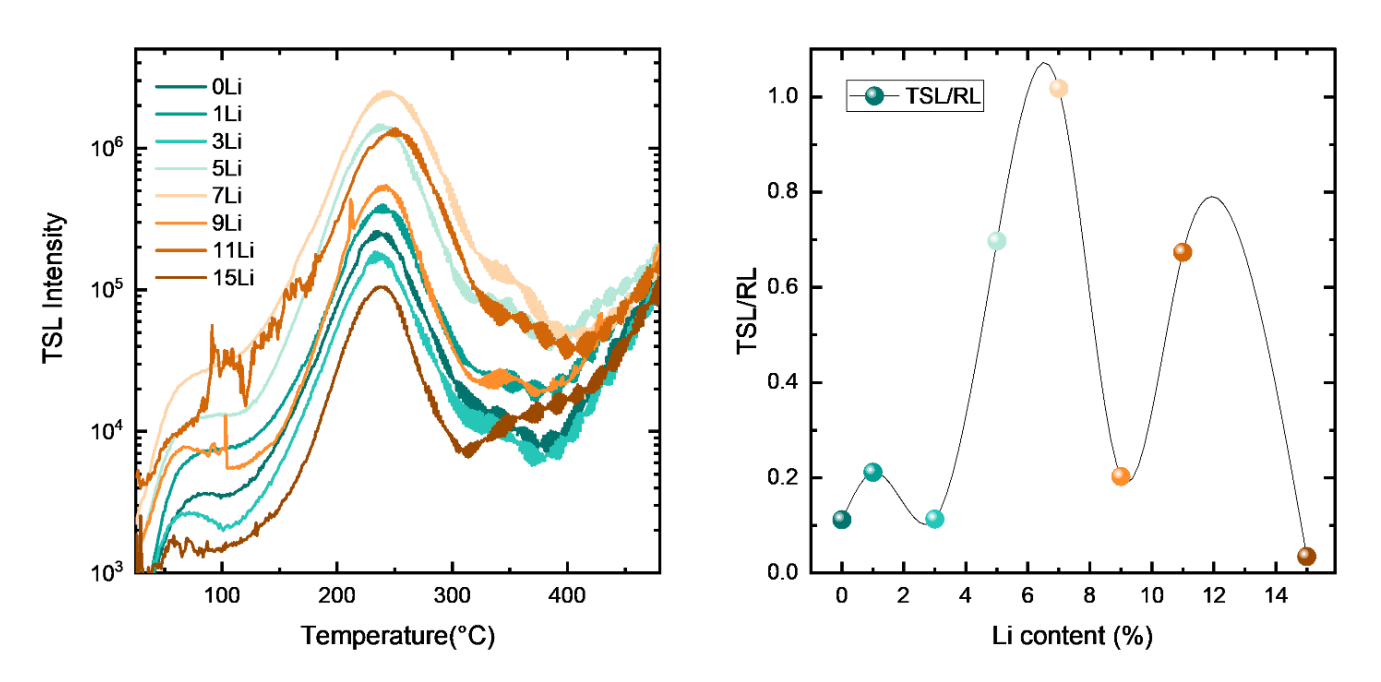


**Figure III.18** TSL above room temperature (X-ray excitation) of LuAG:Ce<sup>3+</sup>, x at. % Li<sup>+</sup> powders codoped with different content of Li<sup>+</sup>.

These results illuminate the crucial role of Li<sup>+</sup> codoping in optimizing trapping behavior in LuAG:Ce<sup>3+</sup> powders. In contrast to the usual combination of higher TSL intensity with improved performance, for scintillator applications the ideal case is in fact a lower TSL signal, provided that the radioluminescence (RL) efficiency remains high. Indeed, TSL traps, while useful for dosimetric applications, can act as competitive centers for charge capture, ultimately reducing light output during scintillation, particularly for TSL peaks that appear above room temperature (RT).

An important feature of the LuAG:Ce³+,Li⁺ powders studied is their combined high RL efficiency and relatively low TSL intensity in the range from 10 K to 320 K. These properties both minimize slow scintillation components and maximize the efficiency of light output, thus underlining their potential for high-performance radiation detection. While all materials necessarily display some level of trapping, the ability of these powders to maintain high luminescence with minimal trapping interference is a distinctive advantage for scintillation-based applications.

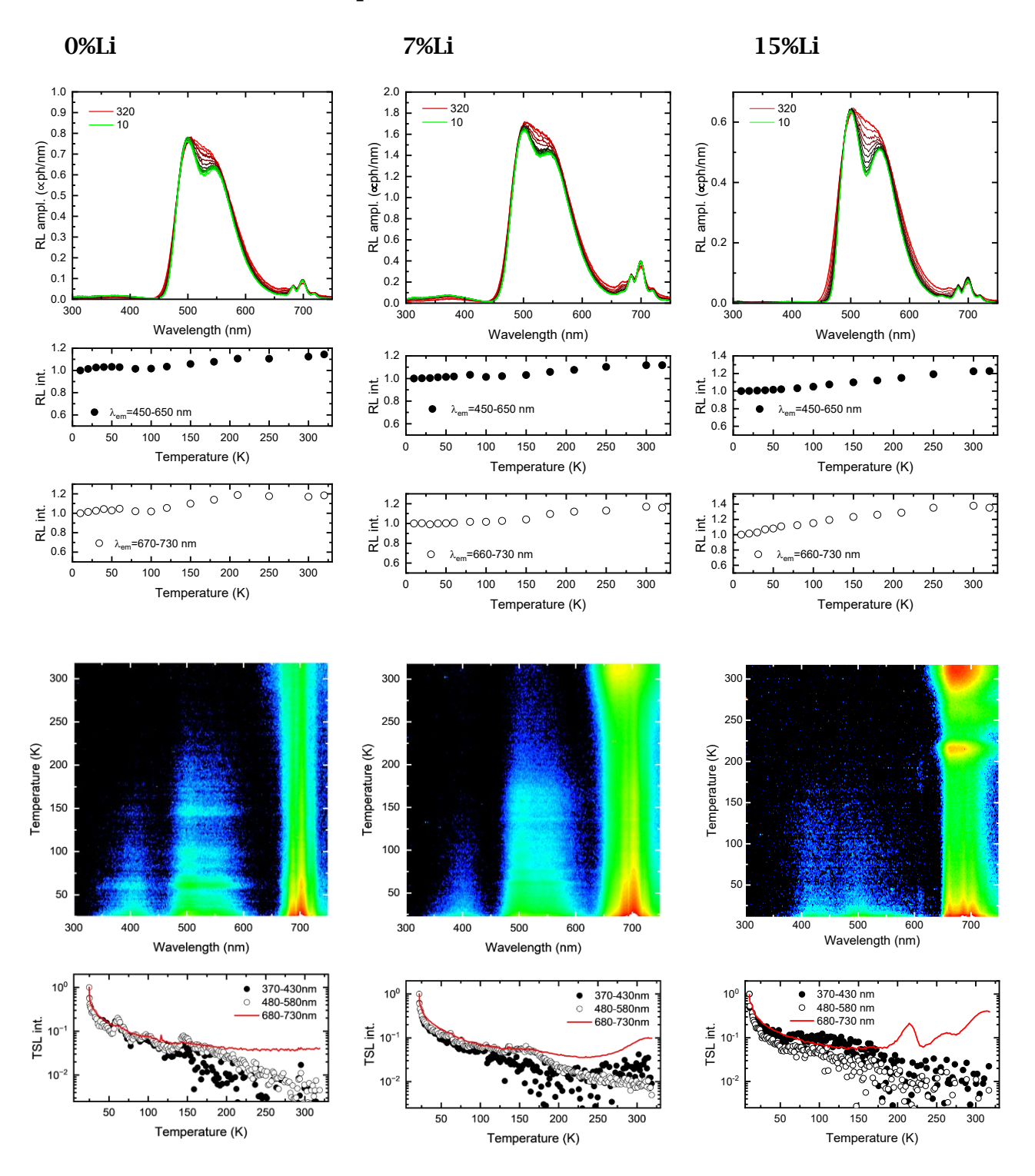
## III.1.6.2 TSL Measurements at low temperature

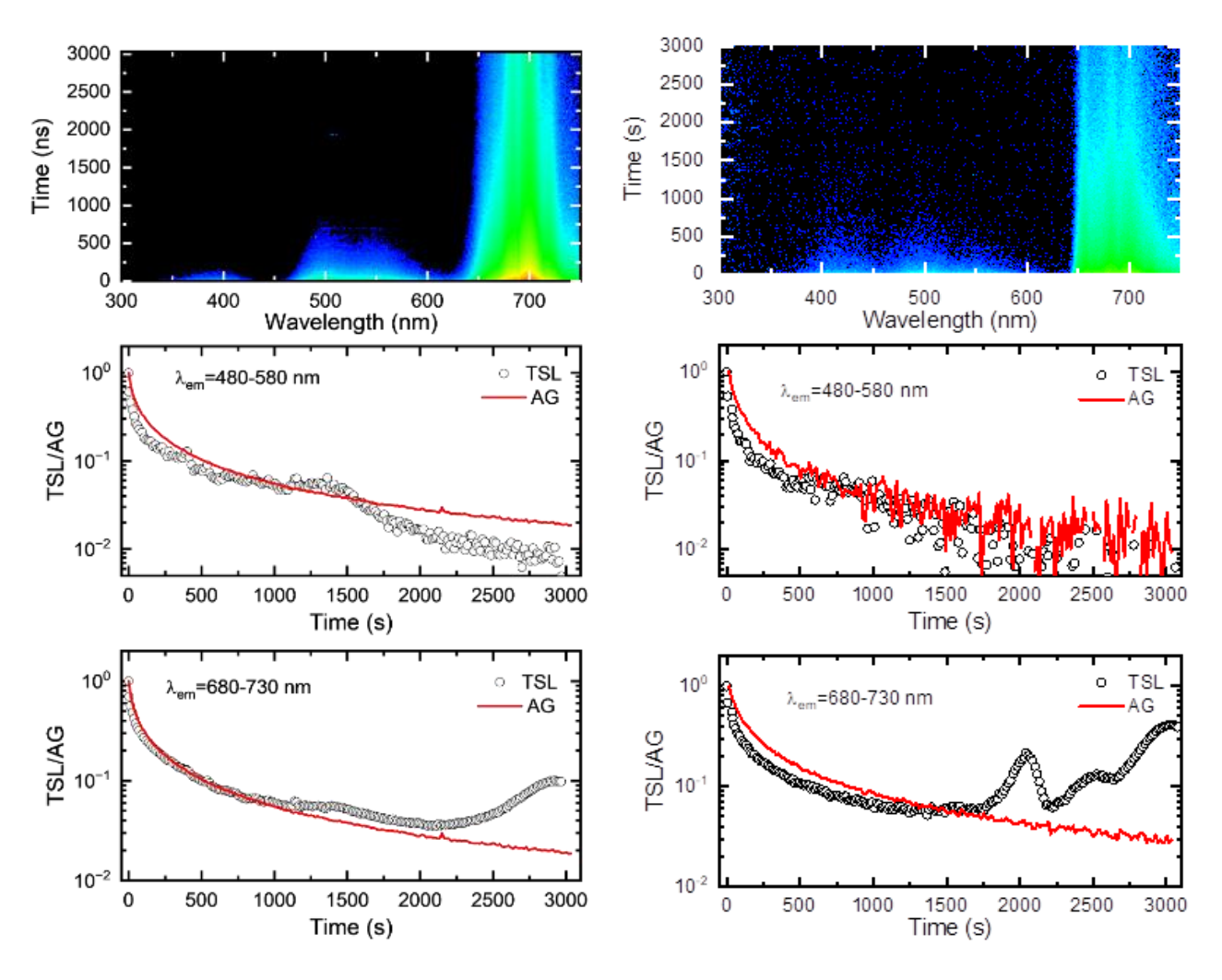
The thermally stimulated luminescence (TSL) measurements of LuAG: $Ce^{3+}$  codoped with 0%, 7%, and 15% Li<sup>+</sup> reveal critical insights into the role of lithium codoping at low temperatures (10 K to 320 K).

The TSL glow curves for these samples indicate the absence of - TSL peaks associated with Ce<sup>3+</sup> emission within the investigated temperature range. This absence underscores a minimal presence of electron trapping states associated and highlights a reduction in charge carrier losses due to non-radiative processes, as a consequence, the energy deposited by the ionizing radiation is more efficiently used for fast scintillation improving overall performance.

Two of the compositions tested, the 7 at. % and 15 at. % Li<sup>+</sup> co-doped powders are notable for their remarkable scintillation properties. They provide bright luminescence with no significant thermal quenching of Ce<sup>3+</sup> emission from 10 K to 320 K, with virtually no temperature dependence apart from an expected progressive emission bands broadening. As a result of this remarkable thermal stability, consistent scintillation efficiency is maintained even under varying thermal conditions, which makes them suitable for applications requiring robust thermal performance.

#### Measurements at low temperature on LuAG:Ce

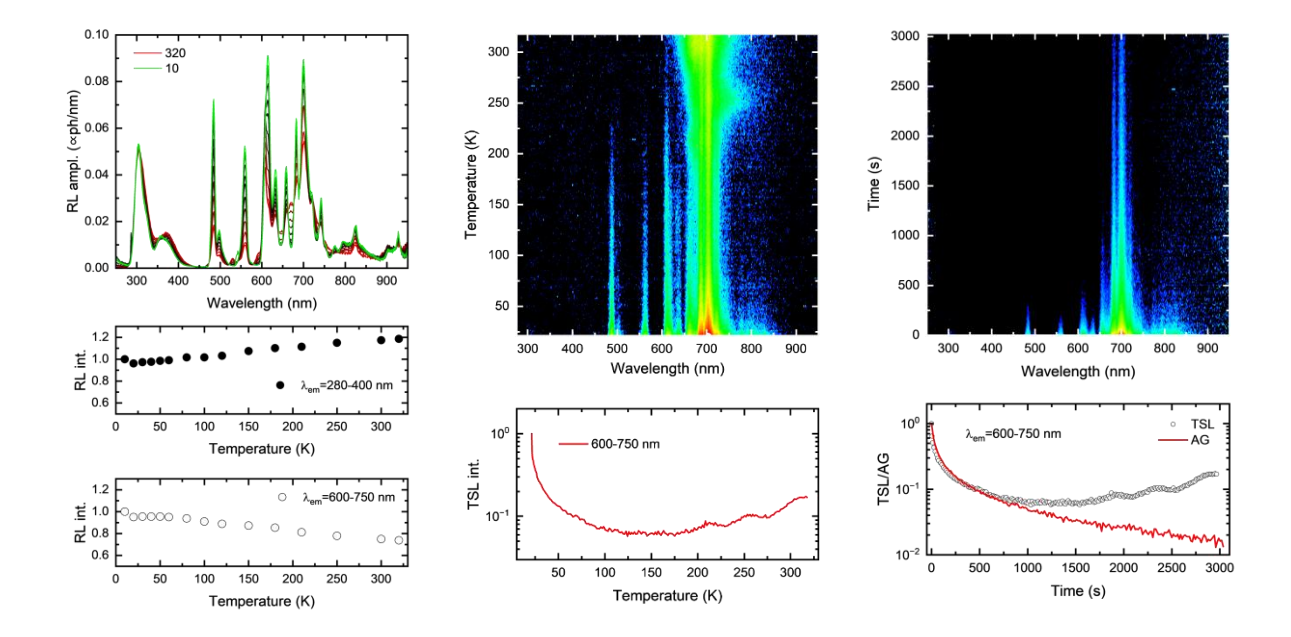




The presence of the emission at 700 nm which intensifies with  $Li^{+}$  concentration because its more intense at 7 at. %, it can be related to Praseodymium emission so the presence of  $Pr^{3+}$  in  $Ce^{3+}$  emission as impurity,  $LuAG:Pr^{3+}$  codoped with 15%  $Li^{+}$  was studied at low temperatures (10 K to 320 K) to investigate potential contributions from  $Pr^{3+}$  ions to thermally stimulated luminescence (TSL). These measurements revealed the presence of a distinct emission within the investigated temperature range, suggesting that  $Pr^{3+}$  ions may be actively involved in trapping and releasing charge carriers in the codoped samples.

#### Measurements at low temperature on LuAG:Pr

#### 15%Li



#### Conclusion

In the present chapter, all LuAG powder materials codoped with Ce<sup>3+</sup> and with varying concentration of Li<sup>+</sup>, Na<sup>+</sup> and K<sup>+</sup> ions have been successfully synthesized using a simple sol gel method. Detailed attention was focused on the effects of Li<sup>+</sup> codoping due to its significant impact on the structural, luminescence and scintillation properties of LuAG:Ce scintillating powder.

The influence of Li<sup>+</sup> codoping on the structural, morphological, and photoluminescence properties of LuAG:Ce was systematically investigated. Structural analysis revealed that the average crystallite size decreases with increasing Li<sup>+</sup> content, ranging from 66 nm (Lifree) to 47 nm for the highest Li<sup>+</sup> doping. DFT calculations showed that Li<sup>+</sup> preferentially occupies  $Al^{3+}$  (24d) sites in the LuAG:Ce matrix. EDS analysis confirmed that the sample with 5 at. % Li<sup>+</sup> exhibits an atomic percentage ratio close to the stoichiometric composition of Lu<sub>3</sub>Al<sub>5</sub>O<sub>12</sub>.

Codoping LuAG:Ce³+ with Na⁺ or K⁺ induces greater lattice expansion and strain compared to Li⁺, which directly relates to their larger ionic radii. While crystallite size peaks at low codoping concentrations for all three ions, Na⁺ and K⁺ produce significantly larger crystallite maxima. These results highlight the dual role of ionic radius and codopant concentration in structure progression. By strategically tuning these parameters, garnet-based scintillators can be optimised to improve performance in structural properties.

Photoluminescence (PL) studies demonstrated that all samples exhibit intense, broad emission bands in the 450–650 nm range, attributed to the  $5d_1 \rightarrow 4f$  transition of  $Ce^{3+}$  in the LuAG host. Interestingly, Li<sup>+</sup> codoping was found to reduce PL intensity compared to both Li-free LuAG:Ce powders and single crystals, with the 5 at.% Li<sup>+</sup> sample displaying the highest PL intensity among the codoped samples. Regarding electron-vibrational coupling, all LuAG:Ce<sup>3+</sup> powders, whether Li<sup>+</sup>-free or codoped, exhibit intermediate coupling (2 < S < 3) compared to the strong coupling (S = 5.99) in single crystals, with no clear trend dependent on Li<sup>+</sup> content. The spontaneous emission lifetime of Ce<sup>3+</sup> was found to follow the real-cavity model (RC) for low Li<sup>+</sup> content (0–3 at. %) and the virtual-cavity model (VC) for higher Li<sup>+</sup> content (5–15 at. %).

Radioluminescence (RL) studies revealed that among the tested compositions, the 7% and 15% Li<sup>+</sup> codoped samples exhibited the brightest luminescence. These results highlight that while Li<sup>+</sup> co-doping influences the formation of charge traps, it does not necessarily degrade the scintillation response. LuAG:Ce<sup>3+</sup>'s ability to maintain good RL output, even at higher trap densities, demonstrates its robust energy transfer and reduced non-radiative losses. These attributes means that LuAG:Ce<sup>3+</sup> co-doped with Li<sup>+</sup> can tolerate increased trapping without compromising its scintillation properties, which makes it attractive for certain applications where charge storage and efficient light emission are both required.

Scintillation decay analysis of LuAG:Ce³+,Li⁺ materials provides clear evidence that solgel synthesized powders exhibit faster decay times than single crystals (SC), irrespective of Li⁺ concentration. Such improvement is due to the ability of the sol-gel method to promote efficient charge transfer and reduce carrier trapping which accelerates light emission. In particular, the absence of afterglow components in the decay curves supports the purity of energy transfer and the minimal recombination associated with powder defects. These findings clearly underline the potential of the sol-gel technique for the development of high-performance scintillators with rapid response and suppressed afterglow.

Thermally Stimulated Luminescence (TSL) studies revealed crucial insights into the trap dynamics of the co-doped powders. In contrast to conventional scintillator behavior where higher TSL signals are often associated with enhanced performance, the LuAG:Ce³+,Li⁺ powders displayed lower TSL intensities across the 10 K to 320 K range, reflecting a reduced density of charge traps. This is particularly significant, as fewer charge traps minimize non-radiative pathways, thereby improving scintillation efficiency.

In summary, this study demonstrates that Li<sup>+</sup>, Na<sup>+</sup> and K<sup>+</sup> codoping in LuAG:Ce allowing precise control of structural, morphological and luminescence properties, offering a pathway to optimize garnet-based materials for advanced scintillation applications.

# Chapter IV

CODOPING EFFECTS ON LuAG:Pr3+

#### Introduction

Following the full study of codoping effects in LuAG:Ce³+ covered in Chapter III, the focus of this chapter is on LuAG:Pr³+, with the objective of exploring ways in which alkali metal ions (Li⁺, K⁺, and Na⁺) affect its structural, morphological and luminescent material properties. Although Ce³+-doped LuAG has been widely studied for its exceptional scintillation performance, Pr³+-doped LuAG provides its own unique advantages, in particularly faster emission decay and efficient radiative transitions, which are critical for high-resolution timing applications. However, the impact of codoping with alkali metals in LuAG:Pr³+ is still less explored offering the opportunity to address this gap and despite its potential.

This chapter's main objective is to investigate the effects of Li<sup>+</sup>, K<sup>+</sup>, and Na<sup>+</sup> codoping on LuAG:Pr<sup>3+</sup> scintillating powders, by concentrating on their impact on structural and morphological properties, photoluminescence and radioluminescence. Unlike the detailed analysis carried out for Ce<sup>3+</sup> codoping in Chapter III, this chapter presents a simplified but focused review while its aim is to compare the two doping centers Ce<sup>3+</sup> and Pr<sup>3+</sup> and to show how the different alkaline codopants are modulating the scintillation characteristics.

While the analysis in this chapter is less in-depth than that in Chapter III, it serves as a complementary exploration that adds to the understanding of the codoping of alkali metals in different luminescent centers. By placing the Pr³+ results together with those from Ce³+, this chapter aims to provide a clearer picture of the ways in which codoping strategy can be adjusted to optimize scintillation efficiency and time resolution in LuAG-based materials. These findings not only further contribute to the basic understanding of codoping effects, but also pave the way for future progress in fast-response scintillator applications.

# IV.1 Codoping effects of Li<sup>+</sup>, K<sup>+</sup>, and Na<sup>+</sup> on LuAG:1%Pr<sup>3+</sup> scintillating powders

# IV.1.1 structural analysis

**Figure IV.1** presents the XRD patterns of  $Lu_3Al_5O_{12}$ : 1 at. %  $Pr^{3+}$  with various concentrations of alkali metal cation of Lithium LuAG:1 at. %  $Pr^{3+}$ , x at. %  $Li^+$  (x =1, 3, 5, 7, 9, 11 and 15 at. %) powders. It is apparent that all the diffraction peaks can be properly assigned the cubic phase (JCPDS no. 73–1368), with Ia3d as the space symmetry group. Similar to  $LuAG:Ce^{3+}$  in the previous chapter. **Table IV.1** presents the structural parameter values of the LuAG:1 at. %  $Pr^{3+}$  samples co-doped with various  $Li^+$  concentrations.

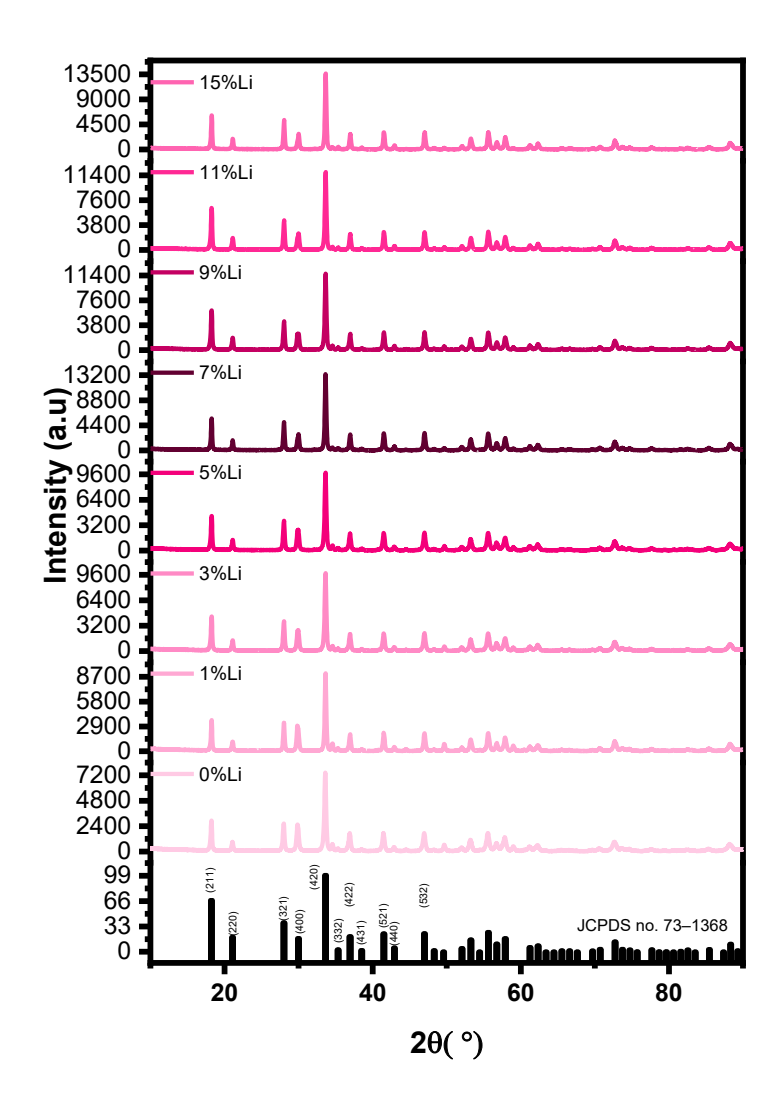


**Figure IV.1** XRD patterns of Lu<sub>3</sub>Al<sub>5</sub>O<sub>12</sub>: 1 at. % Pr <sup>+3</sup>, co-doped with different content of Li<sup>+</sup>.

(hkl)	2θ (°)	FWHM (°)	$\theta$ (rad)	FWHM (rad)	$\frac{\sin \theta}{\lambda}$	$\frac{\beta\cos\theta}{\lambda}$	Height [cts]
211	18.207	0.227	0.15888605	0.0039619	0.10244717	0.00253303	1805
321	27.964	0.243	0.24403194	0.00424115	0.15644821	0.0026648	1772
420	33.572	0.271	0.29297097	0.00472984	0.18699802	0.0029321	5142
422	36.860	0.324	0.32166418	0.00565487	0.20470595	0.00347375	1121
521	41.423	0.301	0.36148387	0.00525344	0.22899824	0.00318179	1210
532	46.911	0.354	0.4093757	0.00617847	0.25773069	0.00367002	1177

$$A = 11.9060 \text{ Å} (1368-073-01)$$

The strain  $\epsilon = 0.0074$ 

Equation 
$$y = a + b*x$$
, Intercept = 0.00167 
$$a = \frac{0.98}{D_{W-H}} = 0.00167$$
 
$$D_{W-H} = 586 \text{ Å}$$
 
$$D_{W-H} = 58.6 \text{ nm}$$

Same steps were followed for the other Li<sup>+</sup> content

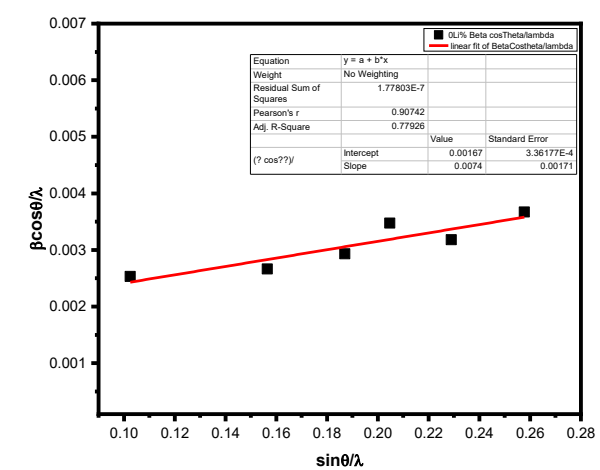


**Table IV.1** Structural parameters for samples of LuAG: 1%Pr<sup>3+</sup> co-doped with different content of Li<sup>+</sup>

%Li	a (Å)	ε (%)	$\mathbf{D}_{\text{W-H}}$ (nm)	$\mathbf{D}_{\mathrm{Sch}}$ (nm)
0	11.926	0.0074±0.00171	58.6	31
1	11.920	$0.00348 \pm 0.00115$	53.5	37
3	11.914	0.00247±6.77434E-4	45.1	35
5	11.921	0.00175±0.0023	42	31
7	11.918	0.00308±0.00175	33.3	38
9	11.916	5.90839E-4±6.55171E-4	41.3	36
11	11.916	6.3763E-4±5.44758E-4	42.9	37
15	11.915	0.00165±6.16373E-4	50.2	40

Supported by structural analysis of LuAG:Pr,Li, the present study explores the effects of  $K^+$  and  $Na^+$  co-doping on  $Lu_3Al_5O_{12}$ :1 at. %  $Pr^{3+}$ . XRD analysis patterns presented in **Figure IV.2** (LuAG:1 at. %  $Pr^{3+}$ , x at. %  $K^+$  (x =1, 3, 5, 7, 9, 11 and 15 at. %) and **Figure IV.3** (LuAG:1 at. %  $Pr^{3+}$ , x at. %  $Na^+$  (x =1, 3, 5, 7, 9, 11 and 15 at. %) of structural properties was investigated for codopant concentrations varying from 1 to 15 at. %, assuming the same conditions of synthesis and investigation. Further XRD patterns affirm the garnet's conservation of its cubic structure (JCPDS No. 73-1368) along with Ia3d symmetry, whatever the type or the codopant concentration.

 $K^{\scriptscriptstyle +}$ 

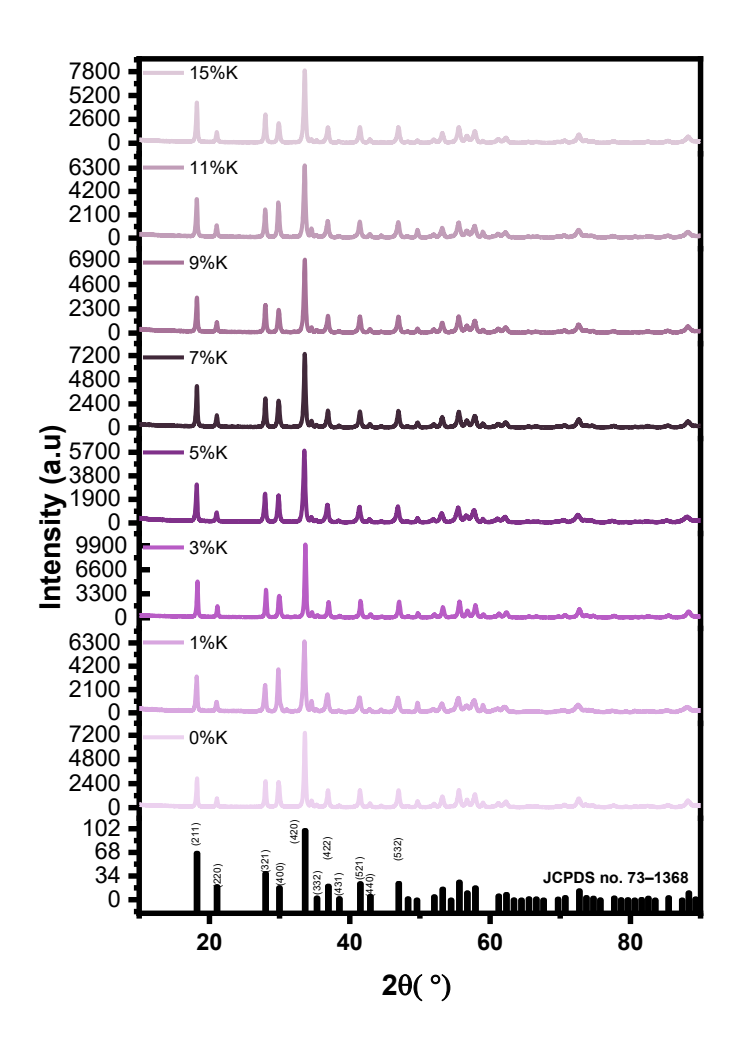


**Figure IV.2** XRD patterns of Lu<sub>3</sub>Al<sub>5</sub>O<sub>12</sub>: 1 at. % Pr <sup>+3</sup>, co-doped with different content of K<sup>+</sup>. **Table IV.2** Structural parameters for samples of LuAG: 1%Pr<sup>3+</sup> co-doped with different content of

%K	a (Å)	ε (%)	Dw-H (nm)	D <sub>Sch</sub> (nm)
0	11.926	$0.0074 \pm 0.00171$	58.6	31
1	11.950	$0.00728 \pm 0.00123$	151.1	45
3	11.915	$0.00256 \pm 5.38224$ E-4	106.1	65
5	11.940	$0.00565 \pm 4.68822$ E-4	122	48
7	11.929	$0.00204 \pm 5.86811E-4$	72	56
9	11.927	$0.00354 \pm 6.05629 E\text{-}4$	100.2	55
11	11.929	$0.00345 \pm 9.92442E-4$	91.5	52
15	11.929	$0.00375 \pm 8.08354 E\text{-}4$	98.4	53

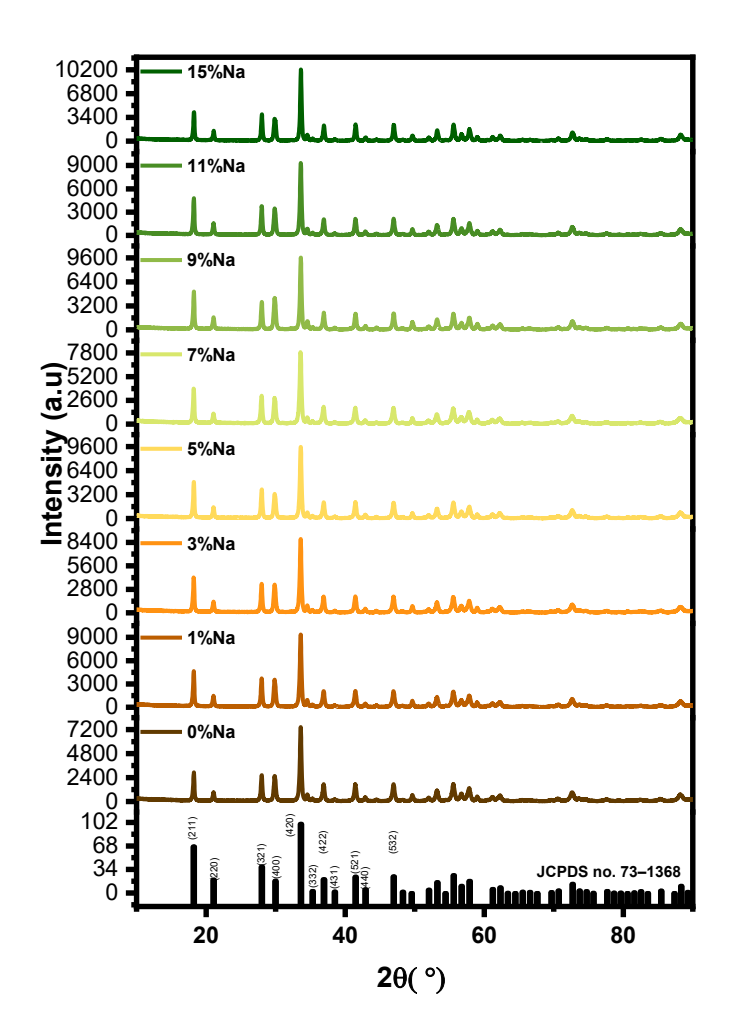


Figure IV.3 XRD patterns of  $Lu_3Al_5O_{12}$ : 1 at. % Pr $^{+3}$ , co-doped with different content of Na $^+$ . Table IV.3 Structural parameters for samples of LuAG:  $1\%Pr^{3+}$  co-doped with different content of Na $^+$ 

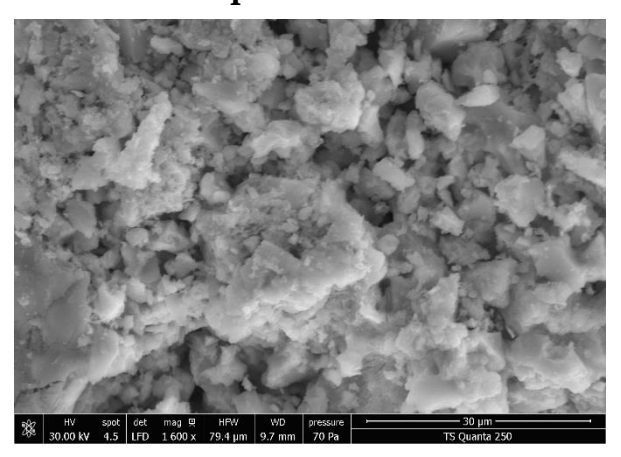
%Na	a (Å)	ε (%)	Dw-H (nm)	D <sub>Sch</sub> (nm)
0	11.926	$0.0074 \pm 0.00171$	58.6	31
1	11.925	$0.00255 \pm 7.43083$ E-4	102.2	61
3	11.926	$0.00307 \pm 6.4625$ E-4	101.4	59
5	11.924	$0.00337 \pm 6.87209$ E-4	111.9	60
7	11.924	$0.00436 \pm 8.25092$ E-4	97.0	55
9	11.923	$0.00218 \pm 9.10049$ E-4	114.2	64
11	11.923	$0.00264 \pm 2.44618E-4$	110.9	66
15	11.919	$0.00159 \pm 6.04737 E-4$	99.0	72

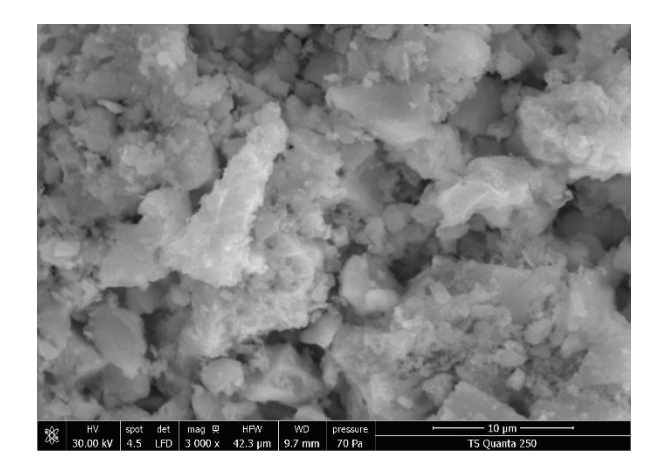
#### IV.1.2 Morphological analysis

Scanning electron microscopy (SEM) reveals codoping-induced significant morphological variations. Undoped LuAG:Pr³+ sample shows finer, more uniformly distributed sized particles. As it is codoped with Li⁺ (e.g. LuAGPr15Li), particle morphology changes to smoother, and the particle size increases as a result of grain coalescence induced by the presence of Li⁺. On the other hand, co-doping with either K⁺ or Na⁺ (e.g. LuAGPr5K and LuAGPr15Na) gives bigger, more aggregate particles, as observed in SEM images. The increase in particle size is coherent with the growth of the nanocrystalline domains detected in the XRD analysis.

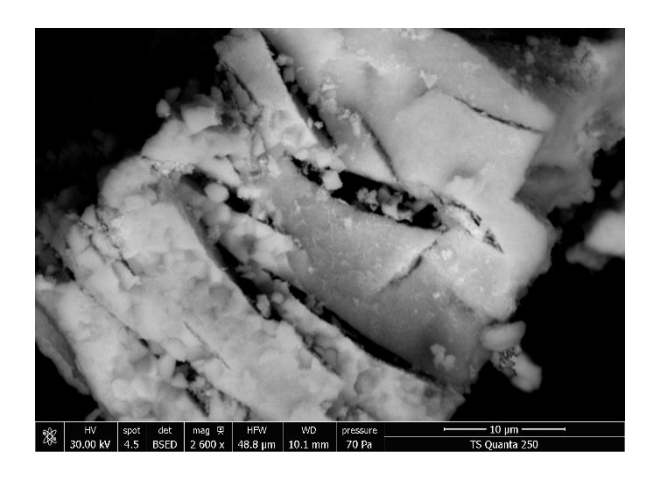
Microstructural changes such as these are crucial, since they can influence light scattering and the density of surface defects, which in turn impacts the material's optical and scintillation performance.

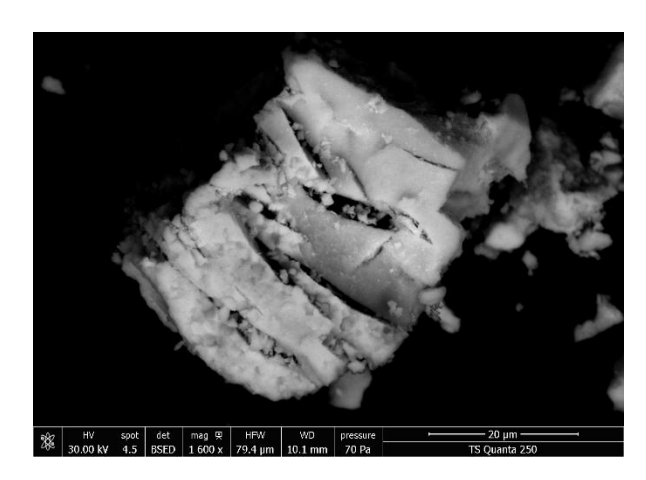
# LuAGPr undoped



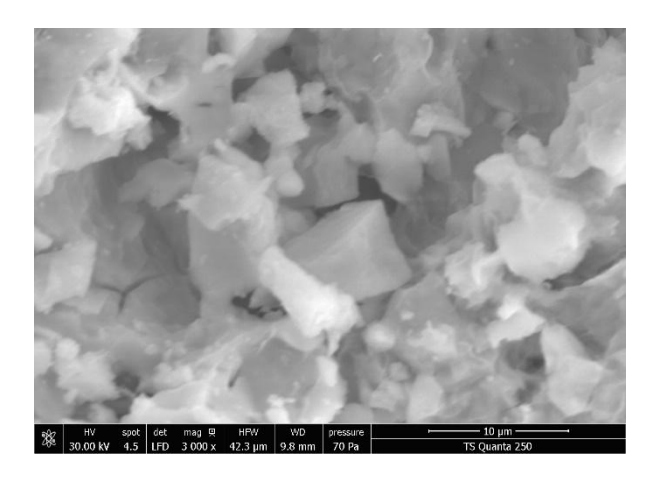


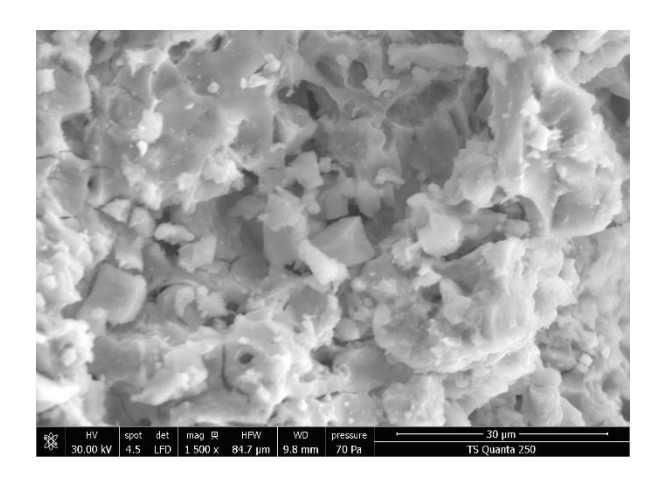
LuAGPr15Li



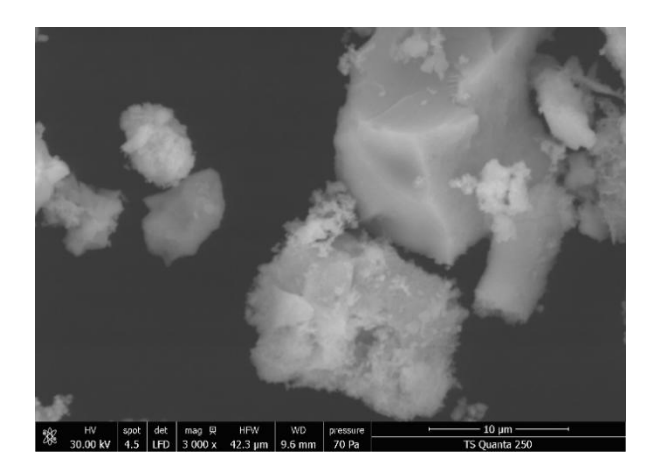


# LuAGPr5K





# LuAGPr15Na



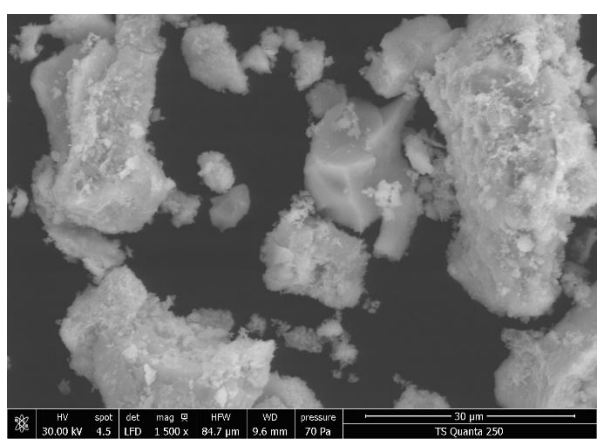


**Figure IV.4** SEM images of samples, namely LuAG:  $Pr^{3+}$  undoped; LuAG:  $Pr^{3+}$ , 15Li; LuAG:  $Pr^{3+}$ , 5K; LuAG:  $Pr^{3+}$ , 15Na.

#### IV.1.3 Photoluminescence study

#### IV.1.3.1 Photoluminescence steady state

Steady-state photoluminescence (PL) spectra of LuAG:Pr³+ codoped powders show a dependence of emission behavior on alkali ions. PL properties of LuAG:1%Pr³+ scintillating powders, codoped with alkali ions (Li⁺, K⁺, Na⁺), has been systematically studied for understanding the mutual interplay between codopant-induced structural modifications and emission efficiency. Below is a structured analysis of the main results and study mechanisms:

The Figures show room temperature emission and excitation spectra of LuAG powders doped with 1% Pr³+ ions and co-doped with different concentrations (x%) of Li⁺, Na⁺, and K⁺ ions, respectively. One can see that Pr³+- doped LuAG shows characteristic emission transitions due to its 4f electronic configuration. B. Kahouadji et al. reported the observed transitions. In the case of excitation, the following transitions dominate:

- ${}^{3}P_{0} \rightarrow {}^{3}H_{4}$ : ~490 nm (blue emission)
- ${}^{3}P_{0} \rightarrow {}^{3}H_{5}$ : ~530 nm (green emission)
- ${}^{3}P_{0} \rightarrow {}^{3}F_{2}$ : ~610 nm (red emission)

Moreover, regardless of the temperature, all samples exhibit nearly identical excitation features. Specifically, the excitation spectra recorded while monitoring emission at 603 nm can be divided into two distinct regions: the first, in the UV range, corresponds to inter-configurational  $4f^25d^0 \rightarrow 4f^15d^1$  transitions, while the second involves intraconfigurational  $4f^2 \rightarrow 4f^2$  transitions. **Figure IV.5** presents a schematic energy diagram of  $Pr^{3+}$  ion with indication of the photoluminescence (PL) excitation and emission transitions of these ions in the LuAG host. For photoluminescence emission spectra of our samples, all the spectra were measured at room temperature with 240 nm excitation wavelength, the emission bands observed at around 24000-36000 cm-¹ correspond to the transitions from the 5d excited state to the  $^3H_J$  ground-state levels of  $Pr^{3+}$  ions. Their spectral profiles show structured emission bands, which are characteristic of 5d  $\rightarrow$  4f transitions, indicated on the figures.

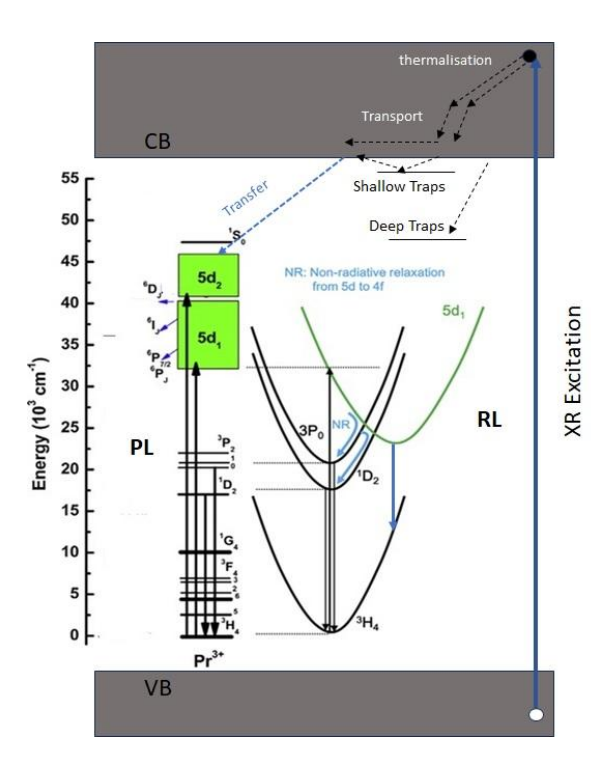


**Figure IV.5** Schematic energy diagram of Pr<sup>3+</sup> ion with indication of the absorption and emission transitions of these ions in the LuAG host.

#### In each series:

- · Li<sup>+</sup> codoping (**Figure IV.6**): Emission intensity initially increases with low Li<sup>+</sup> concentration (particularly at 1-5%), indicating an enhancement effect, possibly due to load compensation or network distortion improving energy transfer efficiency. However, at higher Li<sup>+</sup> concentrations (above 5%), a gradual decrease in intensity is observed, probably due to concentration quenching.
- · Na<sup>+</sup> codoping (**Figure IV.7**): A more significant increase in luminescence intensity is observed with increasing Na<sup>+</sup> content, with maximum emission observed at 1 and 11%. This suggests that Na<sup>+</sup> coding is effective in enhancing the emission efficiency of Pr<sup>3+</sup> ions. At very high concentrations (15%), a slight decrease suggests the appearance of quenching effects.
- ·  $K^+$  codoping (**Figure IV.8**): The emission intensity increases up to an optimum concentration of 5%, then decreases with the addition of  $K^+$ . The larger ionic radius of  $K^+$  compared to  $Li^+$  and  $Na^+$  can lead to greater distortion of the LuAG lattice, which can impact the local  $Pr^{3+}$  environment and have an impact on its radiative efficiency.

Overall, the results demonstrate that codoping with alkali ions significantly affects the photoluminescence performance of LuAG:Pr³+. An optimum doping concentration is observed for each ion (as illustrated in Figure IV.8), above which quenching effects reduce emission efficiency. Codopages at 1% Li⁺, 5% K⁺ and 1% Na⁺ show the highest emission intensities. However, these results need further interpretation and detailed exploration to understand the mechanisms involved. More detailed analysis would be useful to determine the impact of ionic interactions and structural modifications induced by codoping, allowing further optimization of the scintillating properties of this material.

# LuAG: 1%Pr3+, x% Li+

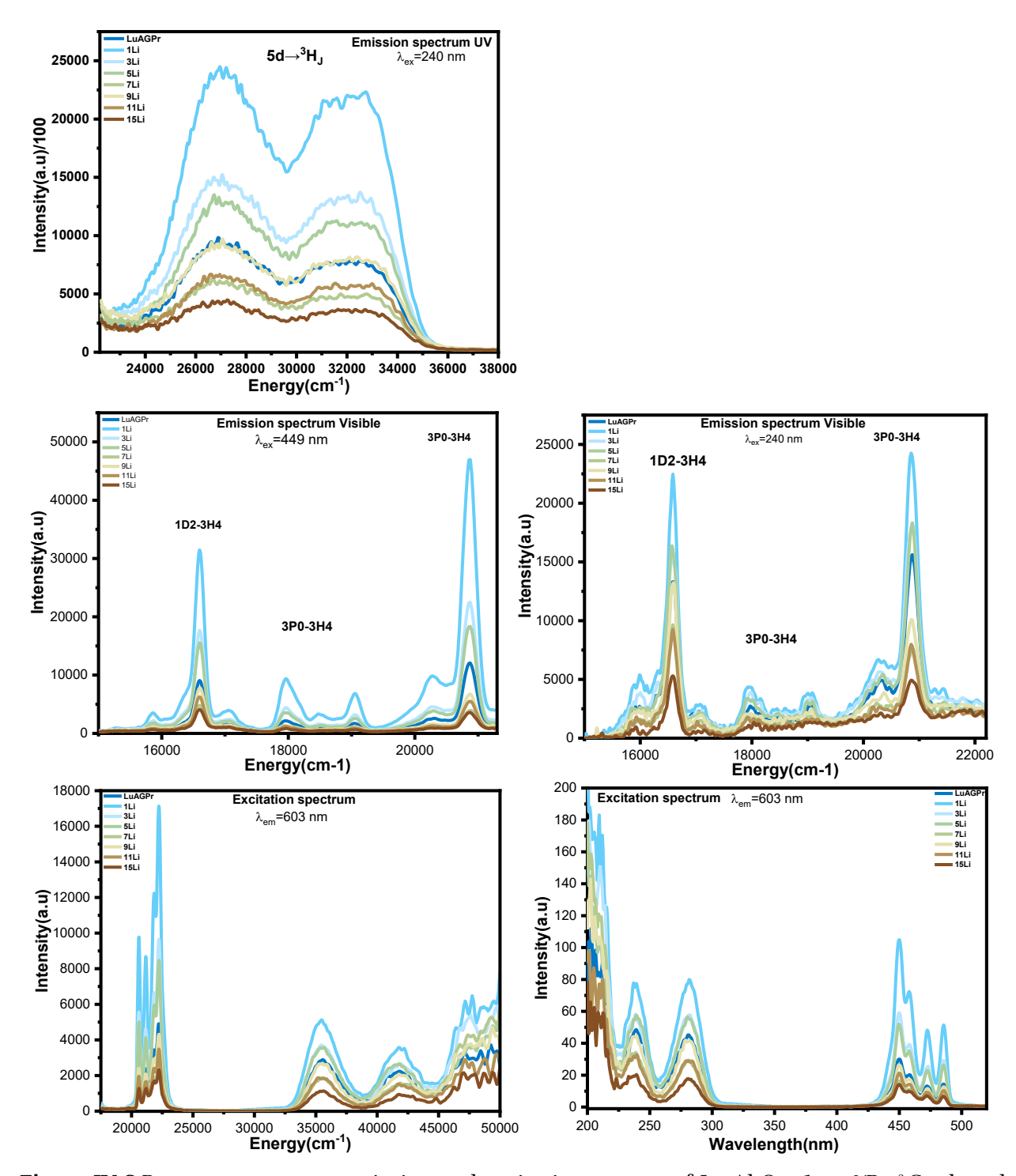


**Figure IV.6** Room temperature emission and excitation spectra of  $Lu_3Al_5O_{12}$ : 1 at. %Pr  $^{+3}$  Co-doped by different content of  $Li^+$  powders.

# LuAG: 1%Pr3+, x% Na+

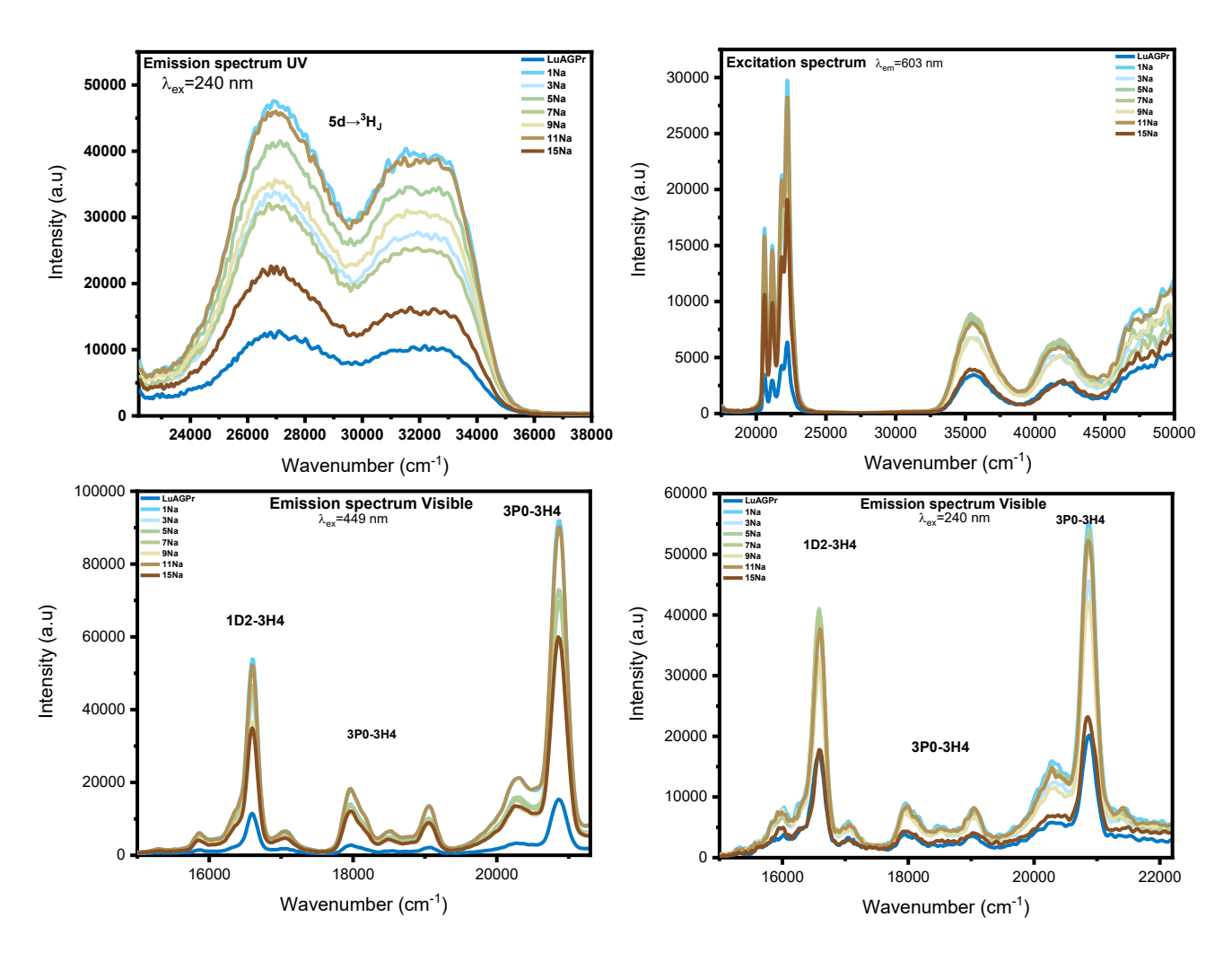


**Figure IV.7** Room temperature emission and excitation spectra of  $Lu_3Al_5O_{12}$ : 1 at. %Pr  $^{+3}$  Co-doped by different content of  $Na^+$  powders.

# LuAG: 1%Pr3+, x% K+

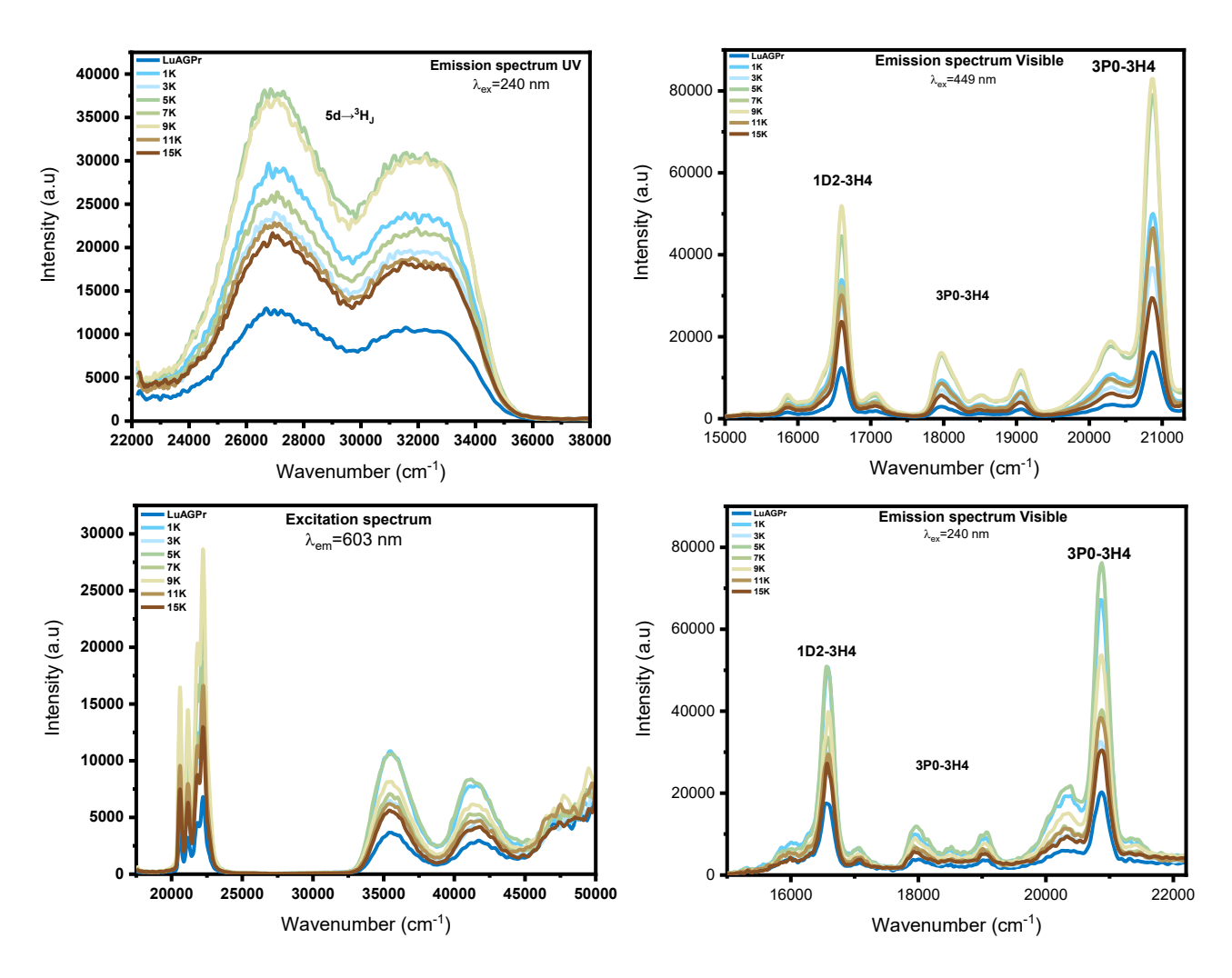


**Figure IV.8** Room temperature emission and excitation spectra of  $Lu_3Al_5O_{12}$ : 1 at. %Pr  $^{+3}$  Co-doped by different content of  $K^+$  powders.

# LuAG: 1%Pr<sup>3+</sup>, (0%, 1%Li<sup>+</sup>, 1%Na<sup>+</sup>, 5%K<sup>+</sup>)

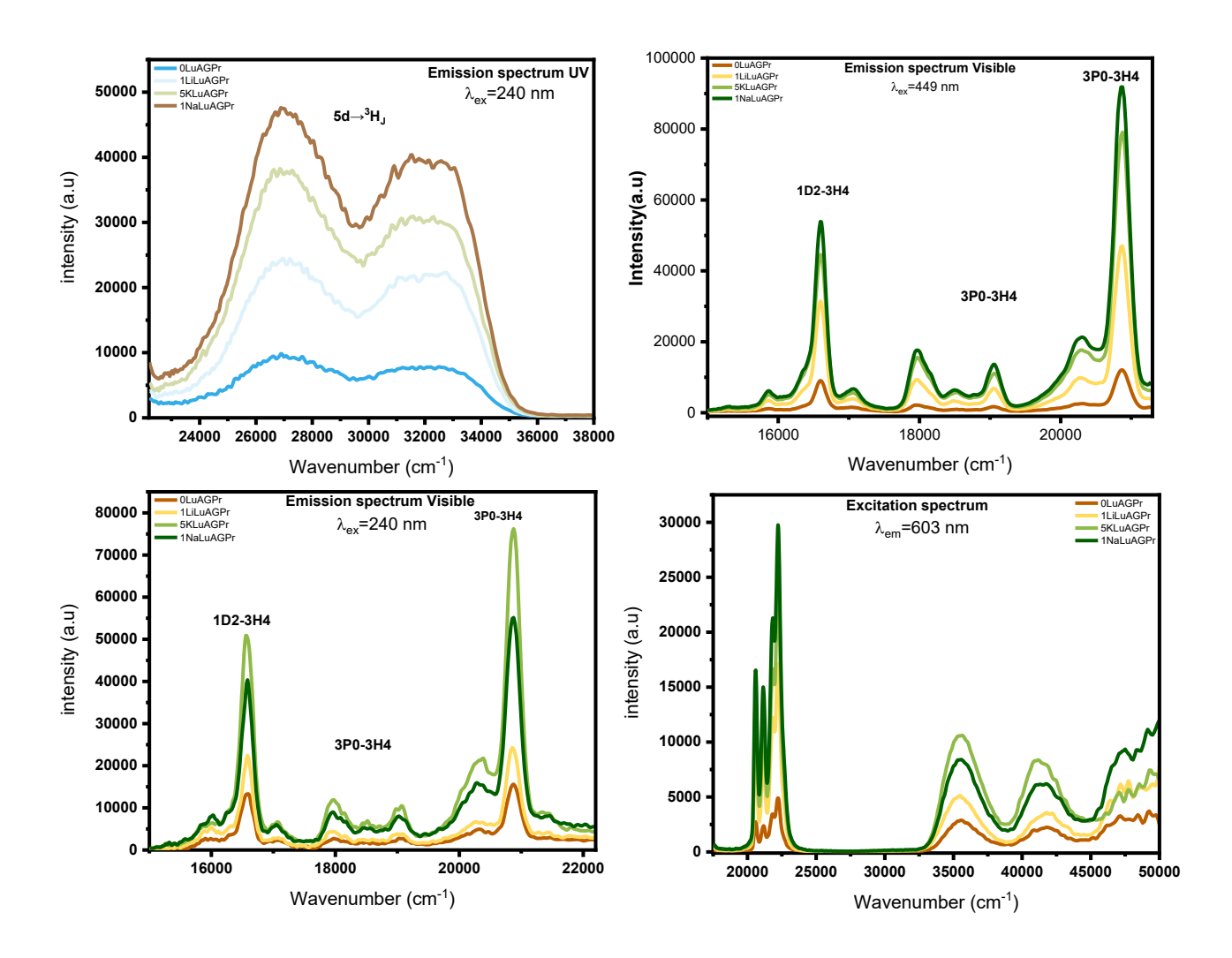


**Figure IV.9** Room temperature emission and excitation spectra of  $Lu_3Al_5O_{12}$ : 1 at. %Pr +3 Co-doped by (undoped, 1%Li+, 1%Na+, 5%K+) powders.

**Table IV.4** Structural parameters for samples of LuAG:  $1\%Pr^{3+}$  co-doped with different content of Li<sup>+</sup> / K<sup>+</sup> /Na<sup>+</sup>

%Li/K/Na	a (Å)	ε (%)	$\mathbf{D}_{\text{W-H}}$ (nm)	$\mathbf{D}_{\mathrm{Sch}}$ (nm)
0	11.926	$0.0074 \pm 0.00171$	58.6	31
1Li⁺	11.920	$0.00348 \pm 0.00115$	53.5	37
1Na⁺	11.925	$0.00255 \pm 7.43083E-4$	102.2	61
5K⁺	11.940	$0.00565 \pm 4.68822$ E-4	122	48

#### IV.1.4 Radioluminescence

#### IV.1.4.1 Radioluminescence steady state

The room temperature radioluminescence spectra of  $Lu_3Al_5O_{12}$  doped with 1%  $Pr^{3+}$  and co-doped with different  $Li^+$  concentrations are displayed in **Figure IV.9.** The visible spectral range's 4f-5d and 4f  $\rightarrow$  4f transitions are mainly responsible for the distinctive emission peaks of  $Pr^{3+}$  seen in the spectra.

Emission intensity is strongly affected by the concentration of Li<sup>+</sup> ions codoping. RL spectra show multiple emission bands, with the most prominent peaks appearing in the visible region. The intensity of these peaks varies systematically with Li<sup>+</sup> concentration with steady-state emission 1.5 times higher than undoped samples, indicating a clear connection between codoping content and radiative emission efficiency. Notably, the spectrum associated with the highest Li<sup>+</sup> content (1%Li) exhibits the highest emission, suggesting increased scintillation efficiency under X-ray excitation.

Concerning the variation of integrated RL amplitude for two distinct regions (Region 1 Energy from 1.18-2.75 eV and Region 2 from 2.75-4.50 eV) as a function of Li<sup>+</sup> concentration in Lu<sub>3</sub>Al<sub>5</sub>O<sub>12</sub>:Pr<sup>3+</sup> powders. The graph shows that the integrated amplitude whose reaches its maximum values at 7 at. % and 15 at. % Li<sup>+</sup> comparing to the LuAG: Pr undoped sample. Nevertheless, a deeper analysis based on the literature and the results of our experiments is needed in order to completely understand as well as clarify the basic processes controlling these enhancements. A deeper understanding of the optimum codoping for enhanced scintillation performance will result from this further work, and this will clarify the specific role of Li<sup>+</sup> in influencing the structural and luminescent properties in the LuAG:Pr<sup>3+</sup> matrix. In **Figure IV.5**, the radioluminescence (RL) emission transitions are also illustrated with different traps.

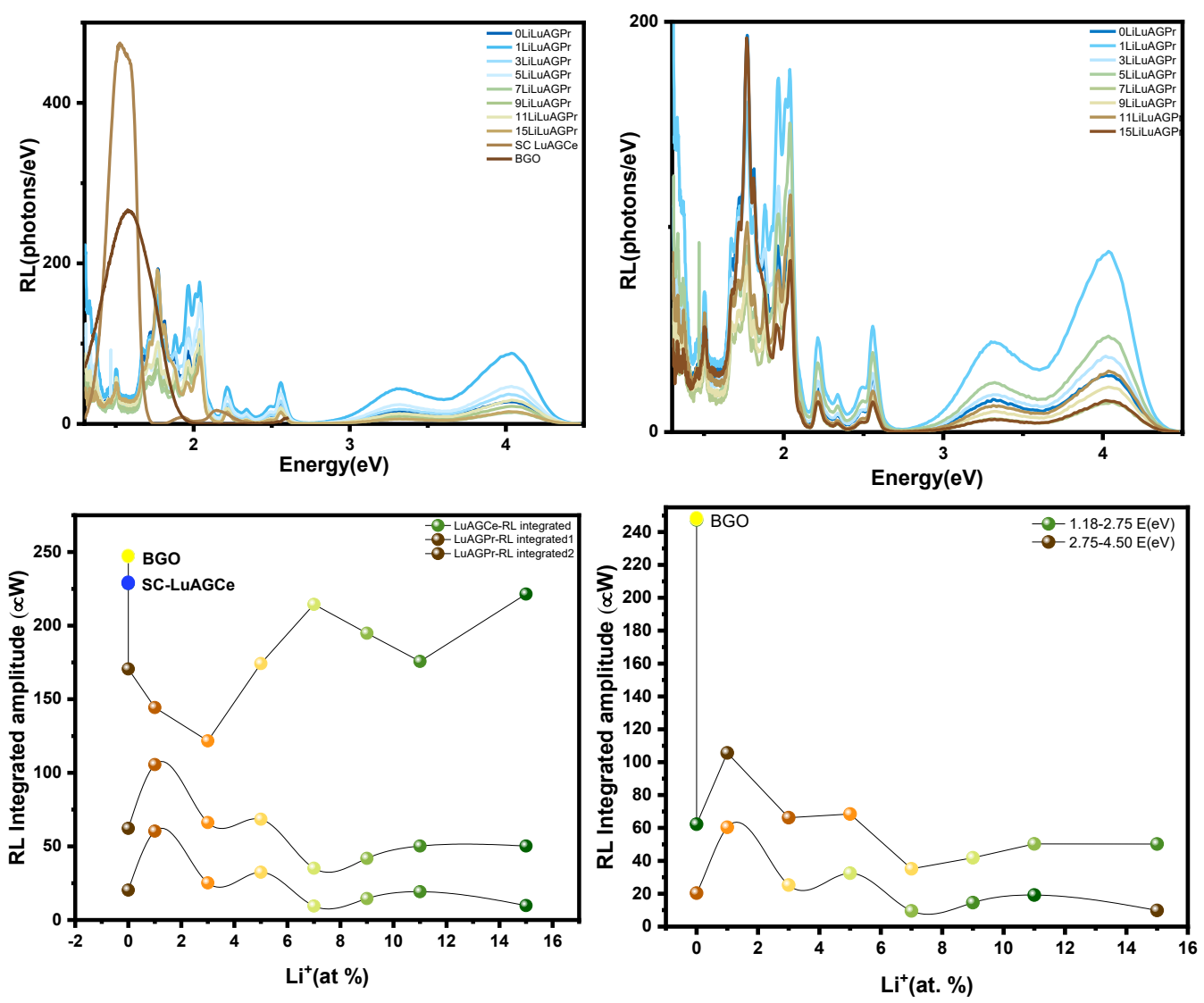


**Figure IV.10** Radioluminescence spectra of Lu<sub>3</sub>Al<sub>5</sub>O<sub>12</sub>: 1 at. %Pr <sup>+3</sup> codoped by different content of Li<sup>+</sup> powders and Variation of RL integrated amplitude.

#### IV.1.4.2 Time resolved Radioluminescence

Shown here is the radioluminescence (RL) decay of  $Lu_3Al_5O_{12}$ : $Pr^{3+}$  powders codoped with various  $Li^+$  concentrations (0-15 at. %), plotted on a semi-logarithmic scale. Across all samples there is an initial fast decay, characteristic of  $Pr^{3+}$  prompt  $5d \rightarrow 4f$  transitions, which is followed by a slower component indicating multi-exponential kinetics. Raising the  $Li^+$  concentration causes decrease in decay time to accelerate systematically.

The further development of fast and cost-effective scintillators, as achieved in this study, offers considerable promise for applications requiring high time resolution in radiation detection technologies. Optimized decay rates and low cost of materials production make them very competitive for scintillator technologies of the next generation.

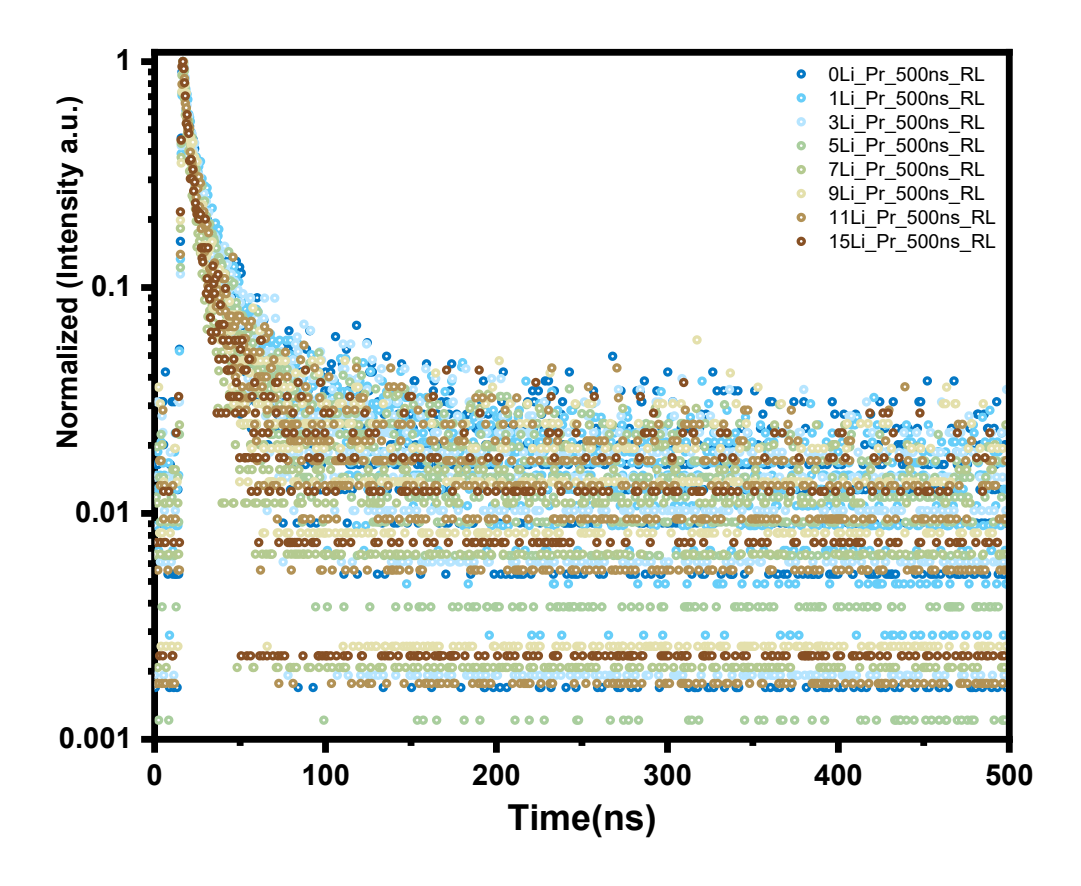


**Figure IV.11** Radioluminescence decay time under pulsed X-ray excitation of  $Lu_3Al_5O_{12}$ : 1 at. %  $Pr^{*3}$ , x at. %  $Li^*$  powders.

#### Conclusion

This chapter investigated how the structural, morphological, photoluminescence, and radioluminescence characteristics of LuAG:Pr³+ scintillating powders are affected by alkali metal ion codoping (Li⁺, K⁺, and Na⁺). The findings showed that Li⁺ codoping significantly increases photoluminescence and radioluminescence intensities, decreases structural strain, and improves crystallographic coherence, especially at the ideal concentrations of 1% for steady-state PL and 7–15% for RL. Li⁺ is a suitable codopant for fast scintillation applications. In contrast, the effects of K⁺ and Na⁺ codoping on emission intensity and decay characteristics differed due to the introduction of greater crystallite sizes and particle aggregation.

These results highlight the significance of choosing the right codopant for enhancing LuAG:Pr³+ scintillation performance and offer important new information on how alkali metal ions affect lattice stability, emission efficiency, and scintillation speed. To better understand the precise processes underlying these improvements, more interpretation based on experimental and literary studies would be helpful, especially for Li which shows exceptional promise for applications using low cost and efficient scintillators.

# GENERAL CONCLUSION

#### **General Conclusion**

The present PhD research has resulted in an extensive study of the synthesis, structural, morphological and optical properties of  $Lu_3Al_5O_{12}$  garnet (LuAG) materials doped with  $Ce^{3+}$  and  $Pr^{3+}$ , and co-doped with alkali metal ions (Li<sup>+</sup>, Na<sup>+</sup>, and K<sup>+</sup>). Through a systematic experimental approach combined with theoretical simulations, the work successfully proved the potential of these co-doped scintillating materials for enhancing luminescence performance and structural tunability. This study was motivated by the need for low-defect, high-performance scintillating materials, taking into account the limitations of traditional crystal growth methods, which are often costly and difficult to scale up. The sol-gel synthesis method adopted in this research provided an economical and versatile route to produce homogeneous LuAG-based powders with precise control of co-doping concentrations.

The thesis aimed to explore how codoping with Li<sup>+</sup>, Na<sup>+</sup>, and K<sup>+</sup> can significantly improve the structural and scintillation properties of LuAG:Ce<sup>3+</sup> and LuAG:Pr<sup>3+</sup>. While the effects of Ce<sup>3+</sup> and Pr<sup>3+</sup> doping in LuAG are well documented, the role of alkaline codopants remains relatively unexplored. This work has contributed to narrow this gap, providing new information on how Li<sup>+</sup>, Na<sup>+</sup> and K<sup>+</sup> codoping affects structural, morphological, luminescent and scintillation properties.

The first chapter introduces an extensive overview of scintillating materials, their mechanisms and applications, focusing on garnet-based scintillators such as LuAG. The importance of rare-earth doping, particularly with Ce³+ and Pr³+, has been established as a key route to improving scintillation efficiency. In addition, codoping with alkali metal ions has been identified as a promising strategy for optimizing luminescence properties, enhancing energy transfer and reducing non-radiative losses. The second chapter detailed the synthesis of LuAG:Ce³+ and LuAG:Pr³+ codoped with varying concentrations of Li⁺, Na⁺, and K⁺ using the sol-gel method. This cost-effective, scalable process enabled precise control of dopant concentrations and facilitated the formation of fine, homogeneous powders. Structural and morphological characterizations by XRD, SEM and EDS revealed well-defined crystal structures, while DFT simulations provided a better understanding of dopant site preferences, lattice modifications and co-doping-induced defect interactions. Optical characterization using PL, RL and TSL measurements showed the effects of codoping on scintillation performance, supporting the choice of alkali ions

as codopants to improve material properties. Chapter 3 focused on LuAG:Ce³+ codoped with Li⁺, Na⁺ and K⁺. Among these, Li⁺ proved to be the most effective codopant, significantly affecting structural, luminescence and scintillation properties. Li⁺ codoping was found to reduce crystallite size and increase photoluminescence intensity, particularly at optimum concentrations. Radioluminescence studies revealed that all Li⁺-codoped LuAG powders exhibit faster scintillation than single crystals without afterglow, while TSL analysis revealed reduced trap densities, further contributing to enhanced charge transport and high RL efficiency, making these materials promising for applications requiring fast response and minimal light output losses. The fourth chapter has extended the study to LuAG:Pr³+ codoped with the same alkali metal ions, revealing that Li⁺ also has a positive impact on PL and RL intensities while stabilizing the crystal structure. Optimum concentrations of Li⁺ improved emission efficiency and decay rate, demonstrating its suitability for fast scintillation applications. In contrast, Na⁺ and K⁺ had variable impacts on luminescence properties, mainly through lattice expansions and larger crystallite sizes, which are linked to their larger ionic radii.

The results of this research highlight the importance of defect control and codoping strategies in advancing scintillator technology. Reduced defect density, improved RL properties and controlled crystallite growth suggest that these materials could be promising candidates for the fabrication of transparent scintillating ceramics. Although beyond the scope of the present study, this aspect opens up new paths for future work focusing on the processing of low-defect ceramics, taking advantage of LuAG's cubic symmetry and resistance to charge trapping.

In conclusion, this work has demonstrated that codoping with alkali metals, in particular Li<sup>+</sup>, significantly improves the structural stability, luminescence efficiency and decay dynamics of LuAG-based scintillators. This is an important step towards the development of low-cost, high-performance scintillator materials for advanced applications in radiation detection, medical imaging and high-energy physics. Further exploration of transparent ceramics, along with the scalability of sol-gel synthesis for industrial applications, could boost the application of these materials in advanced optical technologies, opening up a promising future for next-generation scintillators.

#### References

- [1] Z. Akhrib, et al. "Lithium ion codoping effect on structural, morphological and photoluminescence spectroscopy of  $\text{Lu}_3\text{Al}_5\text{O}_{12}$ :  $\text{Ce}^{3+}$  garnet powder material synthetized by sol gel method." *Optical Materials* 157 (2024): 116329, doi: 10.1016/j.optmat.2024.116329.
- [2] M. J. Weber, "Inorganic scintillators: today and tomorrow," *J. Lumin.*, vol. 100, no. 1–4, pp. 35–45, Dec. 2002, doi: 10.1016/S0022-2313(02)00423-4.
- [3] M. Nikl and A. Yoshikawa, "Recent R&D Trends in Inorganic Single-Crystal Scintillator Materials for Radiation Detection," *Adv. Opt. Mater.*, vol. 3, no. 4, pp. 463–481, Apr. 2015, doi: 10.1002/adom.201400571.
- [4] C. Dujardin *et al.*, "Needs, Trends, and Advances in Inorganic Scintillators," *IEEE Trans. Nucl. Sci.*, vol. 65, no. 8, pp. 1977–1997, Aug. 2018, doi: 10.1109/TNS.2018.2840160.
- [5] P. Dorenbos, "(INVITED) The quest for high resolution  $\gamma$ -ray scintillators," *Opt. Mater. X*, vol. 1, p. 100021, Jan. 2019, doi: 10.1016/j.omx.2019.100021.
- [6] C. Dujardin, A. Bessière, A. Bulin, F. Chaput, and B. Mahler, "Inorganic Nanoscintillators: Current Trends and Future Perspectives," *Adv. Opt. Mater.*, p. 2402739, Jan. 2025, doi: 10.1002/adom.202402739.
- [7] G. F. Knoll, (2010). Radiation detection and measurement. John & Wiley Sons Inc.
- [8] P. T. Dickens, D. T. Haven, S. Friedrich, M. Saleh, and K. G. Lynn, "Increased luminescence and improved decay kinetics in lithium and cerium co-doped yttrium aluminum garnet scintillators grown by the Czochralski method," *J. Appl. Phys.*, vol. 121, no. 12, p. 123104, Mar. 2017, doi: 10.1063/1.4978376.
- [9] D. J. Robbins, (1979). The effects of crystal field and temperature on the photoluminescence excitation efficiency of Ce<sup>3+</sup> in YAG. *Journal of the electrochemical society*, *126*(9), 1550.
- [10] A. K. Singh, S. K. Singh, and S. B. Rai, "Role of Li<sup>+</sup> ion in the luminescence enhancement of lanthanide ions: favorable modifications in host matrices," *RSC Adv*, vol. 4, no. 51, pp. 27039–27061, 2014, doi: 10.1039/C4RA01055H.
- [11] K. Kamada *et al.*, "Growth and scintillation properties of Li and Ce co-doped Lu3Al5O12 scintillator," *J. Cryst. Growth*, vol. 452, pp. 85–88, Oct. 2016, doi: 10.1016/j.jcrysgro.2016.04.036.

- [12] K. Kamada *et al.*, "Single crystal growth of Ce:Gd3(Ga,Al)5O12 with various Mg concentration and their scintillation properties," *J. Cryst. Growth*, vol. 468, pp. 407–410, Jun. 2017, doi: 10.1016/j.jcrysgro.2016.11.026.
- [13] A. Bauzá, T. J. Mooibroek, and A. Frontera, "Towards design strategies for anion- $\pi$  interactions in crystal engineering," *CrystEngComm*, vol. 18, no. 1, pp. 10–23, 2016, doi: 10.1039/C5CE01813G.
- [14] Foster, Camera, "CZOCHRALSKI GROWTH AND SCINTILLATION PROPERTIES OF LITHIUM, SODIUM, AND POTASSIUM CODOPED LUTETIUM, YTTRIUM ALUMINUM GARNET SINGLE CRYSTALS FOR APPLICATIONS IN MEDICAL IMAGING." PhD diss., University of Tennessee, 2019.
- [15] C. Foster, Y. Wu, L. Stand, M. Koschan, and C. L. Melcher, "Czochralski growth and scintillation properties of Li+, Na+, and K+ codoped (Lu0.75, Y0.25)3Al5O12: Pr3+ single crystals," *J. Cryst. Growth*, vol. 532, p. 125408, Feb. 2020, doi: 10.1016/j.jcrysgro.2019.125408.
- [16] C. Foster, Y. Wu, M. Koschan, and C. L. Melcher, "Improvements in Light Yield and Energy Resolution by Li <sup>+</sup> Codoping (Lu <sub>0.75</sub> Y <sub>0.25</sub> ) <sub>3</sub> Al <sub>5</sub> O <sub>12</sub>:Pr <sup>3+</sup> Single Crystal Scintillators," *Phys. Status Solidi RRL Rapid Res. Lett.*, vol. 12, no. 9, p. 1800280, Sep. 2018, doi: 10.1002/pssr.201800280.
- [17] R. Naik, S. C. Prashantha, and H. Nagabhushana, "Effect of Li+ codoping on structural and luminescent properties of Mg2SiO4:RE3+ (RE = Eu, Tb) nanophosphors for displays and eccrine latent fingerprint detection," *Opt. Mater.*, vol. 72, pp. 295–304, Oct. 2017, doi: 10.1016/j.optmat.2017.06.021.
- [18] D. Toptygin, "Effects of the Solvent Refractive Index and Its Dispersion on the Radiative Decay Rate and Extinction Coefficient of a Fluorescent Solute," *J. Fluoresc.*, vol. 13, no. 3, pp. 201–219, May 2003, doi: 10.1023/A:1025033731377.
- [19] J. Y. Jung *et al.*, "Identification and development of nanoscintillators for biotechnology applications," *J. Lumin.*, vol. 154, pp. 569–577, Oct. 2014, doi: 10.1016/j.jlumin.2014.05.040.
- [20] G. Blasse, "Scintillator materials," *Chem. Mater.*, vol. 6, no. 9, pp. 1465–1475, Sep. 1994, doi: 10.1021/cm00045a002.
- [21] C. Greskovich and S. Duclos, "CERAMIC SCINTILLATORS," *Annu. Rev. Mater. Sci.*, vol. 27, no. 1, pp. 69–88, Aug. 1997, doi: 10.1146/annurev.matsci.27.1.69.

- [22] C. B. Carter and M. G. Norton, "Growing Single Crystals," in *Ceramic Materials*, New York, NY: Springer New York, 2013, pp. 523–542. doi: 10.1007/978-1-4614-3523-5\_29.
- [23] D. Savytskii, B. Knorr, V. Dierolf, and H. Jain, "Demonstration of single crystal growth via solid-solid transformation of a glass," *Sci. Rep.*, vol. 6, no. 1, p. 23324, Mar. 2016, doi: 10.1038/srep23324.
- [24] M. Kivambe, B. Aissa, and N. Tabet, "Emerging Technologies in Crystal Growth of Photovoltaic Silicon: Progress and Challenges," *Energy Procedia*, vol. 130, pp. 7–13, Sep. 2017, doi: 10.1016/j.egypro.2017.09.405.
- [25] C. Zhang and J. Lin, "Defect-related luminescent materials: synthesis, emission properties and applications," *Chem. Soc. Rev.*, vol. 41, no. 23, p. 7938, 2012, doi: 10.1039/c2cs35215j.
- [26] S. K. Gupta and Y. Mao, "Nanoscintillators," in *21st Century Nanoscience A Handbook*, 1st ed., K. D. Sattler, Ed., Boca Raton, Florida: CRC Press, [2020]: CRC Press, 2020, pp. 6-1-6-18. doi: 10.1201/9780429351594-6.
- [27] A. Boukerika and L. Guerbous, "Investigation of the structural and photoluminescence properties of Ce3+-doped LuAG nanopowders prepared via sol-gel method," *Opt. Mater.*, vol. 40, pp. 14-19, Feb. 2015, doi: 10.1016/j.optmat.2014.11.039.
- [28] F. Bakan, O. Laçin, and H. Sarac, "A novel low temperature sol–gel synthesis process for thermally stable nano crystalline hydroxyapatite," *Powder Technol.*, vol. 233, pp. 295–302, Jan. 2013, doi: 10.1016/j.powtec.2012.08.030.
- [29] F. Cova *et al.*, "Optical properties and radiation hardness of Pr-doped sol-gel silica: Influence of fiber drawing process," *J. Lumin.*, vol. 192, pp. 661–667, Dec. 2017, doi: 10.1016/j.jlumin.2017.07.045.
- [30] A. E. Danks, S. R. Hall, and Z. Schnepp, "The evolution of 'sol-gel'chemistry as a technique for materials synthesis." *Materials Horizons* 3.2 (2016): 91-112, doi: 10.1039/C5MH00260E.
- [31] H. K. Aity, E. Dhahri, and M. Rasheed, "Optimisation, dielectric properties, and antibacterial efficacy of copper-grafted MgO nanoparticles synthesized via sol-gel method," *Ceram. Int.*, vol. 50, no. 24, pp. 54666–54687, Dec. 2024, doi: 10.1016/j.ceramint.2024.10.324.

- [32] J. M. Nedelec, "Sol-gel processing of nanostructured inorganic scintillating materials." *Journal of Nanomaterials* 2007.1 (2007): 036392.
- [33] N. Dubnikova, E. Garskaite, A. Beganskiene, and A. Kareiva, "Sol-gel synthesis and characterization of sub-microsized lanthanide (Ho, Tm, Yb, Lu) aluminium garnets," *Opt. Mater.*, vol. 33, no. 8, pp. 1179–1184, Jun. 2011, doi: 10.1016/j.optmat.2011.02.008.
- [34] J. H. L. Mott and J. M. Daniel, "Interactions of Electromagnetic Radiation and Subatomic Particles with Matter Part 1," *Clin. Oncol.*, vol. 33, no. 7, pp. 451–454, Jul. 2021, doi: 10.1016/j.clon.2021.02.004.
- [35] C. Dujardin, "Inorganic scintillating materials." Électronique, Photonique, Optique Photonique, Tech. Rep., Techniques de l'ingénieur, Saint-Denis, France (2018).
- [36] A. R. Piotr, Rodnyi P A 1997 Physical Processes in Inorganic Scintillators (New York: CRC Press).
- [37] R. Hofstadter, "Alkali Halide Scintillation Counters," *Phys. Rev.*, vol. 74, no. 1, pp. 100–101, Jul. 1948, doi: 10.1103/PhysRev.74.100.
- [38] R. H. Gillette, "Calcium and Cadmium Tungstate as Scintillation Counter Crystals for Gamma-Ray Detection," *Rev. Sci. Instrum.*, vol. 21, no. 4, pp. 294–301, Apr. 1950, doi: 10.1063/1.1745567.
- [39] W. Van Sciver and R. Hofstadter, "Scintillations in Thallium-Activated Ca I 2 and CsI," *Phys. Rev.*, vol. 84, no. 5, pp. 1062–1063, Dec. 1951, doi: 10.1103/PhysRev.84.1062.2.
- [40] J.Bonanomi, (1952). Les scintillations de luminescence des iodures d'alcalins Université de Neuchâtel, (Doctoral dissertation).
- [41] W. V. Sciver, R. Hofstadter, and J. Eisenstein, "Gamma-and alpha-produced scintillations in cesium fluoride." *Physical Review* 87.3 (1952): 522.
- [42] Schenck, J., "Activation of lithium iodide by europium." *Nature* 171.4351 (1953): 518-519.
- [43] Brinkman, P., CsI(Na) scintillation of crystals, *Phys. Lett.*, 15, 305, 1965."
- [44] J. Menefee, C. F. Swinehart, and E. W. O'Dell, "Calcium Fluoride as an X-Ray and Charged Particle Detector," *IEEE Trans. Nucl. Sci.*, vol. 13, no. 1, pp. 720–724, 1966, doi: 10.1109/TNS.1966.4324036.

- [45] M. J. Weber and R. R. Monchamp, "Luminescence of Bi4 Ge3 O12: Spectral and decay properties," *J. Appl. Phys.*, vol. 44, no. 12, pp. 5495–5499, Dec. 1973, doi: 10.1063/1.1662183.
- [46] Ershov, N. N., N. G. Zakharov, and P. A. Rodnyi. "Spectral-kinetic study of the intrinsic-luminescence characteristics of a fluorite-type crystal." *Optics and Spectroscopy* 53.1 (1982): 51-54.
- [47] M. Laval *et al.*, "Barium fluoride Inorganic scintillator for subnanosecond timing," *Nucl. Instrum. Methods Phys. Res.*, vol. 206, no. 1–2, pp. 169–176, Feb. 1983, doi: 10.1016/0167-5087(83)91254-1.
- [48] Aleksandrov, Yu. M., Makhov, V. N., Rodnyi, P. A., Syreishchikova, T. I., and Yakimenko, M. N., Intrinsic luminescence of BaF<sub>2</sub> at pulse excitation by synchrotron radiation, Sov. Phys. Solid State, 26, 1734, 1984.
- [49] F. COVA, "Rare-Earth doped Scintillating Silica Fibers for ionizing radiation detection." (2020).
- [50] M. Fasoli, *Insights Into Microscopic Processes Governing Rare-earth (Ce3+, Tb3+) Scintillation Efficiency in Sol-gel Silica*. Diss. Università degli Studi di Milano-Bicocca, Dottorato di ricerca in scienza dei materiali, ciclo 18., 2006.
- [51] M. Nikl, "Scintillation detectors for x-rays." *Measurement Science and Technology* 17.4 (2006): R37.
- [52] Duan, Chang-Kui, and Michael F. Reid. "Local field effects on the radiative lifetimes of Ce3+ in different hosts." *Current Applied Physics* 6.3 (2006): 348-350, doi: 10.1016/j.cap.2005.11.016.
- [53] G. Bizarri, "Scintillation mechanisms of inorganic materials: From crystal characteristics to scintillation properties," *J. Cryst. Growth*, vol. 312, no. 8, pp. 1213–1215, Apr. 2010, doi: 10.1016/j.jcrysgro.2009.12.063.
- [54] E. Auffray and C. Ep-Cmx, "MODERN DEVELOPMENTS IN SCINTILLATORS".
- [55] M. J. Weber, "Inorganic scintillators: today and tomorrow," *J. Lumin.*, vol. 100, no. 1–4, pp. 35–45, Dec. 2002, doi: 10.1016/S0022-2313(02)00423-4.
- [56] C. Dujardin *et al.*, "Needs, Trends, and Advances in Inorganic Scintillators," *IEEE Trans. Nucl. Sci.*, vol. 65, no. 8, pp. 1977–1997, Aug. 2018, doi: 10.1109/TNS.2018.2840160.

- [57] P. Dorenbos, "The 5d level positions of the trivalent lanthanides in inorganic compounds," *J. Lumin.*, vol. 91, no. 3–4, pp. 155–176, Nov. 2000, doi: 10.1016/S0022-2313(00)00229-5.
- [58] Van Eijk, Carel WE. "Development of inorganic scintillators." *Nuclear Instruments and Methods in Physics Research Section A: Accelerators, Spectrometers, Detectors and Associated Equipment* 392.1-3 (1997): 285-290, doi: 10.1016/S0168-9002(97)00239-8.
- [59] Brooks, F. D. "Development of organic scintillators." *Nuclear Instruments and Methods* 162.1-3 (1979): 477-505, doi: 10.1016/0029-554X(79)90729-8.
- [60] M. Koshimizu, "Recent progress of organic scintillators," *Jpn. J. Appl. Phys.*, vol. 62, no. 1, p. 010503, Jan. 2023, doi: 10.35848/1347-4065/ac94fe.
- [61] R. C. Sangster and J. W. Irvine, "Study of Organic Scintillators," *J. Chem. Phys.*, vol. 24, no. 4, pp. 670–715, Apr. 1956, doi: 10.1063/1.1742595.
- [62] V. S. Shevelev, A. V. Ishchenko, A. S. Vanetsev, V. Nagirnyi, and S. I. Omelkov, "Ultrafast hybrid nanocomposite scintillators: A review," *J. Lumin.*, vol. 242, p. 118534, Feb. 2022, doi: 10.1016/j.jlumin.2021.118534.
- [63] M. Xia *et al.*, "Organic-inorganic hybrid perovskite scintillators for mixed field radiation detection," *InfoMat*, vol. 4, no. 9, p. e12325, Sep. 2022, doi: 10.1002/inf2.12325.
- [64] W. Chewpraditkul *et al.*, "Scintillation properties of Gd3Al2Ga3O12:Ce, Li and Gd3Al2Ga3O12:Ce, Mg single crystal scintillators: A comparative study," *Opt. Mater.*, vol. 92, pp. 181–186, Jun. 2019, doi: 10.1016/j.optmat.2019.04.023.
- [65] P. T. Dickens, D. T. Haven, S. Friedrich, M. Saleh, and K. G. Lynn, "Increased luminescence and improved decay kinetics in lithium and cerium co-doped yttrium aluminum garnet scintillators grown by the Czochralski method," *J. Appl. Phys.*, vol. 121, no. 12, p. 123104, Mar. 2017, doi: 10.1063/1.4978376.
- [66] Z. Xia and A. Meijerink, "Ce <sup>3+</sup> -Doped garnet phosphors: composition modification, luminescence properties and applications," *Chem. Soc. Rev.*, vol. 46, no. 1, pp. 275–299, 2017, doi: 10.1039/C6CS00551A.
- [67] Wu, Jennifer L., Gautam Gundiah, and A. K. Cheetham. "Structure-property correlations in Ce-doped garnet phosphors for use in solid state lighting." *Chemical Physics Letters* 441.4-6 (2007): 250-254, doi: 10.1016/j.cplett.2007.05.023.

- [68] Mateika, D., E. Völkel, and J. Haisma. "Lattice-constant-adaptable crystallographics: II. Czochralski growth from multicomponent melts of homogeneous mixed-garnet crystals." *Journal of crystal growth* 102.4 (1990): 994-1013, doi: 10.1016/0022-0248(90)90870-Q
- [69] J. Long *et al.*, "Enhanced Luminescence Performances of Tunable Lu  $_{3-}$  X Y  $_x$  Al $_5$  O $_{12}$ :Mn $^{4+}$  Red Phosphor by Ions of Rn $^+$  (Li $^+$ , Na $^+$ , Ca $^{2+}$ , Mg $^{2+}$ , Sr $^{2+}$ , Sc $^{3+}$ )," *Inorg. Chem.*, vol. 56, no. 6, pp. 3269–3275, Mar. 2017, doi: 10.1021/acs.inorgchem.6b02647.
- [70] S. Wang, J. Zhang, G. Jing, Z. Ye, H. Yu, and H. Zhang, "Exploring impurity phases derived from the introduction of vanadium ions in yttrium gallium garnet," *Ceram. Int.*, vol. 46, no. 16, pp. 25996–26003, Nov. 2020, doi: 10.1016/j.ceramint.2020.07.090.
- [71] T. Tomiki, H. Akamine, M. Gushiken, Y. Kinjoh, M. Miyazato, T. Miyazato, N. Toyokawa, M. Hiraoka, N. Hirata and Y. Ganaha, J. Phys. Soc. Jpn., 1991, 60, 2437–2445.
- [72] Van Pieterson, L., et al. "Emission spectra and trends for 4f n- 1 5d $\leftrightarrow$  4f n transitions of lanthanide ions: Experiment and theory." *The Journal of Chemical Physics* 115.20 (2001): 9382-9392, doi: 10.1063/1.1414318.
- [73] J. M. Ogiegło, A. Zych, T. Jüstel, A. Meijerink, and C. R. Ronda, "Luminescence and energy transfer in Lu3Al5O12 scintillators co-doped with Ce3+ and Pr3+," *Opt. Mater.*, vol. 35, no. 3, pp. 322–331, Jan. 2013, doi: 10.1016/j.optmat.2012.08.010.
- [74] Henderson, Brian, and G. Frank Imbusch. *Optical spectroscopy of inorganic solids*. Vol. 44. Oxford University Press, 2006.
- [75] Y.-C. Lin, M. Bettinelli, and M. Karlsson, "Unraveling the Mechanisms of Thermal Quenching of Luminescence in Ce <sup>3+</sup> -Doped Garnet Phosphors," *Chem. Mater.*, vol. 31, no. 11, pp. 3851–3862, Jun. 2019, doi: 10.1021/acs.chemmater.8b05300.
- [76] G. Blasse and B. C. Grabmaier, *Luminescent Materials*. Berlin, Heidelberg: Springer Berlin Heidelberg, 1994. doi: 10.1007/978-3-642-79017-1.
- [77] Shionoya, S.; Yen, W. M.; Yamamoto, H. Phosphor Handbook; CRC Press: Boca Raton, FL, 2006.
- [78] Duan, Chang-Kui, Hongli Wen, and Peter A. Tanner. "Local-field effect on the spontaneous radiative emission rate." *Physical Review B—Condensed Matter and Materials Physics* 83.24 (2011): 245123, doi: 10.1103/PhysRevB.83.245123.

- [79] J. L. Sommerdijk, A. Bril, and A. W. De Jager, "Two photon luminescence with ultraviolet excitation of trivalent praseodymium," *J. Lumin.*, vol. 8, no. 4, pp. 341–343, Feb. 1974, doi: 10.1016/0022-2313(74)90006-4.
- [80] Van Eijk, C. W. E., P. Dorenbos, and R. Visser. "Nd/sup 3+/and Pr/sup 3+/doped inorganic scintillators." *IEEE transactions on nuclear science* 41.4 (1994): 738-741.
- [81] P. Boutinaud, E. Pinel, M. Dubois, A. P. Vink, and R. Mahiou, "UV-to-red relaxation pathways in CaTiO3:Pr3+," *J. Lumin.*, vol. 111, no. 1–2, pp. 69–80, Jan. 2005, doi: 10.1016/j.jlumin.2004.06.006.
- [82] M. P. Sylvia and B. Hons, "Sol-gel Synthesis of and Luminescent Properties of Pr3+ in Different Host Matrices".
- [83] L. Shaw, B. Harbison, B. Cole, J. Sanghera, and I. Aggarwal, "Spectroscopy of the IR transitions in Pr3+ doped heavy metal selenide glasses," *Opt. Express*, vol. 1, no. 4, p. 87, Aug. 1997, doi: 10.1364/OE.1.000087.
- [84] A. Bauzá, T. J. Mooibroek, and A. Frontera, "Towards design strategies for anion- $\pi$  interactions in crystal engineering," *CrystEngComm*, vol. 18, no. 1, pp. 10–23, 2016, doi: 10.1039/C5CE01813G.
- [85] M. J. Odziomek, "Colloidal Synthesis and Controlled 2D/3D Assemblies of Oxide Nanoparticles".
- [86] A. Berneking *et al.*, "A new PET detector concept for compact preclinical high-resolution hybrid MR-PET," *Nucl. Instrum. Methods Phys. Res. Sect. Accel. Spectrometers Detect. Assoc. Equip.*, vol. 888, pp. 44–52, Apr. 2018, doi: 10.1016/j.nima.2018.01.040.
- [87] C.-C. Hsu, S.-L. Lin, and C. A. Chang, "Lanthanide-Doped Core-Shell-Shell Nanocomposite for Dual Photodynamic Therapy and Luminescence Imaging by a Single X-ray Excitation Source," *ACS Appl. Mater. Interfaces*, vol. 10, no. 9, pp. 7859–7870, Mar. 2018, doi: 10.1021/acsami.8b00015.
- [88] C. Hu et al., "Ultrafast Inorganic Scintillators for GHz Hard X-Ray Imaging".
- [89] X. Li, Z. Xue, M. Jiang, Y. Li, S. Zeng, and H. Liu, "Soft X-ray activated NaYF<sub>4</sub>:Gd/Tb scintillating nanorods for *in vivo* dual-modal X-ray/X-ray-induced optical bioimaging," *Nanoscale*, vol. 10, no. 1, pp. 342–350, 2018, doi: 10.1039/C7NR02926H.

- [90] S. R. Miller *et al.*, "Reduced Afterglow Codoped CsI:Tl for High-Energy Imaging," *IEEE Trans. Nucl. Sci.*, vol. 65, no. 8, pp. 2105–2108, Aug. 2018, doi: 10.1109/TNS.2018.2807986.
- [91] S. Yamamoto, K. Kamada, and A. Yoshikawa, "Ultrahigh resolution radiation imaging system using an optical fiber structure scintillator plate," *Sci. Rep.*, vol. 8, no. 1, p. 3194, Feb. 2018, doi: 10.1038/s41598-018-21500-z.
- [92] Duan, Chang-Kui, Michael F. Reid, and Zhongqing Wang. "Local field effects on the radiative lifetime of emitters in surrounding media: virtual-or real-cavity model?." *Physics Letters A* 343.6 (2005): 474-480, doi: 10.1016/j.physleta.2005.06.037.
- [93] B. C. Grabmaier, W. Rossner, and J. Leppert, "Ceramic scintillators for X-Ray computed tomography," *Phys. Status Solidi A*, vol. 130, no. 2, pp. K183–K187, Apr. 1992, doi: 10.1002/pssa.2211300242.
- [94] Buşe, G., et al. "First scintillating bolometer tests of a CLYMENE R&D on Li2MoO4 scintillators towards a large-scale double-beta decay experiment." *Nuclear Instruments and Methods in Physics Research Section A: Accelerators, Spectrometers, Detectors and Associated Equipment* 891 (2018): 87-91, doi: 10.1016/j.nima.2018.02.101.
- [95] M. Zhu *et al.*, "Growth and luminescent properties of Yb:YAG and Ca co-doped Yb:YAG ultrafast scintillation crystals," *J. Cryst. Growth*, vol. 490, pp. 51–55, May 2018, doi: 10.1016/j.jcrysgro.2018.03.015.
- [96] A. Khan, G. Rooh, H. J. Kim, and S. Kim, "Ce3+-activated Tl2GdCl5: Novel halide scintillator for X-ray and γ-ray detection," *J. Alloys Compd.*, vol. 741, pp. 878–882, Apr. 2018, doi: 10.1016/j.jallcom.2018.01.204.
- [97] Krestel, Erich. "Imaging Systems for Medical Diagnosis: Fundamentals and Technical Solutions-X-Ray Diagnostics-Computed Tomography-Nuclear Medical Diagnostics-Magnetic Resonance Imaging-Ultrasound Technology." *Imaging Systems for Medical Diagnosis: Fundamentals and Technical Solutions-X-Ray Diagnostics-Computed Tomography-Nuclear Medical Diagnostics-Magnetic Resonance Imaging-Ultrasound Technology* (1990): 627.
- [98] Moses, William W. "Scintillator requirements for medical imaging." (1999).

- [99] J. G. Reynolds, G. E. Lawson, and C. J. Koester, Eds., *Antiterrorism and Homeland Defense: Polymers and Materials*, vol. 980. in ACS Symposium Series, vol. 980. Washington, DC: American Chemical Society, 2007. doi: 10.1021/bk-2007-0980.
- [100] N. V. Klassen *et al.*, "Advantages and Problems of Nanocrystalline Scintillators," *IEEE Trans. Nucl. Sci.*, vol. 55, no. 3, pp. 1536–1541, Jun. 2008, doi: 10.1109/TNS.2008.924050.
- [101] Tissue, Brian M., and Bipin Bihari. "Lanthanide luminescence as a probe of nanocrystalline materials." *Journal of Fluorescence* 8.4 (1998): 289-294.
- [102] Mercier, B., et al. "Quantum confinement effect on Gd2O3 clusters." *The Journal of chemical physics* 126.4 (2007), doi: 10.1063/1.2431366.
- [103] Tanner, Peter A., Lianshe Fu, and Bing-Ming Cheng. "Spectral band shifts in the electronic spectra of rare earth sesquioxide nanomaterials doped with europium." *The Journal of Physical Chemistry C* 113.24 (2009): 10773-10779.
- [104] C. Dujardin, D. Amans, A. Belsky, F. Chaput, G. Ledoux, and A. Pillonnet, "Luminescence and Scintillation Properties at the Nanoscale," *IEEE Trans. Nucl. Sci.*, vol. 57, no. 3, pp. 1348–1354, Jun. 2010, doi: 10.1109/TNS.2009.2035697.
- [105] Dujardin, Christophe, et al. "LuAG: Ce fibers for high energy calorimetry." *Journal of Applied Physics* 108.1 (2010), doi: 10.1063/1.3452358.
- [106] Mekki, H., et al. "Scintillation properties of (Lu1-x Y x) 3Al5O12: Ce3+ nanoscintillator solid solution garnet materials." *Journal of Instrumentation* 18.02 (2023): P02007, doi: 10.1088/17480221/18/02/P02007.
- [107] G. F. Harrington and J. Santiso, "Back-to-Basics tutorial: X-ray diffraction of thin films," *J. Electroceramics*, vol. 47, no. 4, pp. 141–163, Dec. 2021, doi: 10.1007/s10832-021-00263-6.
- [108] Zhou, Weilie, et al. "Fundamentals of scanning electron microscopy (SEM)." *Scanning microscopy for nanotechnology: techniques and applications*. New York, NY: Springer New York, 2006. 1-40.
- [109] Newbury, Dale E. "Energy-Dispersive Spectrometry." *Characterization of Materials* (2002).
- [110] T. H. Gfroerer, "Photoluminescence in Analysis of Surfaces and Interfaces," in *Encyclopedia of Analytical Chemistry*, 1st ed., R. A. Meyers, Ed., Wiley, 2000. doi: 10.1002/9780470027318.a2510.

- [111] M. Nikl, V. V. Laguta, and A. Vedda, "Complex oxide scintillators: Material defects and scintillation performance," *Phys. Status Solidi B*, vol. 245, no. 9, pp. 1701–1722, Sep. 2008, doi: 10.1002/pssb.200844039.
- [112] Kresse, Georg, and Jürgen Furthmüller. "Efficient iterative schemes for ab initio total-energy calculations using a plane-wave basis set." *Physical review B* 54.16 (1996): 11169.
- [113] Mermin, N. David. "Thermal properties of the inhomogeneous electron gas." *Physical Review* 137.5A (1965): A1441.
- [114] Perdew, John P., and Alex Zunger. "Self-interaction correction to density-functional approximations for many-electron systems." *Physical review B* 23.10 (1981): 5048.
- [115] Hedin, Lars, and Bengt I. Lundqvist. "Explicit local exchange-correlation potentials." *Journal of Physics C: Solid state physics* 4.14 (1971): 2064.
- [116] Ceperley, David M., and Berni J. Alder. "Ground state of the electron gas by a stochastic method." *Physical review letters* 45.7 (1980): 566.
- [117] D. Vanderbilt, *State-of-the-art simulations in electronic structure and total energy for surface science*, European Winter School, (2001).
- [118] Kresse, Georg, and Daniel Joubert. "From ultrasoft pseudopotentials to the projector augmented-wave method." *Physical review b* 59.3 (1999): 1758.
- [119] Blöchl, Peter E. "Projector augmented-wave method." *Physical review B* 50.24 (1994): 17953.
- [120] Davidson, C. G. "14) IF f lag D 0 THEN." *Journal of Computational Physics* 17 (1975): 87-94.
- [121] Murray, Christopher W., Stephen C. Racine, and Ernest R. Davidson. "Improved algorithms for the lowest few eigenvalues and associated eigenvectors of large matrices." *Journal of Computational Physics* 103.2 (1992): 382-389.
- [122] Pulay, Péter. "Convergence acceleration of iterative sequences. The case of SCF iteration." *Chemical physics letters* 73.2 (1980): 393-398.
- [123] S. Blugel. First Principles Calculations of the Electronic Structure of Magnetic Overlayers on Transition Metal Surfaces. PhD thesis, RWTH Aachen, (1988).
- [124] Johnson, Duane D. "Modified Broyden's method for accelerating convergence in self-consistent calculations." *Physical Review B* 38.18 (1988): 12807.
- [125] Feynman, Richard Phillips. "Forces in molecules." *Physical review* 56.4 (1939): 340. doi: https://doi.org/10.1103/PhysRev.56.340

- [126] W. C. DAVIDON, Variable metric methods for minimization, A. E. C. Res. and Develop. Report ANL-5990, Argonne National Laboratory, Argonne, Illinois. (1959).
- [127] Hohenberg, Pierre, and Walter Kohn. "Inhomogeneous electron gas." *Physical review* 136.3B (1964): B864, doi: 10.1103/PhysRev.136.B864.
- [128] Kohn, Walter, and Lu Jeu Sham. "Self-consistent equations including exchange and correlation effects." *Physical review* 140.4A (1965): A1133, doi: 10.1103/PhysRev.140.A1133.
- [129] G. Kresse and J. Furthmüller, "Efficient iterative schemes for *ab initio* total-energy calculations using a plane-wave basis set," *Phys. Rev. B*, vol. 54, no. 16, pp. 11169–11186, Oct. 1996, doi: 10.1103/PhysRevB.54.11169.
- [130] Guo, Weian, et al. "Surface structure and electronic properties of Lu3Al5O12." *Crystals* 11.11 (2021): 1433.
- [131] G. K. Williamson and W. H. Hall, "X-ray line broadening from filed aluminium and wolfram," *Acta Metall.*, vol. 1, no. 1, pp. 22–31, Jan. 1953, doi: 10.1016/0001-6160(53)90006-6.
- [132] Bauzá, Antonio, Tiddo J. Mooibroek, and Antonio Frontera. "Towards design strategies for anion- $\pi$  interactions in crystal engineering." *CrystEngComm* 18.1 (2016): 10-23, doi: 10.1039/C5CE01813G.
- [133] Y. Wu *et al.*, "Role of Lithium Codoping in Enhancing the Scintillation Yield of Aluminate Garnets," *Phys. Rev. Appl.*, vol. 13, no. 6, p. 064060, Jun. 2020, doi: 10.1103/PhysRevApplied.13.064060.
- [134] R. Shi and A.-V. Mudring, "Phonon-Mediated Nonradiative Relaxation in Ln³+ -Doped Luminescent Nanocrystals," *ACS Mater. Lett.*, vol. 4, no. 10, pp. 1882–1903, Oct. 2022, doi: 10.1021/acsmaterialslett.2c00595.
- [135] J. A. Mares, M. Nikl, J. Chval, I. Dafinei, P. Lecoq, and J. Kvapil, "Fluorescence and scintillation properties of LuAlO3:Ce crystal," *Chem. Phys. Lett.*, vol. 241, no. 4, pp. 311–316, Jul. 1995, doi: 10.1016/0009-2614(95)00677-V.
- [136] Y. Zhang, Y. Zhang, Y. Zhang, and H. Gong, "Synthesis and characteristics of fine crystalline LuAG:Ce phosphors by microwave-induced solution combustion method," *J. Lumin.*, vol. 181, pp. 360–366, Jan. 2017, doi: 10.1016/j.jlumin.2016.09.048.

- [137] Ponkumar, S., et al. "Synthesis, characterization, and enhanced photoluminescence of ZrO2: Dy3+ phosphors by incorporating Li+, Na+ and K+ ions for LED applications." *Ceramics International* 50.8 (2024): 13219-13228.
- [138] V. V. Shanbhag *et al.*, "Impacts of core shell structure on structural and photoluminescence properties of CaTiO<sub>3</sub>:Sm<sup>3+</sup>, Li<sup>+</sup> nanoparticles for solid state display applications," *Mater. Res. Express*, vol. 6, no. 8, p. 085037, May 2019, doi: 10.1088/2053-1591/ab1d1d.
- [139] Lopez, O. A., J. McKittrick, and L. E. Shea. "Fluorescence properties of polycrystalline Tm3+-activated Y3Al5O12 and Tm3+-Li+ co-activated Y3Al5O12 in the visible and near IR ranges." *Journal of Luminescence* 71.1 (1997): 1-11.
- [140] Altowyan, Abeer S., et al. "Lattice distortion effects induced by Li+ co-doping on ZnO: Tb3+ phosphors: Photoluminescence and unusual hypersensitive  $^5D_4 \rightarrow ^7F_0$  transition." *Ceramics International* 50.13 (2024): 24036-24044.
- [141] Souadi, G., et al. "Synthesis and enhanced photoluminescence of the BaSiF6: Dy3+ phosphors by Li+ doping via combustion method." *Journal of Luminescence* 241 (2022): 118512.
- [142] P. Dorenbos, "Electronic structure and optical properties of the lanthanide activated RE3(Al1–xGax)5O12 (RE=Gd, Y, Lu) garnet compounds," *J. Lumin.*, vol. 134, pp. 310–318, Feb. 2013, doi: 10.1016/j.jlumin.2012.08.028.
- [143] Vu, Duc Tu, et al. "Enhancing upconversion luminescence emission of rare earth nanophosphors in aqueous solution with thousands fold enhancement factor by low refractive index resonant waveguide grating." *ACS Photonics* 5.8 (2018): 3263-3271, doi: 10.1021/acsphotonics.8b00494.
- [144] J. M. Ogiegło, A. Zych, T. Jüstel, A. Meijerink, and C. R. Ronda, "Luminescence and energy transfer in  $Lu_3Al_5O_{12}$  scintillators co-doped with  $Ce^{3+}$  and Pr3+," *Opt. Mater.*, vol. 35, no. 3, pp. 322–331, Jan. 2013, doi: 10.1016/j.optmat.2012.08.010.
- [145] G. B. Nair and S. J. Dhoble, "Assessment of electron-vibrational interaction (EVI) parameters of YAG:Ce3+, TAG:Ce³+ and LuAG:Ce³+ garnet phosphors by spectrum fitting method," *Spectrochim. Acta. A. Mol. Biomol. Spectrosc.*, vol. 173, pp. 822-826, Feb. 2017, doi: 10.1016/j.saa.2016.10.049.
- [146] V. Bachmann, C. Ronda, and A. Meijerink, "Temperature Quenching of Yellow Ce<sup>3+</sup> Luminescence in YAG:Ce," *Chem. Mater.*, vol. 21, no. 10, pp. 2077–2084, May 2009, doi: 10.1021/cm8030768.

- [147] Kučera, Miroslav, et al. "Gd3+ to Ce3+ energy transfer in multi-component GdLuAG and GdYAG garnet scintillators." *physica status solidi (RRL)-Rapid Research Letters* 7.8 (2013): 571-574, doi: 10.1002/pssr.201307256.
- [148] M. Kucera, K. Nitsch, M. Kubova, N. Solovieva, M. Nikl, and J. A. Mares, "Ce-doped YAG and LuAG Epitaxial Films for Scintillation Detectors," *IEEE Trans. Nucl. Sci.*, vol. 55, no. 3, pp. 1201–1205, Jun. 2008, doi: 10.1109/TNS.2007.913490.
- [149] Yu. V. Zorenko *et al.*, "Luminescence of excitons and antisite defects in Lu3Al5O12:Ce single crystals and single-crystal films," *Opt. Spectrosc.*, vol. 99, no. 6, pp. 923–931, Dec. 2005, doi: 10.1134/1.2149417.
- [150] Nikl, M., et al. "Traps and timing characteristics of LuAg: Ce {sup 3+} scintillator." *Physica Status Solidi A* 181 (2000), doi: 10.1002/1521-396X(200009)181:1<R10::AID-PSSA999910>3.0.CO;2-9.
- [151] R. Praveena, L. Shi, K. H. Jang, V. Venkatramu, C. K. Jayasankar, and H. J. Seo, "Solgel synthesis and thermal stability of luminescence of Lu3Al5O12:Ce3+ nanogarnet," *J. Alloys Compd.*, vol. 509, no. 3, pp. 859–863, Jan. 2011, doi: 10.1016/j.jallcom.2010.09.113.
- [152] X. He *et al.*, "Effects of local structure of Ce3+ ions on luminescent properties of Y3Al5O12:Ce nanoparticles," *Sci. Rep.*, vol. 6, no. 1, p. 22238, Mar. 2016, doi: 10.1038/srep22238.
- [153] H. P. Christensen, D. R. Gabbe, and H. P. Jenssen, "Fluorescence lifetimes for neodymium-doped yttrium aluminum garret and yttrium oxide powders," *Phys. Rev. B*, vol. 25, no. 3, pp. 1467–1473, Feb. 1982, doi: 10.1103/PhysRevB.25.1467.
- [154] J. Amami, D. Hreniak, Y. Guyot, W. Zhao, and G. Boulon, "Size-effect on concentration quenching in Yb3+-doped Y3Al5O12 nano-crystals," *J. Lumin.*, vol. 130, no. 4, pp. 603–610, Apr. 2010, doi: 10.1016/j.jlumin.2009.11.003.
- [155] Meltzer, R. S $\hat{\mathbb{H}}$ , et al. "Dependence of fluorescence lifetimes of Y 2 O 3: E u 3+ nanoparticles on the surrounding medium." *Physical Review B* 60.20 (1999): R14012, doi: 10.1103/PhysRevB.60.R14012.
- [156] R. M. Krsmanović, Ž. Antić, M. G. Nikolić, M. Mitrić, and M. D. Dramićanin, "Preparation of Y2O3:Eu3+ nanopowders via polymer complex solution method and luminescence properties of the sintered ceramics," *Ceram. Int.*, vol. 37, no. 2, pp. 525–531, Mar. 2011, doi: 10.1016/j.ceramint.2010.09.040.
- [157] N. Bloembergen, Nonlinear Optics. New York: W.A. Benjamin, New York, 1965.

#### **Abstract**

This PhD research investigates the synthesis and the structural, morphological, and optical properties of  $Lu_3Al_5O_{12}$  (LuAG) garnet-based scintillators, doped with  $Ce^{3+}$  or  $Pr^{3+}$ , and co-doped with alkali metal ions (Li<sup>+</sup>, Na<sup>+</sup>, and K<sup>+</sup>) using the sol-gel method. Through experimental studies and theoretical simulations, the effects of alkali codoping on luminescence efficiency, crystallite size, and defect density were systematically analyzed. Li<sup>+</sup> co-doping was particularly effective in reducing crystallite size, enhancing photoluminescence (PL) and radioluminescence (RL), and minimizing trap densities, thereby improving scintillation efficiency and charge transport. Moreover, RL studies revealed faster scintillation compared to single crystals, with no afterglow observed. For LuAG:Pr<sup>3+</sup>, Li<sup>+</sup> also enhanced emission intensity and decay characteristics, reinforcing its potential for fast scintillation applications. These findings emphasize the importance of defect control and codoping strategies in optimizing garnet-based scintillators, positioning them as promising candidates for advanced radiation detection and optical technologies.

**Keywords**: Scintillators, LuAG:Ce<sup>3+</sup>, LuAG:Pr<sup>3+</sup>, co-doping, sol-gel, XRD, VASP, photoluminescence, radioluminescence, thermally stimulated luminescence (TSL).

#### Résumé

Cette recherche doctorale porte sur la synthèse ainsi que sur les propriétés structurales, morphologiques et optiques des scintillateurs à base de grenat Lu<sub>3</sub>Al<sub>5</sub>O<sub>12</sub> (LuAG), dopés avec Ce<sup>3+</sup> ou Pr<sup>3+</sup>, et co-dopés avec des ions alcalins (Li<sup>+</sup>, Na<sup>+</sup> et K<sup>+</sup>), en utilisant la méthode sol-gel. À travers des études expérimentales et des simulations théoriques, l'effet de la co-dopage alcaline sur l'efficacité de la luminescence, la taille des cristallites et la densité des défauts a été analysé de manière systématique. La co-dopage avec Li<sup>+</sup> s'est révélée particulièrement efficace pour réduire la taille des cristallites, améliorer la photoluminescence (PL) et la radioluminescence (RL), et minimiser la densité de pièges, ce qui a permis d'améliorer l'efficacité de scintillation et le transport de charge. De plus, les études de RL ont montré une scintillation plus rapide que celle des monocristaux, sans post-luminescence observée. Pour LuAG:Pr<sup>3+</sup>, le Li<sup>+</sup> a également renforcé l'intensité de l'émission et les caractéristiques de décroissance, confirmant son potentiel pour des applications de scintillation rapide. Ces résultats soulignent l'importance du contrôle des défauts et des stratégies de co-dopage pour optimiser les scintillateurs à base de grenat, les positionnant comme des candidats prometteurs pour la détection avancée des radiations et les technologies optiques.

**Mots-clés**: Scintillateurs, LuAG:Ce³+, LuAG:Pr³+, co-dopage, sol-gel, XRD, VASP, photoluminescence, radioluminescence, luminescence stimulée thermiquement (TSL).

# الملخص

**الكلمات المفتاحية :** كواشف الوميض،\*LuAG:Ce³+, LuAG:Pr³ ، التشويب المزدوج، السول-جيل، التلألؤ، العيوب البنيوية، المواد النانوبة.